Inaugural - Dissertation

submitted to the

Combined Faculties for the Natural Sciences and for Mathematics

of the Ruperto-Carola University of Heidelberg, Germany

for the degree of

Doctor of Natural Sciences

Put forward by

Diplom-Physiker (Medizinphysik) Mathies Breithaupt

Born in: Kappeln, Germany

Oral examination: July 21st, 2015

On Simulations of Spin Interactions Applied for
the Volumetric T_1 Quantification by
in vivo Magnetic Resonance Imaging at Ultra High Field

Referees: Prof. Dr. Wolfgang Schlegel
Prof. Dr. Mark Ladd

Erklärung Ich erkläre hiermit, dass ich die vorgelegte Dissertation selbst verfasst und mich dabei keiner anderen als der von mir ausdrücklich bezeichneten Quellen und Hilfen bedient habe.

Heidelberg, den 05.06.2015

Mathies Breithaupt

Für meine Familie

And now, the end is near,
And so I face the final curtain.
My friend, I'll say it clear,
I'll state my case, of which I'm certain.

I did it my way.

Frank Sinatra

Über Simulationen von Spinwechselwirkungen angewandt für die volumetrische T_1-Quantifizierung mit der In-vivo-Magnetresonanztomographie im Ultrahochfeld

In dieser Arbeit wird eine neuartige Methode zur volumetrischen Quantifizierung der longitudinalen Relaxationszeit T_1 mittels der Ultrahochfeld-Magnetresonanztomographie vorgestellt. Die Methode basiert auf der Vorhersage der MR-Signalstörungen durch Inhomogenitäten des statischen Magnetfelds und des eingestrahlten RF-Felds sowie durch im Bildgebungsprozess selbst entstehende Ausleseeffekte, und den daraus resultierenden Korrekturen. Für diesen Zweck wurden die mathematischen Formulierungen der magnetischen Bewegungsgleichung und der Bloch -Gleichungen in eine neue Simulationsumgebung implementiert und in entsprechenden Auswertealgorithmen betrachtet. Zusätzlich wurden verschiedene Ansätze zur Simulation des MR-Signals, auch unter Berücksichtigung von k-Raum-Filtern, sowie diverse Korrekturansätze untersucht.

Mit den vorgestellten SIMBA IR und SIMBA DESPOT1-HIFI-Methoden können T_1-Zeiten im Bereich von 1100 ms bis 3300 ms mit einer maximalen Abweichung vom Sollwert von (-0,42 ± 1,23) % bzw. (1,99 ± 1,58) % quantifiziert werden. Die Minimierung der Wiederholzeit *TR* im SIMBA IR-Experiment reduziert die Messzeit um bis zu 50 % und verbessert die Genauigkeit. Zusätzlich verringert die Verwendung einer nicht-adiabatischen Präparation die Belastung durch die spezifischen Absorptionsrate um bis zu 70 % und ermöglicht somit Untersuchungen in der Nähe von Risikoorganen. Mit der noch schnelleren SIMBA DESPOT1-HIFI-Methode benötigt die Messung eines Probenvolumens von $256\times256\times176\,\mathrm{mm}^3$ mit einer isotropen Auflösung von 1 mm weniger als 30 Minuten. In der Aufnahme eines gesamten menschlichen Gehirns wurde ein klarer Kontrast zwischen den verschiedenen Weichteil-Geweben ersichtlich. Für die graue Hirnsubstanz wurde eine T_1-Zeit von (1917 ± 95) ms bestimmt, während diese für die weiße Hirnsubstanz (1246 ± 56) ms beträgt. In der Untersuchung eines menschlichen Wadenmuskels wurde eine T_1-Zeit von (1877 ± 92) ms quantifiziert. Alle T1-Werte stimmen im Rahmen der Messunsicherheit mit Literaturwerten überein.

On Simulations of Spin Interactions Applied for the Volumetric T_1 Quantification by *in vivo* Magnetic Resonance Imaging at Ultra High Field

In this thesis, a novel technique for the volumetric quantification of the longitudinal relaxation time T_1 by ultra high field (UHF) magnetic resonance imaging (MRI) is introduced. It is based upon the prediction of the MR signal disturbances, due to static magnetic and RF field inhomogeneities as well as readout effects by the imaging process itself, and the corrections resulting hereof. For this reason, the mathematics of the magnetization's equation of motion and the BLOCH equations are implemented into a new simulation framework and regarded for by the evaluation algorithms. Furthermore, different MR signal simulation strategies additionally considering the k-space filters and various correction approaches are investigated.

The introduced SIMBA IR and SIMBA DESPOT1-HIFI methods are capable of quantifying T_1 with respective maximum deviations to the nominal values of $(-0.42 \pm 1.23)\,\%$ and $(1.99 \pm 1.58)\,\%$ within a T_1 range of 1100 ms to 3300 ms. A minimization of the repetition time TR within the SIMBA IR experiments shortens the measurement time by up to 50 % and further improves the accuracy. The use of a non-adiabatic preparation reduces the SAR exposure by up to 70 % and allows examinations near organs of risk. Eventually, the even faster SIMBA DESPOT1-HIFI method was applied on a volume of $256 \times 256 \times 176\,\mathrm{mm}^3$ with an isotropic resolution of 1 mm within less than 30 min. A study of the whole human brain revealed a clearly differentiated soft tissue contrast and T_1 values of (1917 ± 95) ms for the gray and (1246 ± 56) ms for the white matter. In a study on the human calf muscle, T_1 was quantified to a value of (1877 ± 92) ms. All T_1 values are in a strong agreement with literature values.

Contents

1 Introduction

Medical imaging has been playing a major role in the clinical context for decades. The modern use of this term originated in 1977 and refers to the recent, more technical approaches. A great variety of imaging modalities can be categorized by the nature of the obtained information, whether it corresponds to morphology or to function, and by the use of ionizing or non-ionizing radiation.

X-ray based technologies and modalities used in nuclear medicine utilize ionizing radiation for the signal generation. On the one hand, projection imaging as well as native computed tomography (CT) visualizes the skeleton structure and significant changes of the soft tissue. On the other hand, positron emission tomography (PET) and single-photon emission tomography (SPECT) provide information about functional and molecular processes. The exposure to ionizing radiation bears the risk of late term complications due to the deposition of a dose, though. Imaging modalities that use non-ionizing radiation are ultrasound (US) and MRI, besides others. Both are capable of acquiring morphological as well as functional information.

As a collective, these technologies are irreplaceable tools for medical interventions, clinical analyses, and diagnostics. Identifying and classifying pathologies within the human body without performing invasive procedures offers the information as it is, lessens the risk of complications, and improves the patient comfort. The significance of medical imaging becomes clear when its impact on the diagnostic value, the planning and staging of a therapy, and thus, the patient outcome is considered. Especially MRI, which has been honored with the Nobel Prize in Physiology and Medicine in the year 2003, has gained a fundamental clinical importance and is the subject of this thesis.

At this point in time, there are about six million clinical MRI examinations performed in Germany in each single year. Since the first experimental applications performed in 1973, it has not been reported that MRI causes any harm to the human body. Even highly repetitive measurements do not accumulate any kind of physical dose. Among all medical imaging modalities, it is a unique feature of MRI that numerous different contrasts can be evoked. These can either be in the nature of morphology, such as soft tissue or vascularization, or of a functional nature, such as perfusion, diffusion, or neurological connectivity and activity. From this multitude of independent information results a sensitivity and specificity towards different tissue types that modern medicine relies on. Without contrast, the identification and classification of pathologies is not possible. However, the information commonly presented by magnetic resonance (MR) images is only of relative signal values illustrated by an arbitrary grayscale.

Further development of the magnetic resonance technology to improve the imaging quality and efficiency is still an active research field. One major focus concerns the amplification of the static magnetic field strength. Clinically available field strengths of 1.5 T or 3.0 T have

been exceeded by experimental setups of 7 T and above. The most obvious benefit of a higher magnetic field strength is the improvement of the signal to noise ratio (SNR) which translates to a higher spatial resolution or a reduced measurement time.

However, with this benefit come a number of drawbacks. Inhomogeneity of the static magnetic field and the radio frequency (RF) field along with the safety issue of the specific absorption rate (SAR) are the most prominent examples. The static magnetic field is responsible for the emergence of a macroscopic magnetization which is the basis for the MR signal. A variation therein causes a variation in the resonance condition of the observed nuclei. Typical appearances of such are signal cancellations, spatial distortions, and ghosting artifacts in space and time. An additional RF pulse is responsible for the manipulation of the macroscopic magnetization. On the one hand, the magnetic field component of this RF wave scales the signal amplitude and is typically needed to imprint the desired contrast. A deviation from the nominal value also causes signal variations in terms of hypo- and hyperintensities and variations of the contrast in space. On the other hand, the electric field component of the RF wave is not needed for the imaging process itself, but is absorbed by the sample. This phenomenon is characterized by the SAR and causes tissue warming. To avoid injuries, either due to the denaturation of proteins or actual burning, regulatory guidelines must be complied with. The consequence is a limitation in the choice of imaging parameters influencing the desired SNR, the contrast, and the measurement time. For typical *in vivo* conditions, this overall spatial dependence of the signal causes false positive and false negative contrasts and can lead to inaccurate clinical evaluations.

If a similarity is drawn to the art of making music, the problem from above can be illustrated in a more vivid manner: A very well trained musician is playing of a demanding sheet of music on her electric piano, but not all the tones coming out of the speaker sound proper. The mismatch can be so severe, that the actual played composition can be misinterpreted as another piece of music. Because one would never dare to tune the hardware of her instrument, a different solution needs to be found.

As long as the mismatching tones correlate to certain musical notes, then either can only music be selected for presentation that does not incorporate these notes, or the written notes must be altered in such a way that the replacements sound proper. An alternative approach would be to again identify the mismatches but manipulate the electric signal to the speaker in such a way to make the music sound as it should. Any of these solutions might be so specific, that it only accounts for a certain combination of a musician, playing a specific song on a particular instrument.

If the role of the electronic piano is being replaced by an MR tomograph, the musician and the sheet of music by the console and an MRI sequence, and the musical note by an RF pulse, then the sound of the speaker can be interpreted as an MR image and the discord by false contrast. The approaches to solve the problem are not that much different than just specified above.

In contrast to conventional RF pulses, so called adiabatic pulses do hold the desired effect on the magnetization within a distinct range of nonuniform field distributions. Regarding the analogy above, this would compare to the situation where only certain notes are allowed in the sheet of music. However, this is not feasible due to the typically high SAR exposure

of adiabatic pulses. A trade-off between the RF pulse effect and the safety constraints is achieved by an optimization of the pulse shapes. Again regarding the analogy above, this is comparable to the alteration of specific musical notes to make them sound right.

The alternative approach from the analogy above pursues a completely different strategy, which is the fundamental idea behind the work presented in this thesis. Not only is the contrast for a single MR image corrected, but the corrected signals of multiple MR experiments are used to determine the investigated physical properties of the sample. In general, this process is called quantitative imaging. To accomplish this, the involved MRI experiments must be simulated regarding the inhomogeneity of the static magnetic and the RF field. From these simulations, the true signal evolution, defined by the respective physical properties, can be extracted. Knowing how a signal should evolve from these simulations, and how a signal does evolve from a measurement, allows for a post-processing correction. In more simple words, an actual MRI experiment evokes a signal that deviates from theory and this needs to be corrected for. To pick the corresponding correction, the physical properties need to be identified first. The quantification of the physical parameters is based on the signal. However, the signal is affected by the MRI experiment itself and needs to be corrected for. To overcome this circular dependency, the correction has to be implemented in an iterative manner. When applied voxelwise to the volumetric data, the outcome is a set of quantitative images.

Quantitative imaging has the striking benefit, that the determined parameter values are free of all local conditions. Such quantitative images are reproducible and comparable for inter-site and longitudinal studies. This gives rise to a new domain of cooperation and large-scale research. Furthermore and not to break with the current clinical routine, any respective conventional contrast can be generated from these parameter maps.

The main reason why this promising technique is not part of the clinical routine yet, can be attributed to the long measurement times beyond any reasonable time frame with conventional techniques. With the approach outlined above, the measurement time can be reduced as the effects of the accelerated image acquisition in the experiment can be corrected by the method presented in this thesis. Thus, *in vivo* quantitative imaging gets within the grasp of clinical applications.

Within this thesis, the novel approach to overcome the limitations of inhomogeneous static magnetic and RF field distributions outlined above is presented. The focus lies on how to make use of prior knowledge about how the signal evolves throughout MRI experiments from simulations. For this purpose, a numerical solver for the mathematics behind such simulations is introduced at first.

The second part presents a method to correct the signal in accelerated MRI and for quantitative imaging within clinical time frames. A number of correction strategies is investigated and evaluated concerning the accuracy and stability. The results from phantom experiments validate these methods. In addition, first *in vivo* applications of the volumetric quantification of the longitudinal relaxation time are shown.

2 Physical Background

This chapter introduces the physical background relevant for the understanding of this thesis. At first, a qualitative description of phenomena related to nuclear magnetic resonance (NMR) and considerations of the fundamental mathematics of the field of spin physics are touched in section 2.1. Secondly, the role of magnetic resonance imaging (MRI) as an application of NMR is highlighted in section 2.2. At last, specific issues regarding ultra high field (UHF) MRI with its benefits and limitations are presented in section 2.3. For more detailed information on nuclear magnetic resonance see [Slichter, 1978; Abragam, 1983; Haacke et al., 1999], on magnetic resonance imaging see [Bernstein et al., 2004; Reiser et al., 2007; Reimer et al., 2010], and on ultra high field MRI see [Robitaille and Berliner, 2006], respectively.

2.1 Nuclear Magnetic Resonance

The history of nuclear magnetic resonance and its discovery reaches over 100 years back in time. In 1902, Hendrik Antoon Lorentz and Pieter Zeeman were honored "in recognition of the extraordinary service they rendered by their researches into the influence of magnetism upon radiation phenomena" [Nobelprize.org, 1902] with the Nobel Prize in Physics. On top of this, Otto Stern received the Nobel Prize in Physics for the year of 1943 "for his contribution to the development of the molecular ray method and his discovery of the magnetic moment of the proton" [Nobelprize.org, 1943], but it was awarded in 1944 retrospectively. In the same year and with a matching topic, Isidor Isaac Rabi was also awarded the Nobel Prize in Physics "for his resonance method for recording the magnetic properties of atomic nuclei" [Nobelprize.org, 1944]. The discovery of NMR was finally celebrated in 1952, when Felix Bloch and Edward Mills Purcell received the Nobel Prize in Physics "for their development of new methods for nuclear magnetic precision measurements and discoveries in connection therewith" [Nobelprize.org, 1952]. Soon some applications of NMR became interdisciplinary, for instance by the findings of Richard Robert Ernst, who got the Nobel Prize in Chemistry "for his contributions to the development of the methodology of high resolution nuclear magnetic resonance (NMR) spectroscopy" [Nobelprize.org, 1991] in 1991. And the latest Nobel Prize, Nobel Prize in Chemistry, in the field of NMR was awarded to Kurt Wüthrich "for his development of nuclear magnetic resonance spectroscopy for determining the three-dimensional structure of biological macromolecules in solution" [Nobelprize.org, 2002] in the year 2002.

To explain how NMR works, this section will introduce the spin and the magnetic moment attached to it in section 2.1.1. Section 2.1.2 outlines how a macroscopic magnetization forms from this. How the equation of motion behaves is shown on section 2.1.3. At the end, section 2.1.4 deals with the phenomena of transverse and longitudinal relaxation.

2.1.1 Spin and Magnetic Moment

All atomic nuclei consist of nucleons, namely protons and neutrons, giving the nucleus physical properties such as a mass and a charge. With all of these nucleons being fermions, an additional solely quantum mechanical property of an angular momentum called spin $\vec{I}$ must further be assigned to each. The spin of a nucleon comprises the intrinsic and the orbital angular momentum. For an uneven number of protons and/or neutrons the vector sum of all nucleonic spins is different from zero and hence, the nucleus carries a net spin.

Attached to this spin is a magnetic moment $\vec{\mu}$:

$$\hat{\vec{\mu}} = \gamma \hat{\vec{I}} \tag{2.1}$$

with

$$\gamma = g\frac{\mu_\mathrm{K}}{\hbar} \text{ and } \mu_\mathrm{K} = \frac{q}{2m_\mathrm{r}}\hbar \ . \tag{2.2}$$

The proportionality factor γ is called gyromagnetic ratio and is a characteristic constant for a certain nucleus (e. g. $\gamma(^1H) = 267.522 \times 10^6\,\mathrm{rad/sT}$ [Levitt, 2008]). It has a significant impact on the nuclear magnetic resonance sensitivity (see section 2.1.2) as well as on the

behavior of spins interacting with external magnetic fields (as shown in section 2.1.3). The gyromagnetic ratio can be derived from the LANDÉ g-factor g, the nuclear magneton μ_K and the reduced PLANCK constant $\hbar$. The nuclear magneton itself is defined as the ratio of the charge q and the rest mass m_r (e. g. for a proton $m_\mathrm{p} = 1.673 \times 10^{-27}\,\mathrm{kg}$ [Beringer, 2012]). In comparison to an electron with a rest mass of $m_\mathrm{e} = 9.109 \times 10^{-31}\,\mathrm{kg}$ [Beringer, 2012], the nuclear magneton of a proton is by a factor of $\frac{m_\mathrm{p}}{m_\mathrm{e}} \approx 1836$ smaller than the BOHR magneton [Haacke et al., 1999]. The same accounts for the scaling of the magnetic moments.

Mathematically, a spin can be described by the algebra of a state vector $|j, m\rangle$ with the spin quantum number j, the secondary spin quantum number $m \in -j, -j+1, \ldots, j$, and the z-axis as the quantification-axis:

$$\hat{\vec{I}}^{\,2} |j, m\rangle = \hbar^2 j(j+1) |j, m\rangle \quad \text{and} \tag{2.3}$$

$$\hat{I}_z |j, m\rangle = \hbar m |j, m\rangle \quad , \tag{2.4}$$

holding the validity of the following commutator relations:

$$[\hat{I}_a, \hat{I}_b] = i\epsilon_{abc}\hbar\hat{I}_c \quad \text{and} \tag{2.5}$$

$$[\hat{I}_a, \hat{\vec{I}}^{\,2}] = 0 \quad . \tag{2.6}$$

For protons, with $j = \frac{1}{2}$, m can only take two possible values. In empty space, the energy levels are independent of the secondary spin quantum number and are therefore $(2j+1)$-fold degenerated. By applying an external magnetic field though, this degeneration is countermanded as described by the ZEEMAN effect.

The interaction of a magnetic moment of a nucleus with a net spin and the external magnetic field $\vec{B}$ can be expressed via the HAMILTON operator $\hat{\mathcal{H}}_\mathcal{Z}$. With the definition of the magnetic moment from equation 2.1, and the assumption of a constant $\vec{B}$ pointing in the z-direction, $\hat{\mathcal{H}}_\mathcal{Z}$ ends in:

$$\hat{\mathcal{H}}_\mathcal{Z} = -\hat{\vec{\mu}} \cdot \vec{B} \tag{2.7}$$

$$= -\gamma \hat{\vec{I}} \cdot \vec{B} \tag{2.8}$$

$$= -\gamma \hat{I}_z B_0 \quad \text{with} \quad \vec{B} = (0, 0, B_0) \quad . \tag{2.9}$$

Since $\hat{\mathcal{H}}_\mathcal{Z} \propto \hat{\vec{I}}$ in this case, the eigenstates of the spin from equations 2.3 and 2.4 are also eigenstates of the HAMILTON operator:

$$\hat{\mathcal{H}}_\mathcal{Z} |j, m\rangle = -\gamma \hat{I}_z B_0 |j, m\rangle \tag{2.10}$$

$$= -\gamma\hbar m B_0 |j, m\rangle \quad . \tag{2.11}$$

According to the time-independent SCHRÖDINGER equation and equation 2.11, the energy levels E_m are obtainable by:

$$\hat{\mathcal{H}}_\mathcal{Z} |j, m\rangle = E_m |j, m\rangle \quad \text{and} \tag{2.12}$$

$$E_m = -\gamma\hbar m B_0 \quad . \tag{2.13}$$

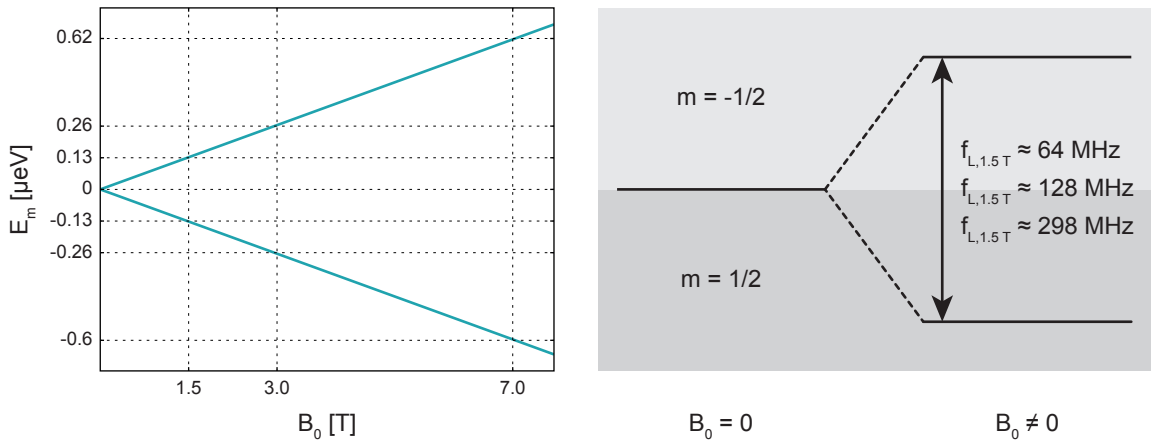

(a) (b)

Figure 2.1: Zeeman effect: (a) The energy E_m and the photonic band gap of the two Zeeman levels of a proton increase with an increasing magnetic field strength B_0. (b) So does the passage frequency f. At a magnetic field strength of 7.0 T, f comes out to approximately 298 MHz.

All neighboring energy levels are equidistant with a difference in the secondary spin quantum number of $\Delta m = 1$. The energy gap ΔE_m between the Zeeman levels is therefore given by:

$$\Delta E_m = -\gamma\hbar\Delta m B_0 \tag{2.14}$$
$$= -\gamma\hbar B_0 \tag{2.15}$$
$$= \hbar\omega_{\mathcal{L}} \ . \tag{2.16}$$

From here, the resonance frequency, or so called Larmor frequency $\omega_{\mathcal{L}}$, can be assessed and set into relation with the magnetic field strength:

$$\omega_{\mathcal{L}} = \gamma B_0 \ . \tag{2.17}$$

Again, for protons there is only one photonic band gap and the Larmor frequency at different B_0 accounts to $f_{1.5\,\mathrm{T}} = 63.86\,\mathrm{MHz}$, $f_{3.0\,\mathrm{T}} = 127.73\,\mathrm{MHz}$, and $f_{7.0\,\mathrm{T}} = 298.03\,\mathrm{MHz}$, respectively.

2.1.2 Macroscopic Magnetization

Although each spin must be considered to be independent of its neighbors, in typical nuclear magnetic resonance volume elements of at least the order of cubic millimeter, the entity of spins forms a spin ensemble. This spin ensemble can be treated as a thermodynamic reservoir holding the Fermi-Dirac statistics. With temperatures T around the Fermi temperature, this statistic devolves to the Boltzmann distribution:

$$P(E_m) = \frac{e^{-E_m/k_B T}}{Z} \tag{2.18}$$
$$= \frac{e^{\gamma\hbar m B_0/k_B T}}{Z} \quad \text{with} \quad Z = \sum_m e^{\gamma\hbar m B_0/k_B T} \ ; \tag{2.19}$$

$P(E_m)$ being the probability of a spin in the eigenstate E_m, $k_\mathcal{B}$ the BOLTZMANN constant and Z the partition function. The normalized occupation numbers N_{top}/N and N_{bottom}/N of the two energy levels of protons unfold to:

$$\frac{N_{\text{top}}}{N} = \frac{e^{\frac{1}{2}\gamma\hbar B_0/k_\mathcal{B}T}}{N} \text{ and} \tag{2.20}$$

$$\frac{N_{\text{bottom}}}{N} = \frac{e^{-\frac{1}{2}\gamma\hbar B_0/k_\mathcal{B}T}}{N} \tag{2.21}$$

with

$$N = e^{\frac{1}{2}\gamma\hbar B_0/k_\mathcal{B}T} + e^{-\frac{1}{2}\gamma\hbar B_0/k_\mathcal{B}T} \ . \tag{2.22}$$

The ratio of the occupation numbers η denotes the availability of spins for a NMR experiment. Below, the hyperbolic tangent is expanded to a TAYLOR series and approximated:

$$\eta = \frac{\Delta N}{N} = \frac{e^{\frac{1}{2}\gamma\hbar B_0/k_\mathcal{B}T} - e^{-\frac{1}{2}\gamma\hbar B_0/k_\mathcal{B}T}}{e^{\frac{1}{2}\gamma\hbar B_0/k_\mathcal{B}T} + e^{-\frac{1}{2}\gamma\hbar B_0/k_\mathcal{B}T}} \tag{2.23}$$

$$= \tanh \frac{\frac{1}{2}\gamma\hbar B_0}{k_\mathcal{B}T} \tag{2.24}$$

$$\approx \frac{1}{2}\frac{\gamma\hbar B_0}{k_\mathcal{B}T} \ . \tag{2.25}$$

The expansion holds for the high-temperature approximation with $T > 10^{-4}\,\text{K}$. For typical *in vivo* temperatures in the range of 310 K, the ratio of occupation numbers for protons at different magnetic field strengths takes values of $\eta_{1.5\,\text{T}} = 4.94 \times 10^{-6}$, $\eta_{3.0\,\text{T}} = 9.89 \times 10^{-6}$, and $\eta_{7.0\,\text{T}} = 23.07 \times 10^{-6}$, respectively.

The results above point out the sensitivity issue with NMR, as only the difference in spins of the occupation numbers contributes to the signal. To obtain the macroscopic magnetization $\vec{M}$, which scales directly with the signal (see section 2.2.2), the vector sum of all expectation values of the magnetic moments included within a volume element V needs to be calculated:

$$\vec{M} = \frac{1}{V}\sum_i^N \langle\hat{\vec{\mu}}_i\rangle \tag{2.26}$$

$$= \frac{1}{V}\sum_i^N \gamma\,\langle\hat{\vec{I}}_i\rangle \ . \tag{2.27}$$

The expectation values of the x- and y-component vanish. With the considerations from section 2.1.1, the expectation value of the z-component I_z is given by:

$$\langle I_z\rangle = \frac{\gamma\hbar^2 j(j+1)}{3k_\mathcal{B}T}B_0 \ . \tag{2.28}$$

Still fulfilling the high-temperature approximation, the absolute macroscopic magnetization M_0 is pointing in z-direction while being in the thermal equilibrium and can be derived from:

$$M_0 = \frac{1}{V}\frac{\gamma^2\hbar^2 j(j+1)}{3k_\mathcal{B}T}B_0\sum_i^N 1 \tag{2.29}$$

$$= \frac{N}{V}\frac{\gamma^2\hbar^2 j(j+1)}{3k_\mathcal{B}T}B_0 \ . \tag{2.30}$$

2.1.3 Equation of Motion

There are two possible perspectives to the movement of the macroscopic magnetization: the quantum mechanical or the semiclassical one. Quantum mechanically, the temporal evolution of the expectation values of the magnetic moments is described by the Liouville von Neumann equation:

$$\frac{\partial \langle \hat{\vec{\mu}} \rangle}{\partial t} = \langle -\frac{i}{\hbar}[\hat{\vec{\mu}}, \hat{\mathcal{H}}_{\mathcal{Z}}] \rangle \quad . \tag{2.31}$$

Taking the commutator relations from equations 2.5 and 2.6 and the definition of the Hamilton operator from equation 2.7 into account, the expression above can be rephrased to:

$$\frac{\partial \vec{\mu}}{\partial t} = \vec{\mu} \times \gamma \vec{B} \quad . \tag{2.32}$$

An equation of motion for the macroscopic magnetization can be defined from the sum over all magnetic moments, see equations 2.26, and above:

$$\frac{\partial \vec{M}}{\partial t} = \vec{M} \times \gamma \vec{B} \quad . \tag{2.33}$$

Treating the spin $I = \frac{1}{2}\hbar$ ensemble as a semiclassical system still holds the correct quantum mechanical considerations. This is due to the temporal characteristics of the expectation values of the spins as dealt with in the Ehrenfest theorem. It describes how the magnetic moment with an angular momentum behaves. From classical electrodynamics it is known that a torsional moment $\vec{N}$ is working on a magnetic moment inside an external magnetic field:

$$\vec{N} = \vec{\mu} \times \vec{B} \quad . \tag{2.34}$$

The angular momentum of a spin system is changed in time by such:

$$\frac{\partial \vec{I}}{\partial t} = \vec{N} \quad . \tag{2.35}$$

Combining the two equations 2.34 and 2.35 from above with the correlation of the magnetic moment to a spin from equation 2.1, the temporal evolution of a magnetic moment and the macroscopic magnetization can be defined analogous to equations 2.32 and 2.33, respectively. With $\vec{B} \parallel \vec{M}$ and $\vec{M} = \vec{M}_0$ in thermal equilibrium, the temporal derivative vanishes and $\vec{M}$ is constant in time. To distort the state of the system, the effective magnetic field needs to have a component vertical to $\vec{M}$.

In other words, the macroscopic magnetization is rotating, or precessing, around the magnetic field (see figure 2.2). Such behavior can be compared to the motion of a tumbling spinning top. To simplify this observation, a rotating reference frame shall be introduced. Its rotation axis $\vec{\Omega}$ is parallel to $\vec{B}_0$ linking $(x', y', z' = z)$ to the stationary reference frame (x, y, z) in the following manner:

$$\left.\frac{\partial \vec{M}}{\partial t}\right|_{\text{rot}} = \vec{M} \times (\gamma \vec{B} + \vec{\Omega}) \tag{2.36}$$

$$= \vec{M} \times \gamma \vec{B}_{\text{eff}} \quad . \tag{2.37}$$

The effective magnetic field $\vec{B}_{\text{eff}}$ dictates the precession axis in the rotating reference frame. There are two contributing fields to it:

$$\vec{B}_{\text{eff}} = \vec{B}_0 + \vec{B}_1 \tag{2.38}$$

with

$$\vec{B}_0 = \begin{pmatrix} 0 \\ 0 \\ \frac{\Delta\omega}{\gamma} \end{pmatrix} \text{ and } \vec{B}_1 = \begin{pmatrix} B_1 \sin(\phi) \\ B_1 \cos(\phi) \\ 0 \end{pmatrix} \ ; \tag{2.39}$$

$\Delta\omega$ being some off-resonance to the rotation frequency, $\vec{B}_1$ an additional external field from a transmit coil (see section 3.1.2) with the amplitude B_1 and the transverse phase ϕ to the x-axis. If the resonance condition $\vec{\Omega} = \gamma\vec{B}_0$ is fulfilled, the phase of the B_1 can, with no loss of generality, be set to zero and the equation of motion can be simplified to:

$$\left.\frac{\partial\vec{M}}{\partial t}\right|_{\text{rot}} = \vec{M} \times \begin{pmatrix} B_1 \\ 0 \\ \frac{\Delta\omega}{\gamma} \end{pmatrix} \ . \tag{2.40}$$

Again, the macroscopic magnetization is precessing around the effective magnetic field as shown in figure 2.2(c). One of two special cases occurs with $B_1 = 0$. Now, the macroscopic magnetization is constant in time, see figure 2.2(a). The second case happens when the resonance condition $\Delta\omega = 0$ is satisfied. Here, the magnetization is turning in the y/z-plane, see figure 2.2(b). All of this accounts for the assumption that the spins are isolated from each other.

2.1.4 Transverse and Longitudinal Relaxation

Spins do interact with each other as well as with the micro-environment, and this causes a fading of the precession motion. The entropy is maximized when the macroscopic magnetization is in thermal equilibrium. Hence, a disturbed spin ensemble will always return to this state. To describe such a process of relaxation, Bloch introduced empirically derived terms parameterized by the two constants T_1 and T_2 [Bloch, 1946]. These lead to differential equations called Bloch equations:

$$\frac{\partial M_x(t)}{\partial t} = \omega_{\mathcal{L}} M_y(t) - \frac{M_x(t)}{T_2} \ , \tag{2.41}$$

$$\frac{\partial M_y(t)}{\partial t} = -\omega_{\mathcal{L}} M_x(t) - \frac{M_y(t)}{T_2} \text{ and} \tag{2.42}$$

$$\frac{\partial M_z(t)}{\partial t} = \frac{M_0 - M_z(t)}{T_1} \ ; \tag{2.43}$$

M_0 still denotes the macroscopic magnetization in thermal equilibrium or in context with the relaxation process $M(t \to \infty) = M_0$. Simplifying the mathematical model into a transverse and a longitudinal magnetization $M_\perp$ and $M_\parallel$, the solution to the Bloch equations comes out as a set of exponential functions:

$$M_\perp(t) = M_\perp(0) e^{-i\omega_{\mathcal{L}} t} e^{-t/T_2} \text{ with } M_\perp(t) = M_{xy}(t) = M_x(t) + iM_y(t) \text{ and} \tag{2.44}$$

$$M_\parallel(t) = M_\parallel(0) e^{-t/T_1} + M_0(1 - e^{-t/T_1}) \text{ with } M_\parallel(t) = M_z(t) \ . \tag{2.45}$$

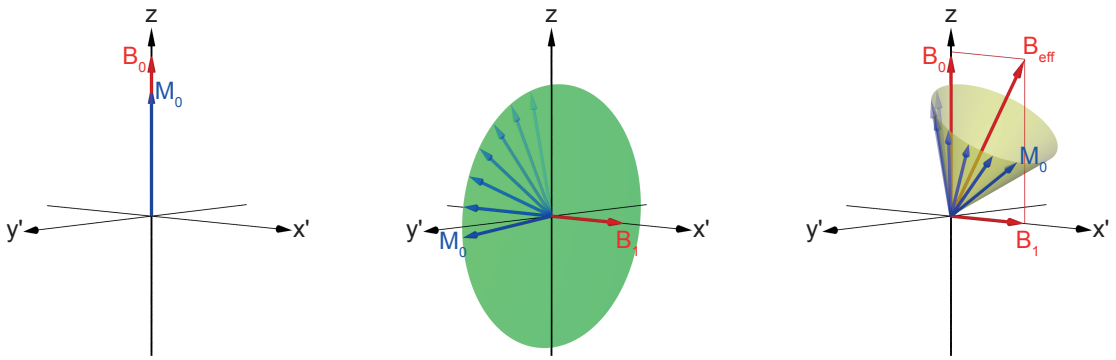

(a) (b) (c)

Figure 2.2: Temporal evolution of the magnetization: (a) In presence of a static magnetic field B_0 (red), the magnetization M_0 (fading blue) is pointing into the z-direction and is resting in the rotating reference frame. (b) An external RF field B_1 (red), on-resonant with the observed spins, rotates the magnetization around an axis in transverse plane on a circular plane (green). (c) A effective magnetic field B_{eff} (red) consists of both contributions of (a) and (b). The resulting effective field can point into an arbitrary direction with a precessing motion of the magnetization. Here, the magnetization occupies the curved surface area of a cone (yellow).

The motion described by equation 2.44 can be interpreted as a precession of the transverse magnetization around the z-axis of the rotating reference frame with the LARMOR frequency while decaying to zero with the time constant T_2 which may now be called transverse relaxation time, illustrated in figure 2.3(a). In a similar manner, the longitudinal component of the magnetization is building up, or returning, to its equilibrium magnetization exponentially with the longitudinal relaxation time T_1, shown in figure 2.3(b). These two phenomena can be explained in the following ways.

Transverse Relaxation The transverse magnetization is the sum of coherent spins or magnetic moments. Spin-spin interactions, or in the case of protons dipole-dipole interactions, cause a loss of this coherence. For this reason the transverse relaxation is also called spin-spin relaxation. There is no transfer of energy taking place. Moreover, the system is not just striving for a minimum in energy but a maximization of entropy.

Longitudinal Relaxation In contrast to the transverse component, the longitudinal magnetization is solely due to the difference in the occupation numbers of the ZEEMAN levels (see section 2.1.2). Microscopic movement of the molecules due to thermal processes causes fluctuations in the local magnetic field. Because of this, a transfer of energy from the spins to the micro-environment accompanied by a transition of the ZEEMAN levels is induced. The recovery of the occupation numbers to the state described by the BOLTZMANN statistics is the result. Giving the micro-environment the name of a lattice, the longitudinal relaxation can also be addressed with the synonym spin-lattice relaxation.

For human tissue, the relaxation times range from a few to many hundreds milliseconds for T_2 and up to a few seconds for T_1. A further analysis of the temporal magnetic field

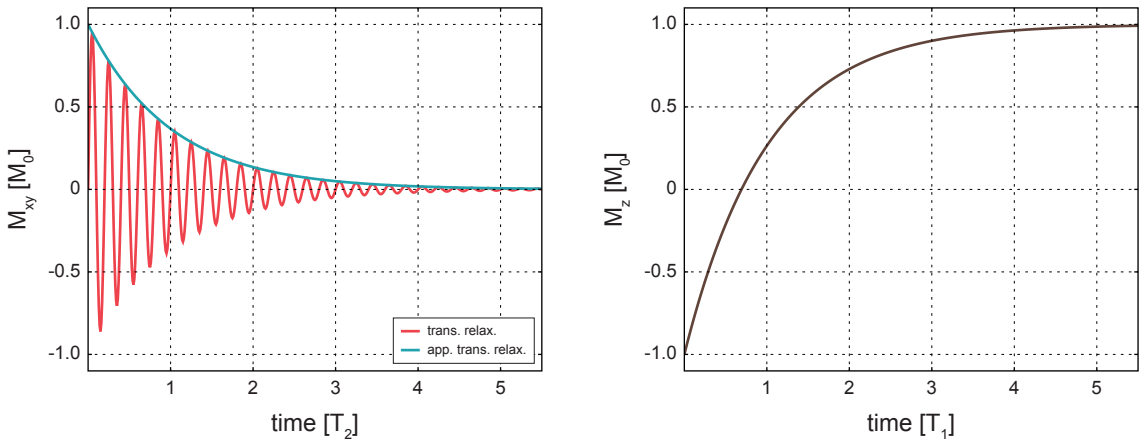

(a) (b)

Figure 2.3: Transverse and longitudinal relaxation: (a) A transverse component of the macroscopic magnetization M_{xy} decays with the time constant T_2. Spin interactions cause a dephasing, named spin-spin relaxation, of the spin ensemble (blue line). Additionally, inhomogeneity in the local magnetic field fans out the spins due to a change in the LARMOR frequency. The absolute value of the transverse magnetization is oscillating (red line). (b) A deflected z-component of the macroscopic magnetization M_z returns to its equilibrium state M_0 with the time constant T_1 (brown line). All spins align according to their surrounding and the relaxation process is called spin-lattice relaxation.

inhomogeneity reveals a dependency of the relaxation times on the magnetic field strength itself. In both cases, the processes of relaxation are irreversible.

While observing the transverse component of the macroscopic magnetization after disturbance, the apparent decay is faster than described by the spin-spin relaxation. The origin lies in the spatial inhomogeneity of the static magnetic field ΔB_0. With a variation in the LARMOR frequencies, the spin ensembles fan out or dephase. The absolute value of the transverse magnetization is additionally oscillating besides the exponential decay of the spin-spin relaxation. This process is often referred to as apparent transverse relaxation or T_2^* relaxation. The correlation of T_2 and T_2^* can be outlined by:

$$\frac{1}{T_2^*} = \frac{1}{T_2} + \gamma \Delta B_0 \ . \tag{2.46}$$

This equation is based on a simplified model and is not generally admitted. It is clear that $T_2^* \leq T_2$. By using any kind a refocusing strategy (e. g. a spin echo pulse), the spins can be rephased. Now the absolute value of the transverse magnetization is only diminished by the spin-spin relaxation.

2.2 Magnetic Resonance Imaging

One of the most important applications of nuclear magnetic resonance lies in the field of clinical diagnostics. With the advancement to magnetic resonance imaging, spatially resolved signal acquisition in terms of tomography has become available. MRI makes use of non-ionizing radiation and yields an excellent soft tissue contrast, allowing for the clear

differentiation and classification of pathologies. “For their discoveries concerning magnetic resonance imaging” [Nobelprize.org, 2003], Paul Lauterbur and Sir Peter Mansfield have been awarded the Nobel Prize in Physiology or Medicine in the year 2003.

The concept of MRI can be split into two parts: on one side, the manipulation of the macroscopic magnetization, imprinting a contrast and making the magnetization available for detection as described in section 2.2.1, and on the other side, the spatially resolved signal acquisition, encoding the spatial information and detecting the signal as delineated in section 2.2.2. With various combinations of these two parts, MRI offers a large number of acquisition techniques and contrasts as outlined in section 2.2.3.

2.2.1 Radio Frequency Pulses

A radio frequency pulse can be of any shape and intended function. Common to all is the generation of the electromagnetic wave by a transmit coil (examples are shown in section 3.1.2) and the characterization by its amplitude and frequency behavior in time as well as its initial phase. Throughout this section, some very basic pulses must hold as examples and only a short outlook will provide a more general understanding.

Constant Frequency Pulses One of the two prominent pulse classes is the one of constant frequency. In a most simple application, an radio frequency (RF) pulse is used to globally tip the macroscopic magnetization $\vec{M}$ from its equilibrium state. Its amplitude B_1 is of a rectangular shape and its frequency ω is chosen in such a way, that it matches the spin's Larmor frequency. Such a pulse is shown in figure 2.4(a). Again, this means that the resonance condition $\Delta\omega = 0$ is satisfied and equation 2.40 simplifies to:

$$\left.\frac{\partial \vec{M}}{\partial t}\right|_{\text{rot}} = \vec{M} \times \begin{pmatrix} B_1 \\ 0 \\ 0 \end{pmatrix} \quad . \tag{2.47}$$

Only the pulse amplitude is defining the effective magnetic field $\vec{B}_{\text{eff}}$ and hence the precession motion. The angle by which the magnetization is rotated around the x-axis is called tip- or flip angle α. For a constant pulse amplitude of a given duration τ, the tip angle can be calculated by:

$$\alpha = \gamma \tau B_1 \quad . \tag{2.48}$$

It scales directly with the gyromagnetic ratio γ and the product of the pulse amplitude and duration. Yet, as B_0 underlies spatial variations and additional magnetic gradient fields are used in magnetic resonance imaging (see section 2.2.2), $\Delta\omega$ can become different from zero and contribute to the effective magnetic field. This z-component of B_{eff} tilts the rotation axis out of the transverse plane despite the phase of the pulse. For this general case, equation 2.48 from above does not hold. However, a good estimate for the tip angle of off-resonant spins is given by the Fourier transform of the RF envelope, shown in figure 2.4(b), within the small tip angle approximation; $\sin(\alpha) \approx \alpha$ and $\Delta M_z \approx 0$. The frequency bandwidth Δf_{BW} or full width at half maximum (FWHM) of the frequency profile of a rectangular pulse therefore nearly equals the inverse duration:

$$\Delta f_{\text{BW}} = \frac{1.21}{\tau} \quad , \tag{2.49}$$

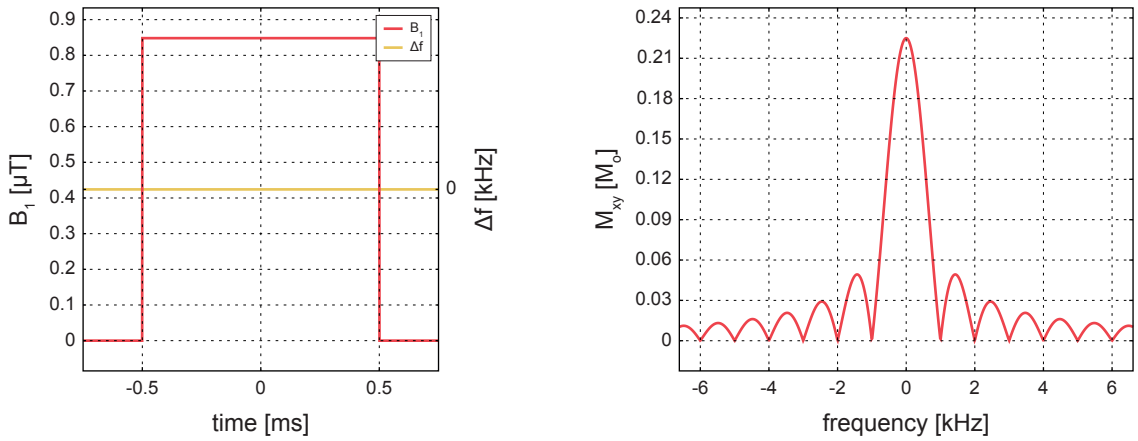

(a) (b)

Figure 2.4: Schematic of a rectangular RF pulse: (a) Both, amplitude B_1 (red) and off-resonance Δf (yellow) of a rectangular pulse are shown. The amplitude is chosen in such a way, that for a pulse duration of 1 ms the associated tip angle comes out to 13 °. (b) Its FOURIER transform can be described by a sinc function and reveals the transverse magnetization M_{xy}. With a FWHM of 1.21 kHz and numerous sidebands; off-resonant spins will also be manipulated.

and its shape is the one of a cardinal sine (sinc) function. Such short rectangular pulses are used to uniformly manipulate transverse magnetization in a non- or volume-selective manner as done in 3D imaging.

To manipulate spins within a very well defined band of frequencies, a different pulse is used. As the FOURIER transform needs to be of a rectangular shape, the pulse amplitude must be described by a sinc function, see figure 2.5(a). With a non-constant amplitude however, the tip angle cannot be calculated by equation 2.48. Yet, the pulse can be subclassified into a number N of rectangular pulses of finite duration $\Delta\tau$, yielding a total tip angle of:

$$\alpha = \gamma \sum_{i}^{N} B_{1,i} \Delta\tau_i \ , \tag{2.50}$$

and with its conversion into the integral form:

$$\alpha = \gamma \int_{0}^{\tau} B_1(t) \mathrm{d}t \ . \tag{2.51}$$

In general, the tip angle for pulses of this class and on-resonant spins is proportional to the area under the RF envelope. Regarding the FOURIER transform of a sinc pulse, so is the rectangular shape only valid for a temporally infinite sinc pulse. In reality, the duration of an RF pulse is limited though and as a consequence wiggles and sidebands occur across the frequency profile. The more side lobes the sinc pulse has, or the higher the dimensionless bandwidth-time product is, the less pronounced these distortions are; see figure 2.5(b). Additionally, the pulse is apodized by a HAMMING or HANNING windowed filter. The width of the manipulated frequency band is inverse proportional to half of the duration of

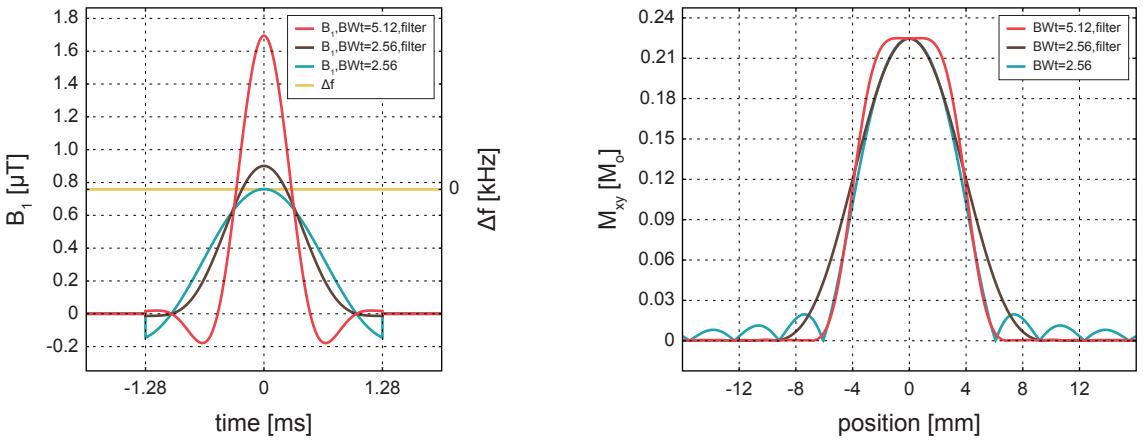

(a) (b)

Figure 2.5: Schematic of a sinc RF pulse (a) Different amplitude shapes B_1 (blue, brown, red) and off-resonance Δf (yellow) of a sinc pulse are shown. Peak amplitudes are chosen in such ways that for a pulse duration of 2.56 ms the associated tip angles come out to 13 °. The pulses differ in the value of the dimensionless bandwidth-time product (blue and brown: 2.56, red: 5.12) and the applied filter function (blue: without, brown and red: HAMMING filter). (b) To keep the slice thickness constant at 8 mm, the amplitude of the slice selection gradient (not shown) has been adapted. Its FOURIER transform can be approximated by a rectangular function. Limitations of the temporally limited RF pulse in terms of wiggles and sidebands (blue) of the transverse magnetization M_{xy} can be countermanded with a filter functions (brown) and a higher bandwidth-time product (red).

the central lobe t_0 of the sinc trajectory:

$$\Delta f_{\mathrm{BW}} = \frac{1}{t_0} \ . \tag{2.52}$$

Sinc pulses are used as slice-selective excitation pulses with small tip angles in 2D imaging.

Adiabatic Pulses As a second, and totally different pulse class, adiabatic pulses must be listed. The concept of an adiabatic pulse is based not only on the variation of the amplitude in time, but also on a complementary frequency modulation. When the pulse is subclassified again, not only does the rotation angle change but so does the rotation axis. If the direction of the rotation axis changes slowly enough compared to the rotation angle, the following rules apply:

- Magnetization parallel to the effective magnetic field will stay parallel
- Magnetization anti parallel to the effective magnetic field will stay anti parallel
- Magnetization perpendicular to the effective magnetic field will stay perpendicular

Mathematically this condition, also called adiabatic condition, can be described by:

$$\left| \frac{\partial \Psi_{\mathrm{eff}}}{\partial t} \right| \ll \gamma |\vec{B}_{\mathrm{eff}}| \ , \tag{2.53}$$

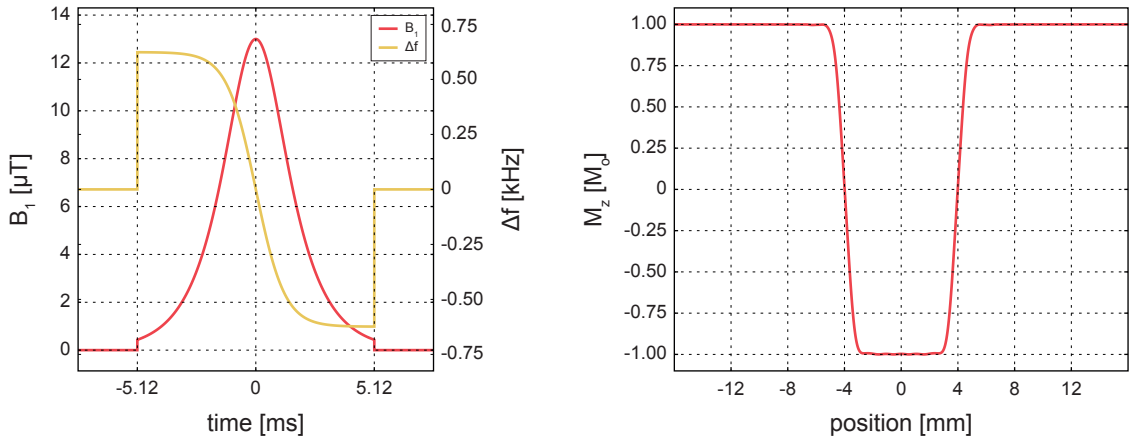

(a) (b)

Figure 2.6: Schematic of a HS RF pulse (a) Both, the amplitude B_1 form and the frequency modulation Δf are described by a hyperbolic secant and a hyperbolic tangent function, respectively. The tip angle is not depending on the integral of the pulse envelope, but on the interplay of B_1 and Δf. In this case, the pulse affects the magnetization as an slice-selective inversion. (b) The resulting slice profile of 8 mm thickness cannot be approximated by the FOURIER transform of the RF element and needs to be simulated via the BLOCH equations. A HS slice profile features sharp ridges and a homogeneous inversion efficiency within a range of B_1 values.

with Ψ_{eff} being the azimuthal angle of $\vec{B}_{\text{eff}}$. It is easily seen, that the tip angle has a much more complex dependency as on- and off-resonant conditions exist throughout the RF pulse. These pulses are designed for a specific manipulation of the magnetization and may not be interchangeable by simply stretching or scaling the RF envelope.

To exemplify the rules from above, the following considerations need to be taken into account. In case of the first or second rule, the situation can be compared to one in which the RF pulse is always strongly off-resonant. The magnetization sticks to the rotation axis of the effective magnetic field and precesses around it. The transverse component changes only within a limited range of phases. The accumulated phase of the magnetization is nearly the same as for $\vec{B}_{\text{eff}}$ and its final state is very well defined indifferent of B_0 and/or B_1 uncertainties. In a case of the third rule, the situation is completely different. Here, the pulse is continuously on-resonant despite the change of the rotation axis. The magnetization is strongly precessing around the effective magnetic field, rapidly changing its transverse component through the complete angular range. This behavior is called adiabatic fast passage. Within the pulse, the transverse magnetization accumulates a phase that strongly depends on the local conditions.

Adiabatic pulses can be classified into excitation, saturation, inversion, and refocusing pulses. Depending on the intention behind the pulse, the three different concepts are used. For saturation and inversion pulses, the accumulated phase does not play a role. Typically these pulses are used for the preparation of the magnetization and are followed by a spoiling gradient, destroying only residual transverse coherence. Any kind of adiabatic concept may be applied and one typical example is the hyperbolic secant (HS) pulse shown in figure 2.6 [Silver et al., 1984]. For excitation and refocusing pulses, the phase does play a major role. Arbitrary tip angles with pulses of this class can only be achieved by multiple

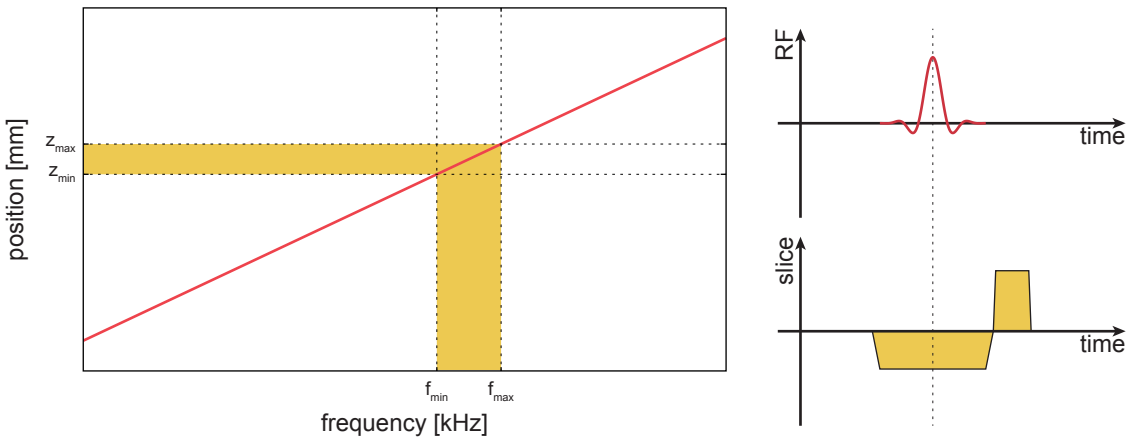

(a) (b)

Figure 2.7: Slice selection scheme: (a) There is a linear relationship between the frequency bandwidth and the spatial position. The width of the slice is given by the gradient amplitude. (b) From the center of the pulse, the transverse magnetization is accumulating an additional phase. Before the signal is detected, this phase needs to be rephased by a second gradient with half of the zero order moment and opposite polarity of the slice selection gradient.

pulses, making use of all adiabatic principles in combination with phase jumps. Finally, to refocus a spin ensemble, the effect of the pulse has additionally to be indifferent of the magnetization's initial phase.

Spatially Selective Pulses Some pulses allow for the use in 2D imaging. For 2D imaging, an additional modification to the local magnetic field must be done. To select and manipulate only a certain region within the field of view (FOV), in most cases a slice, a spatially varying linear magnetic gradient field must be played out into the slice direction. This gradient changes the LARMOR frequency along its direction and assigns an off-resonance to a certain position in space. The profile width Δz scales with the gradient amplitude in the following manner:

$$\Delta z = \frac{2\pi \ \Delta f_{\mathrm{BW}}}{\gamma G_z} \ , \tag{2.54}$$

G_z is the gradient amplitude in slice direction. The stronger the gradient is, the narrower the resulting profile will be; see figure 2.7(a).

During the RF pulse however, the gradient also causes a dephasing of the transverse magnetization. To refocus these oscillations after the RF irradiation has been completely finished, a second gradient must be played out. In a first approximation, its zero order moment must be have half of the slice selection moment with opposite polarity; see figure 2.7(b). A pulse can only be used for slice selection if either the imprinted phase can be rewound or the pulse is self-refocusing.

Advanced Pulses To understand how RF pulses work in detail, the concept of excitation k-space has to be understood as introduced by Pauly [Pauly et al., 1989]. The pulse amplitude, frequency, and phase as well as the accompanying gradient can be of an arbitrary shape but must fulfill the small tip angle approximation. If the pulse is observed

in k-space, it can be seen how a trajectory evolves. For a rectangular pulse this is a dot in k-space center and for a slice-selective sinc pulse this is a sinc function along the slice direction with its maximum in k-space center. The inverse FOURIER transform reveals a weighting matrix for the magnetization in position space. More pulse classes such as variable-rate pulses, composite pulses, and multi-dimensional pulses have been developed this way. For optimization, there are many techniques available such as the analytical approach of the SHINNAR-LE ROUX (SLR) algorithm [Shinnar et al., 1989; Le Roux, 1986] and several improvements of it [Shinnar and Leigh, 1989; Pauly et al., 1991]. Alternatively, numerical optimizations [Ugurbil et al., 1987, 1988; Conolly et al., 1988] can be performed via a genetic algorithm (GA) [Goldberg and Holland, 1988] or optimal control theory (OCT).

2.2.2 Spatial Coding and Data Acquisition

With a part of the macroscopic magnetization $\vec{M}$ in the transverse plane, a signal S is available for detection. In general, it can be mathematically described by:

$$S(t) = c \iiint M_{\perp}(\vec{r},t) B_1^-(\vec{r},t) e^{-i\phi(\vec{r},t)} \mathrm{d}x\mathrm{d}y\mathrm{d}z \ , \tag{2.55}$$

with c being a technical scaling factor, $M_{\perp}$ the transverse magnetization, B_1^- the coil sensitivity profile, and ϕ the transverse phase of $\vec{M}$. All excited magnetization vectors within the field of view, meaning with nonzero entries in B_1^-, contribute to the signal. In order to resolve this superposition of all the acquired information spatially, some kind of encoding must be performed. This can be explained more easily if the signal is observed in k-space. The FOURIER transformed magnetization unfolds to a frequency distribution. Instead of labeling the axes of this k-space with k_x, k_y, and k_z, as if they were spatial directions, logical denotations will be assigned respectively: readout or frequency encoding (RO), phase encoding (PE), and slice-selection (SS) or partition encoding (PART) (depending on whether it is a 2D or 3D imaging technique).

One role of magnetic gradient fields has briefly been touched before (see section 2.2.1), but another main application will be delineated here. The LARMOR frequency of the spins is influenced, by superimposing the static magnetic field B_0 with a spatially varying linear magnetic gradient field $\vec{G}$. During a time frame t, off-resonant spins with a frequency $\omega_{\mathcal{L}}$ accumulate a transverse phase ϕ. By deliberately switching the gradient fields, a pattern of ϕ values can be imprinted in position space $\vec{r}$:

$$\phi(\vec{r},t) = \int_0^t \omega_{\mathcal{L}}(\vec{r},t')\mathrm{d}t' \tag{2.56}$$

$$= \gamma\vec{r} \cdot \int_0^t \vec{G}(t')\mathrm{d}t' \ , \tag{2.57}$$

or with the definition of a wave vector $\vec{k}$:

$$\vec{k}(t) = \frac{\gamma}{2\pi} \int_0^t \vec{G}(t')\mathrm{d}t' \ , \tag{2.58}$$

the phase can be also expressed in k-space by:

$$\phi(\vec{r},t) = 2\pi\ \vec{r}(t)\cdot\vec{k}(t)\ . \tag{2.59}$$

Thus, the temporal evolution of the signal itself is strongly depending on the played out gradient field:

$$S\left(\vec{k}(t)\right) = \iiint M_{\perp}(\vec{r},t)e^{i2\pi\ \vec{r}(t)\cdot\vec{k}(t)}\mathrm{d}x\mathrm{d}y\mathrm{d}z\ . \tag{2.60}$$

The covered path in k-space is called a k-space trajectory. Time is parameterizing the phase entries along this trajectory and relaxation effects in $M_{\perp}$ of a given tissue. By means of a phase sensitive acquisition technique (quadrature detection) a complex signal can be acquired. The total measurement signal is the FOURIER transform of the spatial distribution of the magnetization, and hence its inverse FOURIER transform, holds the acquired image:

$$M_{\perp}(\vec{r}) \sim \iiint S(\vec{k})e^{i2\pi\ \vec{r}(t)\cdot\vec{k}(t)}\mathrm{d}k_x\mathrm{d}_y\mathrm{d}k_z\ . \tag{2.61}$$

In figure 2.8 it is shown, how k-space is holding the information of the image. While the center of k-space contains the low frequencies and the major part of the energy (see figures 2.8(a,b)), it dictates the intensity of the rather homogeneous areas. Reconstructing only this part of k-space will lead to a blurry but still similar image. The contribution of high frequencies in the outer rim of k-space (see figures 2.8(c,d)) is noticeable in the details of the image. Hence, a reconstruction of this region of k-space will only hold the changes of neighboring structures.

The two most prominent encoding techniques are readout or frequency encoding and phase encoding or partition encoding. The fundamental physical background of both methods is identical, yet the application of one or the other is clearly distinct.

Frequency Encoding Frequency encoding is nearly always performed into the readout direction with a constant amplitude gradient. For more complex gradient waveforms with a time varying direction and amplitude, please see the paragraph about advanced encoding below. In dependency on the size of the FOV and the spatial resolution, the data acquisition is divided into a number of N discrete sampling points. The speed in which k-space is traversed from a given starting point is defined by the gradient amplitude. Each sampling point's time frame τ is finite and hence always contains accumulated information from a segment of the k-space trajectory. A bandwidth Δf of a single k-space point can be defined in such a way, that:

$$\Delta f = \frac{1}{\tau} \tag{2.62}$$

or

$$\frac{\Delta f}{N} = \frac{1}{T_{\mathrm{acq}}}\ \text{with}\ T_{\mathrm{acq}} = N\tau\ , \tag{2.63}$$

with T_{acq} being the total acquisition time. One frequency encoding step always means that one complete k-space trajectory is acquired.

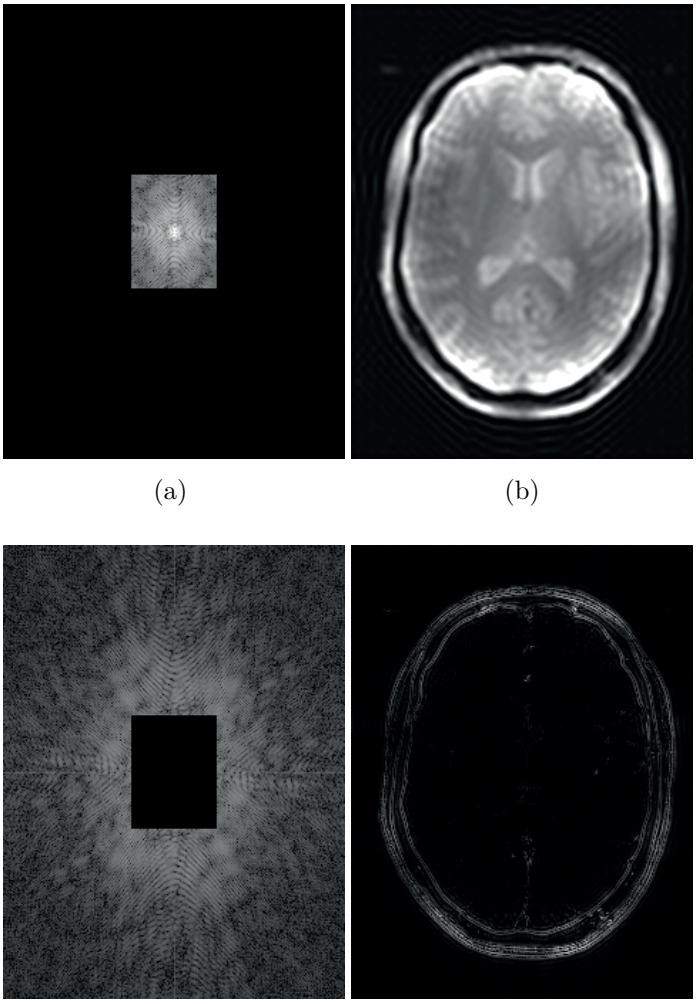

(a) (b)

(c) (d)

Figure 2.8: Imaging k-space: (a) The center of the imaging k-space is holding information about homogeneous structures. (b) By reconstructing only this region, the resulting image will appear blurry and ringing artifacts occur. (c) The outer rim of k-space holds the information about changes and hard edges. (d) An image reconstructed from this region will show the edges of the object.

Phase and Partition Encoding Without a net phase, a k-space trajectory always begins in k-space center. In order to select a starting point before frequency encoding begins, a different strategy must be pursued. Phase and partition encoding is usually performed in orthogonal directions to each other and the readout direction, spanning a three-dimensional Cartesian k-space. By playing out a gradient in either or both direction, k-space is traversed as well. The final position will not change any further as soon as the gradients have finished. This yields the starting point for the following frequency encoding step.

From the gradient-dependent maximum precession frequency and the NYQUIST-SHANNON sampling theorem, relationships between the distance in position of k-space sampling points $\Delta\vec{k}$ and the size of the FOV as well as the maximum $\vec{k}$ and the spatial resolutions Δx, Δy, Δz, can be expressed, respectively:

$$\Delta\vec{k} = \begin{pmatrix} FOV_x^{-1} \\ FOV_y^{-1} \\ FOV_z^{-1} \end{pmatrix} \tag{2.64}$$

and

$$2\vec{k}_{\max} = \begin{pmatrix} \Delta x^{-1} \\ \Delta y^{-1} \\ \Delta z^{-1} \end{pmatrix} \quad . \tag{2.65}$$

Advanced Encoding More advanced acquisition techniques to accelerate the imaging are the echo-planer [Mansfield, 1977] and echo-volumetric imaging [Mansfield et al., 1994]. The two strategies differ mainly in the usage as a 2D or 3D application. An excitation pulse is followed by a train of readout trajectories acquiring the complete k-space in a single shot (in 3D imaging a complete partition). Such imaging is applied for functional magnetic resonance imaging or diffusion weighted imaging. Besides the Cartesian readout, radial readout without [Lauterbur, 1973] and with density adaption [Nagel et al., 2009; Konstandin et al., 2011], spiral readout [Gatehouse et al., 1994; Glover and Lee, 1995; King et al., 1995], or twisted projection imaging [Boada et al., 1997] offer possibilities to shorten the timings between excitation and the acquisition of k-space center even further. The phase encoding and partition encoding steps can be omitted in 3D imaging. For 2D imaging the half-pulse concept offers a possibility to further shorten the echo timings by omitting the slice selection rephase gradient [MacFall et al., 1990].

A different way to accelerate the acquisition is via partial fourier imaging or parallel imaging. In the first case, not all of k-space is acquired, but as the k-space is HERMITIAN, missing information can be derived from redundant entries. This can be realized in two different manners: asymmetric echo or the actual partial fourier imaging. Parallel imaging is more sophisticated and relies on the availability of multiple overlapping receive elements. From the coil sensitivity profile, the spatial origin of a signal contribution can be isolated and regarded in the reconstruction algorithm. The two most prominent examples are generalized autocalibrating partial parallel acquisition (GRAPPA) [Griswold et al., 2002] and sensitivity encoding (SENSE) [Pruessmann et al., 1999].

2.2.3 MRI Sequences

If the two sections 2.2.1 and 2.2.2 above are combined and set in an adequate repetitive pattern, a magnetic resonance imaging sequence is the result. However, as outlined before, there are too many techniques in ongoing development to be covered within this section. As most of the work of this thesis relies on only one type of sequence, it shall be introduced here and presented in more detail within section 3.2.2.

Again for the most simple case, a tipping of the macroscopic magnetization from its equilibrium state is followed by the acquisition of one k-space trajectory. This progression is then repeated in such a way, that all of k-space is covered and the inverse FOURIER transform reveals the magnetic resonance (MR) image. The *fast low angle shot* (FLASH) technique was published in 1986 and gave rise to fast applications of magnetic resonance imaging in clinical routine [Haase et al., 1986]. In a more general context, this technique is often referred to as a spoiled gradient-recalled echo (GRE) sequence. By the use of only small tip angles, the major part of the macroscopic magnetization is left undistorted on the longitudinal axis. This way, the progression steps can be repeated without any additional waiting time for the $M_{\parallel}$ to build up again. A complete image with a resolution in the millimeter range can be acquired within a few seconds.

Numerous contrasts can be achieved by deliberately choosing the parameters, in particular the tip angle α and the echo and repetition time te and tr, of a FLASH sequence. Mathematically, the sequence signal equation can be expressed by:

$$S = \rho(M_0)\frac{1 - e^{-tr/T_1}}{1 - e^{-tr/T_1}\cos(\alpha)}e^{-te/T_2^*}\sin(\alpha) \ ; \tag{2.66}$$

ρ being a proportionality factor scaling with the longitudinal magnetization, and T_1 and T_2^* the longitudinal and apparent transverse relaxation time, respectively. Three different native contrasts can be created in the following way; see figure 2.9.

PD Weighted A long tr, short te, and small α will create a proton density (PD) weighted image. With $\cos(\alpha) \approx 1$, the repetition time and T_1-dependent terms from equation 2.66 cancel out leaving only a M_0 scaling with the echo time. If te is short enough compared to T_2^* though, this scaling will also clear out.

T_1 Weighted A short tr, short te, and large α will create a T_1 weighted image. The weighting of T_2^* can again be neglected due to the short echo time. Now, the reduced repetition time causes a weighting with T_1 as the approximation $\cos(\alpha) \approx 1$ is no longer valid though. The higher the tip angle becomes, the stronger this weighting will be.

T_2^* Weighted A long tr, long te, and small α will create a T_2^* weighted image. For the same reason as for the PD weighting, the long repetition time causes no weighting by T_1. The prolonged echo time causes a weighting by T_2^*.

Another much more distinct way to imprint a contrast into the image is by the use of an magnetization preparation (MP). A MP consists of radio frequency pulses, gradients, and timing intervals that are played out before the imaging begins. The two most prominent examples are the saturation recovery (SR) and inversion recovery (IR) experiments; see

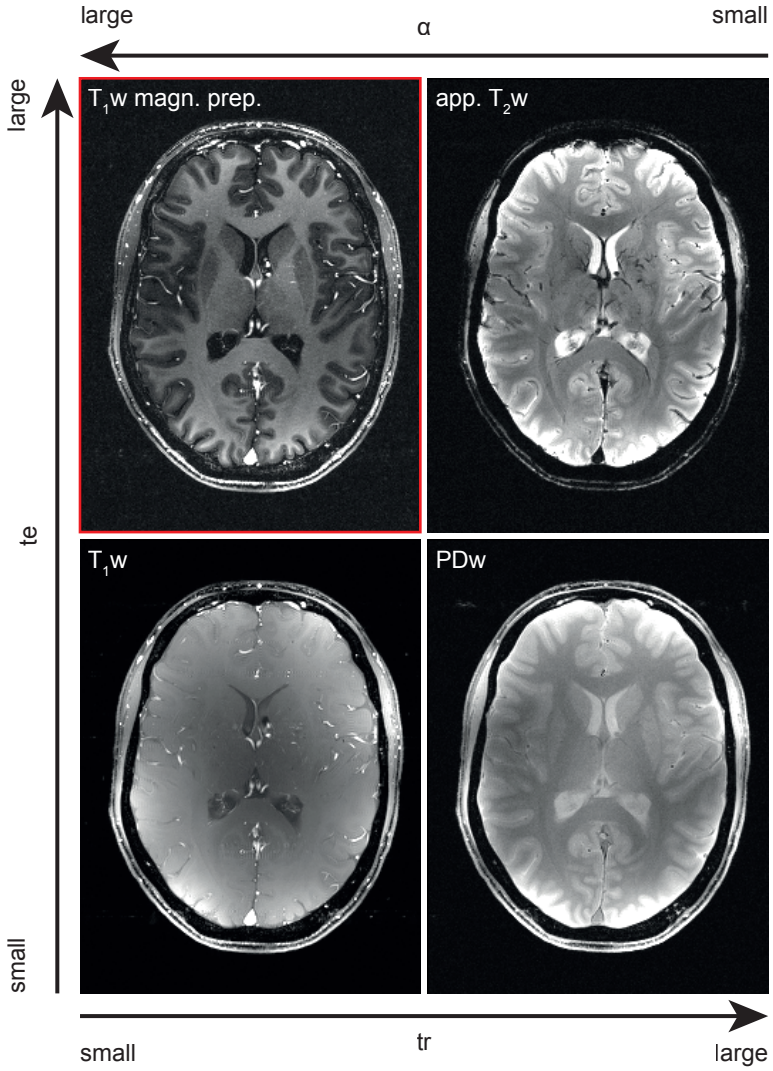

Figure 2.9: Imaging contrasts at 7 T: The FLASH sequence allows for numerous different contrast to be imprinted by simply adjusting the timing and tip angle parameters; soft tissue and/or liquid structures appear differently as a hypo- or hyperintense signal. All native T_1 contrasts lack distinctness at ultra high magnetic field strengths. Only with a magnetization preparation via an inversion pulse (red box) can a true T_1 contrast be imprinted, in this case an inverted white and gray matter signal intensity.

figure 2.9. A RF pulse is saturating or inverting the magnetization and is followed by a waiting time *TS* or *TI* respectively. During this period, the magnetization is relaxing and builds up its longitudinal component. The transverse component is dephased so that it does not step into appearance again. For two different tissue types with different longitudinal relaxation times T_1^a and T_1^b and within an IR experiment, the maximum contrast appears at:

$$TI = \ln\left(\frac{T_1^a}{T_1^b}\right)\frac{T_1^a T_1^b}{T_1^a - T_1^b} \ , \tag{2.67}$$

assuming complete relaxation between the preparation RF pulses.

2.3 Ultra High Field

This section is dedicated to the improvement of the field strength of the static magnetic field. Clinically applied magnetic resonance imaging systems embody magnets of field strengths in the range of 1.5 T to 3.0 T (so called high field systems). Everything above 4.0 T is commonly considered to be of ultra high field [Robitaille and Berliner, 2006]. Systems from 4.0 T to 7.0 T, as utilized for this thesis, to even higher field strengths of 9.4 T and 11.4 T have been tried in experimental studies. Despite the actual field strength, all considerations from the previous sections also apply for UHF magnetic resonance imaging but some additional remarks should be considered. Benefits and limitations come along with this advance and the latter needs to be overcome to establish this technology in clinical routine [Kraff et al., 2015].

The most obvious benefit is the impact of the magnetic field strength on the signal to noise ratio (SNR) as discussed in section 2.3.1. Not discussed within this thesis are the advantages for contrasting in functional magnetic resonance imaging [Ogawa et al., 1992] and native angiography such as time of flight (TOF) [Keller et al., 1989; Ruggieri et al., 1989] or arterial spin labeling (ASL) [Detre et al., 1992] imaging. On the other hand, inhomogeneity of the static magnetic field and the radio frequency field can impair the image quality significantly. This is shown in sections 2.3.2 and 2.3.3, respectively. The last remark in section 2.3.4 is made regarding the most important safety issue and reveals stronger constraints and limits in UHF magnetic resonance imaging.

2.3.1 Signal to Noise Ratio

The difference of occupations numbers of the Zeeman levels shifts with the amplitude of the static magnetic field B_0 as described by the Boltzmann statistics (see section 2.1.2). This is why future improvements of magnetic resonance technology greatly rely on stronger magnets. The relationship between B_0 and the signal to noise ratio can be outlined, as published by [Hoult and Lauterbur, 1979], by:

$$SNR \propto \frac{B_0^2}{\left(aB_0^{1/2} + bB_0^2\right)^{1/2}} \ ; \tag{2.68}$$

with a and b being technical scaling parameters. While the first part of the denominator is addressing signal losses due to RF hardware imperfection, the second part comprises losses

due to the sample object itself. For human magnetic resonance imaging, it is the second part of sample losses that dominates, but it also strongly depends on the coil concepts [Pohmann et al., 2015]. As a results, the signal to noise ratio scales nearly linearly with the magnetic field strength.

This increase in SNR can either be invested into a higher spatial resolution within the same acquisition time, or into a reduction of the acquisition time with the same spatial resolution. Furthermore, SNR sensitive acceleration techniques, such as parallel imaging or partial fourier imaging (see section 2.2.3), can be applied with higher acceleration factors. Finally, nuclei of lower sensitivity and lower concentration such as sodium, chlorine, and potassium, with relative signal strength in the range of 0.001 ppm to 1 ppm compared to a hydrogen signal, become available for detection [Madelin and Regatte, 2013; Konstandin and Nagel, 2014; Kraff et al., 2015].

2.3.2 Static Magnetic Field Inhomogeneity

Not only do imperfections of the static magnetic field B_0 cause inhomogeneity, but because of the high field strength, differences in the susceptibility $\Delta\chi$ of adjacent tissue types strongly impact on the image quality as well [Truong et al., 2006]. The field inhomogeneity ΔB_0 is defined by:

$$\Delta B_0 = \Delta\chi B_0 \ , \tag{2.69}$$

and causes the accumulation of an extra phase which leads to a signal cancellation and geometric distortions. Since human tissue is quite heterogeneous, these influences strongly depend on the spatial position and can hardly be corrected via additional tunable static magnetic fields. Such effects are especially apparent in the proximity of air filled cavities as in the case of the frontal sinuses. Applying stronger gradient helps to overcome part of this problem but cannot resolve it completely.

2.3.3 Radio Frequency Field Inhomogeneity

The wavelength λ of radio frequency pulses is inverse proportional to the static magnetic field B_0. At a field strength of 7 T and in empty space or air, it is in the order of $\lambda_{\text{air}} \approx 100\,\text{cm}$. Further, the wavelength also scales with the relative permittivity of a tissue ϵ_r in the following manner:

$$\lambda_{\text{tissue}} = \lambda_{\text{air}}/\sqrt{\epsilon_r} \ . \tag{2.70}$$

Assuming human tissue to be mainly similar to water (ϵ_{water} has a relative permittivity of 78), λ_{tissue} shortens to approximately 13 cm [Gabriel et al., 1996a,b,c]. This distance lies below the dimension of the human body. Hence, interferences of the primary RF wave and multiple reflections can occur. Constructive and destructive superposition is the result [Bottomley and Andrew, 1978]. Typically this can be observed as a hyperintensity in the brain center (central brightening), as a hotspot, at the tissue surface in proximity to the coil elements, or as a hypointensity [Truong et al., 2006]. This means, that the nominal tip angle, as it has been set within the sequence protocol, is not uniformly realized through the whole field of view. With more advanced coil concepts, the impact of these phenomena can be depleted.

2.3.4 Specific Absorption Rate

One of the two major safety issues for magnetic resonance imaging is the compliance with specific absorption rate limits [IEC, 2010]. All radio frequency pulses are partially absorbed by the tissue mass and lead to a warming. The physical unit which describes how much power is deposited per mass unit is called specific absorption rate (SAR). In the field of nuclear magnetic resonance, it can be calculated by:

$$SAR = \frac{E}{m_{\mathrm{r}}\tau} \tag{2.71}$$

$$= \frac{\sigma}{2\rho}|E_1|^2 \tag{2.72}$$

$$\propto |\omega_{\mathcal{L}} B_1|^2 \ ; \tag{2.73}$$

E is the absorbed energy, m_{r} and τ the mass and pulse duration, σ and ρ the electric conductivity and mass density, $\omega_{\mathcal{L}}$ the Larmor frequency, and E_1 and B_1 the electric and magnetic field strength of the RF wave, respectively. The SAR value increases with increasing $\omega_{\mathcal{L}}$ and hence with increasing B_0 [Bottomley and Andrew, 1978]. This leads to numerous limitations for the choice of pulse and timing properties, especially regarding the tip angle, in MRI sequences. It plays a major role as a constraint in pulse design and optimization.

3 Material and Methods

Within this chapter, the preexisting material and the applied methods as well as hardware developments and the implementations of the evaluation software are presented. At first, section 3.1 holds a list of hardware components and a description of the newly constructed measurement phantoms in section 3.1.4. Section 3.2 lists software programs and platforms operated in the context of this thesis as well as the implementations of magnetic resonance imaging (MRI) sequences in section 3.2.2. Finally, the chapter closes with section 3.4, giving a detailed description on the gold standard of quantitative imaging and fast mapping methods for the longitudinal relaxation time.

3.1 Hardware

3.1.1 Magnetic Resonance Tomograph

All measurements have been performed on a 7 T whole body magnetic resonance (MR) tomograph (MAGNETOM 7T; Siemens AG, Healthcare Sector, Erlangen, Germany) shown in figure 3.1. At the time of this thesis, it was of an experimental setup and not certified as a medical device. This means that regulatory guidelines by the German government allowed for human applications only within ethically approved studies.

The static magnetic field strength B_0 came out to 6.98 T and thus, the LARMOR frequency for protons $\omega_{\mathcal{L}}$ to 297.191 MHz. The system embodied a gradient system with the following maximum amplitudes and slew rates; see table 3.1. Eight power amplifiers offered the radio frequency (RF) system a total output power of 8 kW in combined mode. The system was non-actively shielded. The bore of the housing was 60 cm in diameter and 3 m long with a manually slidable patient table.

Figure 3.1: MAGNETOM 7T photography

Table 3.1: MAGNETOM 7T gradient specifications

	x-axis	y-axis	z-axis
maximum amplitude	40 mT/m	40 mT/m	45 mT/m
maximum slew rates	180 mT/m ms	180 mT/m ms	220 mT/m ms

3.1.2 Radio Frequency Coils

All MRI experiments within this thesis were performed by the use of one of the two following coils. They differ in the concept of construction, e. g. number of receive channels, and the type of application, e. g. as a volume resonator or as a surface coil. The main characteristics are shortly outlined; more information is given in the product manuals.

24-Channel Nova Medical Receive Array The first coil was a 24-channel transmit and receive coil from Nova Medical (Nova Medical Inc., Wilmington, Massachusetts, USA); see figure 3.2(b). It embodied a birdcage resonator as a transmit element and 24 small loop structures arranged as a half ball cup to receive the signal. Its field of view (FOV) was mainly defined by the receive loops. Smaller loops are limited in the penetration depth and hence, the FOV is not only limited in size but also feature an inhomogeneous receive field distribution. The signal to noise ratio (SNR), though, was improved compared to a single-channel coil with comparable volume coverage.

(a) (b)

Figure 3.2: Radio frequency coil photographies: (a) The 24-channel Nova Medical receive array is designed for brain imaging and (b) the 28-channel Siemens knee coil is designated for studies on the extremities.

28-Channel Siemens Knee Coil The second coil was a 28-channel transmit and receive coil from Siemens (Siemens AG, Healthcare Sector, Erlangen, Germany). By the concept of a cylindrical housing, the coil has been optimized for designated imaging of the human knee. As the Nova Medical coil, it also embodied a birdcage resonator as a transmit element and 28 loop structures for the receive path. It is shown in the results section 6.2.3 that the transmit field features a distinct inhomogeneity.

3.1.3 Computational Resources

All computational calculations were performed on either a standard desktop computer or on a high performance computing (HPC) cluster. The complexity estimations in section 4.1.6 are bases on the following hardware components.

PC The desktop computer, running Windows 7 Ultimate, was based on an x64-architecture and equipped with an Intel i7-2600 CPU at 3.40 GHz with 4/8 physical/logical cores, 32 GB of main memory, and besides a HDD for data storage with a 250 GB SSD hard drive for fast data logging.

HPC Cluster The HPC was manufactured by HP (Hewlett-Packard GmbH, Böblingen, Germany). To give easy access to various dynamic link libraries, the system was running Microsoft Windows Server 2008 R2 Enterprise. One head node was managing 4 worker nodes within a private 1000 MBit/s local area network. Again, the systems were based on an x64-architecture. All C/C++ and MATLAB jobs were handled via the Windows Server 2008 Task Scheduler.

The head node (HP ProLiant DL380 G7 LFF) was equipped with two Intel Xeon E5620 CPUs at 2.40 GHz with 4/8 physical/logical cores. Besides 24 GB of main memory, it employed a 1 GB flash backed cache. All data was stored on 300 GB SAS drives in a RAID 1 setup.

Each worker node (HP ProLiant SL170s) was holding two Intel Xeon E5649 CPUs at 2.53 GHz with 6/12 physical/logical cores; making 96 hyperthreaded cores in total. 2 GB

of main memory were assigned to each logical core, 48 GB to each worker node, and in total 192 GB to the complete HPC. As no data needed to be stored on the worker nodes explicitly, standard HDDs were sufficient.

3.1.4 Homogeneity and Contrast Phantoms

Two different phantoms were developed within this thesis. Special regard was given to produce well defined and reproducible conditions. The positioning of the phantoms was aided by an adjustable phantom table.

Homogeneity Phantom To create the most simple situation of a homogeneous phantom, a cylindrical housing of acrylic glass with a flat top and bottom was realized (see figure 3.4(a)). In numbers, the cylindrical barrel has an inner diameter of 123 mm, is 129 mm high, and the wall is 3 mm thick. Its bottom and top plate are 6 mm strong and detachable. On the topside, six indentations are distributed for the allocation on the phantom table and a flexible nozzle is mounted for the degasification. All contacts have been sealed with O-rings. With such a design, the phantom offers a cylindrical symmetry and distortion by the phantom housing are minimized. Two phantoms of this design have been built.

The first was filled with HiPerSolv CHROMANORM (VWR International GmbH, Darmstadt, Germany). HiPerSolv CHROMANORM is commercially available distilled water with a maximum contamination of 5 ppm. A degasification and slight mechanical vibration has been performed three times. The transverse and longitudinal relaxation times at 25 ° room temperature were determined to (1869±90) ms and (3223±15) ms, respectively. Water phantoms of this size show strong effects of RF interferences at a frequency of 300 MHz.

The second phantom is filled with ELBESIL B20 (L. Böwing GmbH, Flörsche, Germany). ELBESIL is a family of silicon oils with a silicon (Si) and oxygen (O) alternating backbone as shown in figure 3.3. Each silicon atom carries two or three methyl groups (CH3). The exact length of the bone is unknown as it is solely characterized by its physical properties. Its melting point lies at -55 °, its boiling point at 190 °, and the viscosity at room temperature is 20 mm^2/s. Only two different chemical shifts exist for the methyl groups depending on the position of the hydrogen (H) atom in the molecule; either at the end or middle section of the backbone. If the backbone is long enough, the signal contribution from the two methyl groups bound to the silicon will outweigh the two Si-3CH_3 groups. The result is a single MR resonance peak. This time, due to the small relative permittivity of 2.8, the RF field distribution is nearly homogeneous.

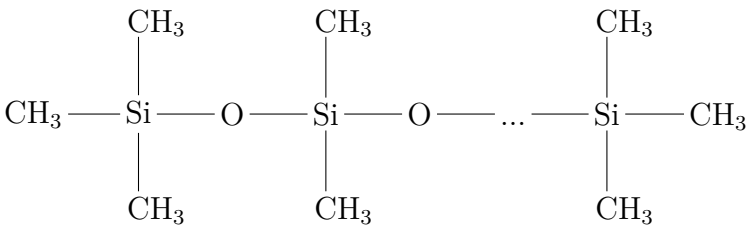

Figure 3.3: ELBESIL oil structural: Silicon (Si), oxygen (O), and methyl groups (CH3). Silicon oil has an alternating silicon-oxygen backbone of arbitrary length. For proton imaging, only two different chemical shifts of the hydrogen nuclei (H) contribute to the signal. Depending on the length of the backbone, one of the resonance frequencies will dominate.

(a) (b) (c)

Figure 3.4: Homogeneity and contrast phantom photographies: (a) The homogeneity phantoms are filled with HiPerSolv CHROMANORM and ELBESIL B20, (b) the contrast phantom is loaded with test tubes of Magnevist solutions of different concentrations and ELBESIL B20, (c) and a phantom table is used to reproducibly position the phantoms.

Contrast Phantom The second phantom concept holds for studies of the MR contrast due to the weighting of the longitudinal relaxation process. Its basis is the same as the homogeneity phantom from above. In extension, 13 test tubes, also made of acrylic glass and arranged in a hexagonal pattern, can be inserted into the top plate as shown in figure 3.4(b). Each test tube has an inner diameter of 21 mm, is 100 mm high, and its coat and the bottom plate are 1 mm thick. On the inside, a conical cavity is milled to guide air into the drill hole of a sealing screw. This way, it can be filled with a syringe, compressed by torquing down the screw, and the test tube will be void of air as a result.

The main compartment of the phantom was flooded with ELBESIL B20. Each test tube was filled with a different concentration of Magnevist (Bayer HealthCare AG, Leverkusen, Germany) solved in HiPerSolv CHROMANORM. Magnevist is the marketing name for gadopentetic acid, a gadolinium-based MRI contrast agent. The paramagnetic properties of the gadolinium cause a reduction of the longitudinal relaxation time. Mathematically, the following equation describes the relation between the actual longitudinal relaxation time T_1, the relaxation time in absence of the contrast agent $T_{0,1}$, and the concentration of gadolinium c_{Gd}:

$$\frac{1}{T_1} = \frac{1}{T_{1,0}} + R_1 \cdot c_{\mathrm{Gd}} \ , \tag{3.1}$$

with R_1 being the longitudinal relaxivity. While $T_{1,0}$ was measured, R_1 is determined by a linear regression to a set of measured T_1 values over the corresponding concentrations of the contrast agent. From the relaxation experiment at room temperature, the relaxivity was quantified to $3.44\,(\mathrm{mM\,s})^{-1}$. This value is in good agreement with the literature [Noebauer-Huhmann et al., 2010]. The targeted T_1 values were to range from 1200 ms to 2300 ms in steps of 100 ms (12 tubes) and one test tube of HiPerSolv CHROMANORM. Table 3.2 holds the actual T_1 and the accompanying T_2 values as well as the Magnevist concentrations.

Some remarks regarding T_2 must be made. For one, it is obvious that the transverse relaxation time is influenced by the contrast agent as well. Pure water has a long T_2 time,

Table 3.2: Parameters of the contrast phantom: Values for the longitudinal relaxation time T_1 were determined by an IR spin-echo experiment, the transverse relaxation time T_2 values by a multi-echo spin-echo experiment. The base solution of the contrast agent (CA) was of a 5 mM concentration. The concentration c_{Gd} and the respective masses m of water and the base solution are listed for each test tube.

test tube [#]	T_1 [ms]	T_2 [ms]	c_{Gd} [mM]	m_{H2O} [ml]	m_{CA} [ml]
1	3223±15	1869±90	0	250.000	0
2	2253±30	1407±55	0.041	163.286	86.714
3	2153±17	1422±36	0.048	174.297	75.703
4	2037±18	1418±32	0.055	183.615	66.385
5	1933±18	1209±18	0.062	191.601	58.399
6	1830±22	1237±20	0.071	198.522	51.478
7	1721±17	1292±38	0.080	204.578	45.422
8	1613±24	1158±17	0.091	209.922	40.078
9	1512±27	1113±15	0.103	214.672	35.328
10	1407±27	1048±15	0.117	218.922	31.078
11	1303±31	940±10	0.133	222.747	27.253
12	1217±37	961±13	0.151	226.208	23.792
13	1107±59	847±11	0.173	229.354	20.646

which is longer than typically encountered *in vivo* values in the order of a few hundred milliseconds. For the quantitative imaging experiments the long transverse relaxation times are not of any issue, because in *fast low angle shot* (FLASH) sequences T_2 only causes a constant signal scaling for each test tube.

Phantom Table A holding system was designed to position the phantoms in a reproducible manner. Comparable to the patient table, a phantom table adjustable in height and axial position is used. Figure 3.4(c) shows how the phantom table can directly be attached to the patient table and can be fixed to designated anchor points. The black structure is made of hardwood and the anchors of a nonmagnetic metal. Mounted on top is a backplate of poly(methyl methacrylate) (PMMA) and features an oblong hole to adjust the height. Two rods of arbitrary length serve as a distance marker between the backplate and the indentations in the phantom mentioned above. An overall positioning-error is in the range of less than a millimeter.

3.2 Software

3.2.1 Programs and Platforms

MathWorks MATLAB MATLAB (The MathWorks Inc, Natick, Massachusetts, USA) is commercial software used for solving mathematical problems. It is primarily using matrix operations to numerically approach the problem. The user is handling the software by a proprietary programming language. Smaller custom programs can be wrapped as a script or a function and object-oriented programming is also supported.

A large number of functions are already implemented within the framework. The platform is build up of the main program (MATLAB) and can be expanded by additional toolboxes. These toolboxes are usually assigned to specific topics (see below) and need to be licensed independently.

Within this thesis, the MATLAB release R2013a was used for all computations. Later releases were avoided for compatibility reasons of the code and hardware. Additionally, the following toolboxes, descriptions are taken from [MathWorks.com, 2015], were used:

- Input/output, visualization: Statistics Toolbox, Signal Processing Toolbox, Image Processing Toolbox, and Curve Fitting Toolbox.
- Optimization: Optimization Toolbox and Global Optimization Toolbox.
- Program acceleration: Parallel Computing Toolbox and MATLAB Coder.
- Stand-alone program: Compiler.

Besides the standard computer, MATLAB was also run on a HPC cluster as specified in section 3.1.3. For this reason, the MATLAB Distributed Computing Server was installed. It contains all toolboxes within the MATLAB family. A client can address it via the Parallel Computing toolbox. The jobs were handled by the Windows Server 2008 Task Scheduler.

The MATLAB Distributed Computing Server allows the execution of code on a cluster, either consisting of satellite computers and/or designated hardware grids and/or clouds. No modifications to the code need to be made as long as it can be executed parallelized on the client computer. Only a small overhead exists for communication reasons between a client and the server. In this way, high computational burden or a high demand of main memory can be handed to designated hardware.

DKFZ Image Processing Platform The DKFZ Image Processing Platform (DIPP) is a version of the Medical Imaging Interaction Toolkit (MITK) for in-house use only [MITK.org, 2015]. MITK is a free software library that comprises both the Insight Segmentation and Registration Toolkit (ITK) and the Visualization Toolkit (VTK). It simplifies the development of interactive programs and allows the execution within a graphical user interface. Another feature of MITK is the ability to generate workflows and to automate data evaluations.

For this thesis, the plug-in to run command line programs was of a major focus. This way, any programs generated by the MATLAB Compiler can be called. Input variables can be specified through customizable Extensible Markup Language (XML) based graphical user interfaces. The great benefit lies in the compatibility and so offered use of other MITK features such as image segmentation to produce binary image masks and registration to correct for motion. All of the evaluation routines from chapters 3 and 4 for MR images have been implemented into this framework.

Siemens IDEA Integrated Development Environment for Applications (IDEA) is the software platform from by Siemens (Siemens AG, Healthcare Sector, Erlangen, Germany) to give external sequence programmers the possibility to write custom pulse sequences. It is wrapped within the software package NUMARIS/4 and holds the Sequence Development Environment (SDE). The sequence language is ANSI-C++ and offers the user features like structure implementations and basic loops. To write image reconstruction algorithms,

the Image Calculation Environment (ICE) is used; the programming language is also ANSI-C++.

Custom sequences can be simulated with a Protocol Off-line Editing Tool (POET). This way, not only sequence patterns can be visualized, but safety issues can be calculated from heuristic models to respond to predefined sequence parameters. It allows the user to review sequence timings and any property of the sequence objects.

Autodesk Inventor Inventor is a software package by Autodesk (Autodesk Inc, San Rafael, California, USA) to create three-dimensional computer-aided design (CAD) constructions. Single elements and assemblies of elements can be created with the help of a graphical user interface.

Each element can be parameterized and rescaled at any point in time. This way, design drawing can be generated and the object of desire can be prototyped by a workshop or a 3D-printer.

3.2.2 MRI Sequences

Gradient Recalled Echo Sequence The FLASH technique is first listed in section 2.2.3 and examples of its importance for past and modern imaging are outlined in sections 3.3 and 3.4. It will also be the experimental backbone of all MRI experiments regarding quantitative imaging in section 4.2. Modern versions of the FLASH technique facilitate more efficient spoiling schemes than proposed in the original publication [Haase et al., 1986]. A framework with a great repertoire of flexible features, partially using existing routines by Siemens, has been implement and optimized for efficiency aspects. The basic concept is explained in more detail here.

At first, 2D imaging will be explained; a sequence diagram is shown in figure 3.5(a). As already described in section 2.2.1 about RF pulse elements, the magnetization is tipped from its longitudinal axis. This is usually done by a cardinal sine (sinc) shaped pulse (red RF element) accompanied by a slice-selection gradient (first yellow slice element) of a certain amplitude depending on the bandwidth-time product of the pulse and the slice thickness. From the center of the pulse, the isodelay point, an extra phase caused by the slice-selection gradient is accumulated. To compensate this phase and prevent signal loss, an additional gradient (second yellow slice element) with half of the zero order moment of the slice-selection gradient and opposite polarity is played out. The FLASH technique is usually performing a Cartesian k-space readout; logical read, phase, and slice directions are orthogonal (see section 2.2.3). A k-space line is selected by a phase tab (first blue phase element). In the same time frame, the read prephaser (first orange read element) moves the wave vector to one beginning of the phase line. The following readout gradient moves the wave vector along the phase line (frequency-encoding) and the evolving echo (blue RF element) is acquired by an analog digital converter (ADC) event (black boxed RF element). Eventually, the phase tab is reversed (second blue phase element) bringing the wave vector back to the k-space center line. Remaining transverse magnetization is completely dephased by spoiling gradients causing more than a 2π phase accumulation along the voxel dimensions. These gradients are usually played out on the read and slice direction (brown elements).

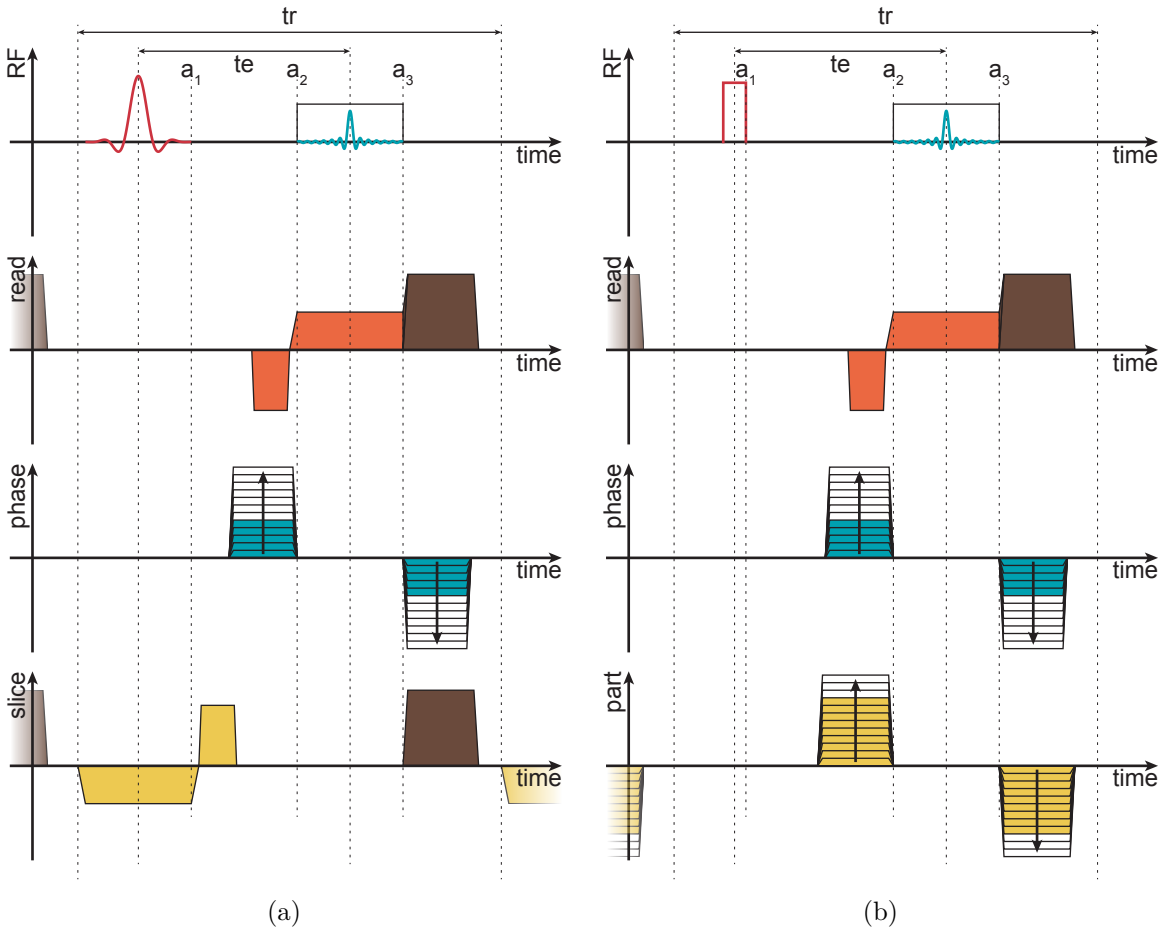

Figure 3.5: Diagram of a GRE sequence: The sequence can be classified into an RF channel (red/blue) as well as read (orange), phase (blue), and slice/partition (yellow) gradient channels. (a) 2D imaging: The RF pulse is accompanied by a slice selection gradient and immediately followed by the slice rephaser. A read prephaser and a phase tab set the starting point of the k-space trajectory. The k-space is traversed by the read gradient and the so formed echo is acquired by the ADC event. Finally the phase tab is rephased and all remaining transverse magnetization is spoiled in read and slice direction. (b) 3D imaging: The RF pulse can be slice- or volume-selective. The difference to the 2D mode lies is the gradient switching on the partition channel. A second phase-encoding is performed by a tab and a rephase tab; spoiling is omitted.

This pattern of RF and gradient elements is repeated in time. Important parameters are the echo time *te*, which is the time between the isodelay point and the center of the *k*-space line, the repetition time *tr* of the pattern, and the phase increment of the RF pulse from one pulse to the next. While the timings define the contrast imprinted into the image, the phase cycle causes an intrinsic destruction of remaining transverse magnetization. This method is called RF spoiling and causes a destructive interference across multiple pattern repetitions [Zur et al., 1991]. After all *k*-space lines are acquired, the image can by reconstructed by a two-dimensional FOURIER transform.

In order to minimize the effects and artifacts of motion and/or diffusion, the zero order moment of any gradient needs to be as short as possible. As a consequence, the gradients are aligned to certain anchor points within the sequence pattern. The slice rephaser starts at the end of the RF pulse (anchor point a_1). Both, the read prephaser and the phase tab end at the beginning of the ADC event (anchor point a_2), while the phase rephaser starts at the end of it (anchor point a_3). For the spoiling, it is not of any significance at which time point after the gradients begin or end, but for temporal efficiency, these usually start at the end of the ADC event.

For 3D imaging, the sequence needs to be adapted. Not only is a thin slice excited, but either a thick slab or the whole volume. In case of a slab selection, which is similar to a slice selection in the 2D mode, a sinc pulse with the accompanying gradient is used. A volume-selective mode usually makes use of a rectangular pulse without a gradient which is illustrated by the red RF element in figure 3.5(b). The main difference between the two modes is the encoding of the slice and partition direction, respectively. Section 2.2.2 already outlined the fact, how a partition line is encoded similar to the phase lines. Each partition line is selected and rephased by the partition tabs (first and second yellow partition element). The spoiling gradient (brown read element) is only applied in the read direction.

The pattern repetition and parameterization is analogous to the 2D mode. The image reconstruction is done by a 3D FOURIER transform. Also corresponding to the phase gradient alignment from above, the partition encoding gradients are anchored at the beginning and end of the ADC element (anchor points a_2 and a_3).

Additional features that have been implemented and operated within this thesis are listed below.

- excitation mode: If specific absorption rate (SAR) constraints are exceeded, the pulse duration can be prolonged. An intrinsic optimization of the pulse duration is performed for the sinc pulse. The bandwidth-time product is maximized depending on the slice thickness and taking the maximum gradient amplitude of the MR system into account; the duration can vary between 1.92 ms and 3.20 ms.
- gradient mode: All gradient timings have been optimized in the following two step process. First, any gradient is calculated to fit into a minimum time frame. This concerns the ramp times as well as the flat top time; all constraints are defined by the MR system. From the user defined timing parameters (within the dynamic limits), the final gradient timings are calculated to match the input and minimize artifacts but also have a minimum load of peripheral nerve stimulation (PNS).
- asymmetric echo: The read prephaser can be reduced to acquire only a certain segment of the phase line. A shorter echo time is the result (see section 2.2.2).

- partial fourier: This feature is implemented for the phase and, in case of 3D imaging, partition direction. For more information see section 2.2.2.
- elliptical scanning: The specified resolution in the image space is represented by the maximum wave vector in k-space. In 2D imaging this can be visualized by a circle and in 3D by a sphere. Entries in k-space outside these boundaries represent higher spatial resolutions than specified in the sequence protocol and can therefore be omitted. A shortening of the total acquisition time accompanied by a drop in SNR is the result.
- parallel imaging: This feature is part of an existing Siemens module and has been facilitated as described in section 2.2.2.
- flow compensation: The effects of flow have already been addressed above. To compensate the signal variations completely, all higher order moments of the gradients need to be rephased to zero. The most important one is the first order moment; it corresponds to contribution of a constant flow. Usually this is accomplished by using multiple gradients with a specific symmetry [Pattany et al., 1987; Haacke and Lenz, 1987; Wendt, 1991]. Although the nominal signal is increased and artifacts are reduced, the minimum timings are prolonged.
- parameter map: Custom parameters can be defined on a sheet of the user interface. An easy implementation is offered via the parameter map by Maxim Zaitsev.

Gradient Recalled Echo Sequence with Magnetization Preparation The FLASH technique lacks the ability to imprint a sufficient T_1 contrast at a magnetic field strength of 7 T; this can be seen in figure 2.9 of section 2.2.3. To improve this circumstance, the magnetization can be prepared (also shown in the listed figure from above). One example of such a preparation is exemplified by the inversion recovery (IR) experiment from section 3.4.1 and realized by an magnetization prepared rapid gradient echo (MPRAGE) sequence [Mugler and Brookeman, 1990]. A RF pulse is played out in a slice- or volume-selective manner with or without a gradient (first yellow slice element in figure 3.6). Figure 3.6 shows an exemplary rectangular preparation pulse (first red RF element). A spoiling gradient (first brown slice element) destroys the potentially existing transverse magnetization. The pulse is followed by a waiting time; in case of an inversion called inversion time TI. Within this time frame, the magnetization recovers according to it longitudinal relaxation time. Such a total block of a preparation and the readout is repeated with the period of the repetition time TR.

A second type of preparation is performed between the magnetization preparation, which is called outer preparation from now on, and the readout. This inner preparation can be a regional or spectral saturation as just two examples. The most prominent spectral saturation is the fat suppression. Depending on the spatial mode and the effect of the inner preparation, a slice selection gradient (second yellow slice element) and another spoiling gradient (second brown slice element) are played out along with the RF pulse. After all the preparation is done, the readout, in this case the FLASH technique, follows. A detailed explanation is given above.

The readout itself can be influenced by a number of options. The number of segments specifies how many k-space lines are acquired following one preparation. It can range from

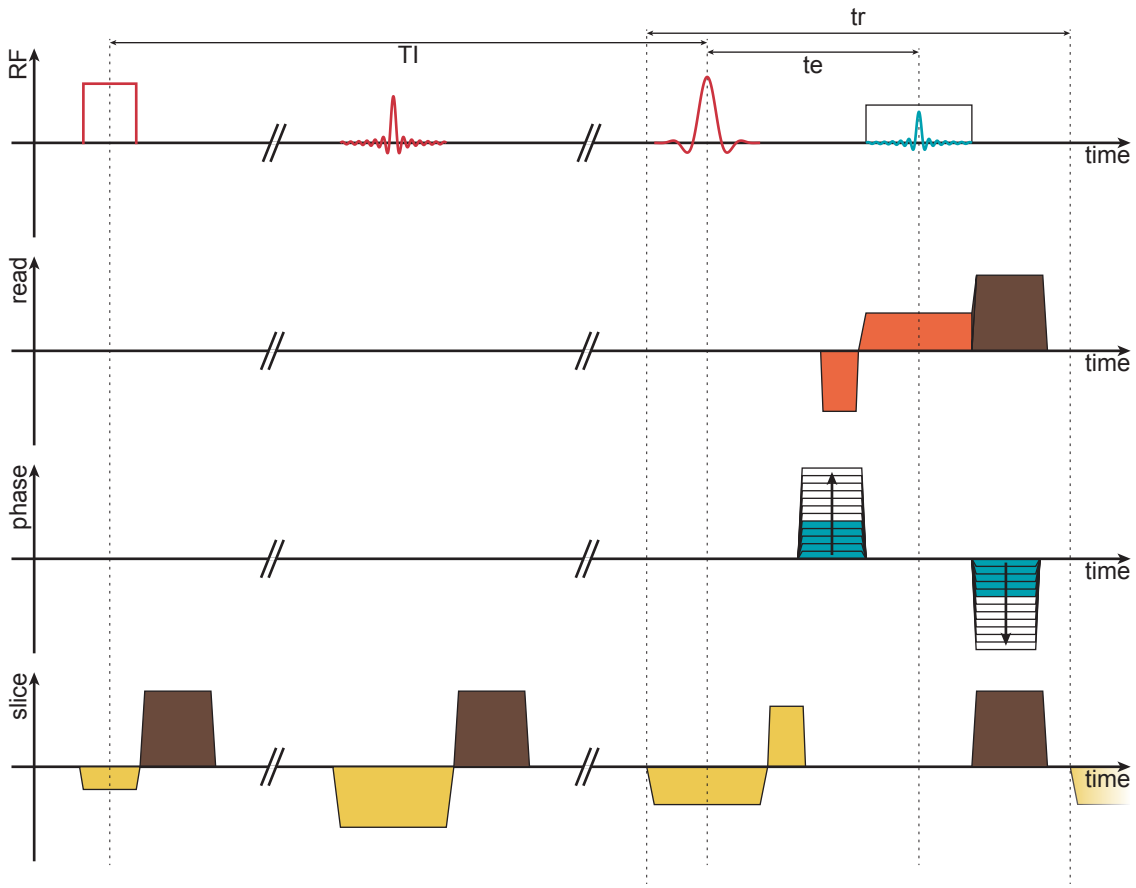

Figure 3.6: Diagram of a GRE sequence with magnetization preparation: The GRE sequence is proceeded by of block of preparation pulses. A description of the schematic is given in figure 3.5. The RF pulses can be slice- or volume-selective and are accompanied by gradients (yellow slice elements) and potentially succeeded by spoiling gradients (brown slice elements). The preparation is followed by a GRE sequence readout as illustrated in figure 3.5.

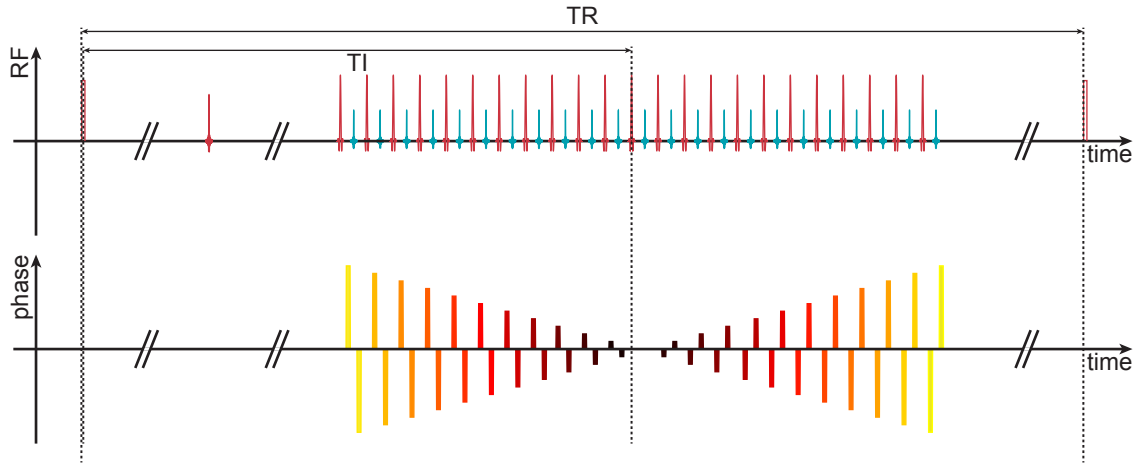

(a)

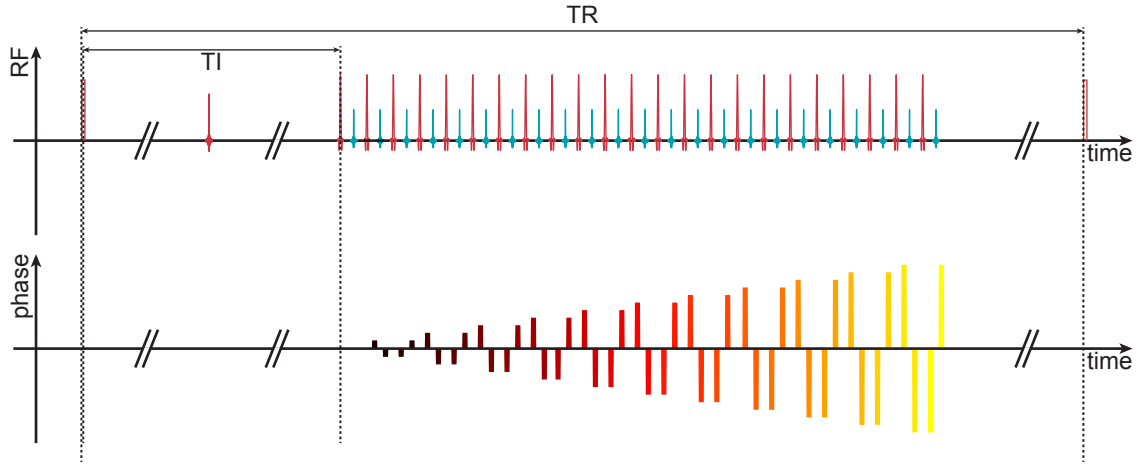

(b)

Figure 3.7: Ordering schemes of k-space: Lines of k-space can be acquired innermost first or linearly ordered. The coloring of the gradients in phase direction indicates the spatial frequency magnitude of the corresponding k-space line; yellow corresponds to high and black to low spatial frequencies. A description of the schematic is given in figure 3.5. (a) Linear ordering: The outermost k-space line is acquired first. The following lines are influenced by the proceeding readout blocks. (b) Centric ordering: k-Space center is acquired first. The acquired signal is mostly influenced by the contrast imprinted by a magnetization preparation.

a single shot sequence, where all k-space lines are acquired after a single preparation, to a single line readout. On one hand, this significantly influences the total acquisition time but on the other hand, the resulting contrast is also depending on the order of segmentation. The most important parameter is the ordering scheme. This scheme defines, in which pattern the k-space lines are acquired; whether the innermost or outermost lines are acquired first. Linear and centric reordering schemes are illustrated in figure 3.7. To understand the difference, two aspects must be considered. The k-space center line holds most of the energy and thus the information about the contrast. Each readout block influences the longitudinal state of the magnetization by the RF pulse and the repetition time. If linear ordering is exercised, the k-space center is in a distorted state at the time of acquisition and does not hold the theoretically expected signal value. With centric ordering, this instance is negligible to a certain degree. More detailed explanations and the consequences are given in section 4.2.5.

3.3 Parameter Uncertainties

3.3.1 Static Magnetic Field Inhomogeneity

In section 2.3.2, the issue with static magnetic field inhomogeneity, specifically at ultra high magnetic fields, has been introduced. To quantify these variation within the FOV, and hence regard it later on, a simple technique was applied.

From the definition of the equation of motion 2.40, it is known, that with the absence of an RF field component, the effective magnetic field is only defined by the off-resonance $\Delta\omega$: The greater the off-resonance, the stronger the precession motion. A phase $\Delta\phi$ is accumulated within a finite time frame t analogous to equation 2.57:

$$\Delta\phi = \int_0^t \Delta\omega(t')\mathrm{d}t' \ . \tag{3.2}$$

Hence, an off-resonance that is constant in time can be calculated by:

$$\Delta\omega = \frac{\Delta\phi}{t} \ . \tag{3.3}$$

This phase, though, is not only caused by off-resonance due to static magnetic field inhomogeneity, but can also have contributions from imperfect RF pulse effects. To neglect these effects, the phase needs to be determined at two different points in time t_1 and t_2. Both phases incorporate the same errors and only differ in the integral over t from above. The net off-resonance comes out as:

$$\Delta\omega = \frac{\Delta\phi_2 - \Delta\phi_1}{t_2 - t_1} \ . \tag{3.4}$$

This is computed on a pixel by pixel basis.

This technique is implemented in an MRI sequence by Siemens. It is based on the FLASH method with two contrasts. The time-points t_i are given by the echo times te_i. It is necessary, that the two echoes are acquired with the same gradient polarity to regard

chemical shift artifacts on the one hand. On the other hand, the difference in the echo times may not be too large, because phase wraps ($\Delta\phi$ >360 °) cannot be resolved. For practicability reason it is chosen in such a way, that the two fat signals are in phase.

3.3.2 Radio Frequency Field Inhomogeneity

Also in section 2.3.3, the misfit of RF field inhomogeneity is outlined. Destructive and constructive interferences cause spatial variation in the amplitude and the phase of the RF pulse and thus, the effective tip angle. To determine the actual tip angle, the following method was applied.

Taking the equation of motion 2.40 as the starting point again, on-resonant spins are tipped from the initial state by the magnetic component of the RF pulse (see equation 2.51). Any residual transverse magnetization is spoiled. The longitudinal component M_z is reduced proportional to the actual tip angle β:

$$M_z = M_0 \cos(\beta) \ . \tag{3.5}$$

It cannot be detected directly, and needs to be tipped into the transverse plane by the readout angle α to present the signal S:

$$S(\beta) = \rho(M_0) \cos(\beta) \sin(\alpha) \ . \tag{3.6}$$

This is only a rough approximation and neglects effects of the longitudinal and transverse relaxation. A detailed mathematical description is presented in section 3.4.1 about the IR experiment. From the ratio of two signals, one without preparation $S(0)$ and one with a non-zero tip angle $S(\beta)$, the problem turns out to:

$$\cos(\beta) = \frac{S(\beta)}{S(0)} \ . \tag{3.7}$$

As the signal is spatially resolved, a spatially resolved map of the actual tip angle is the result.

This is method is implemented in the Siemens work-in-progress sequence. The sequence is acquiring two contrasts: one with and one without a preparation. A preparation pulse is immediately followed by a single-shot FLASH readout train; k-space center line first. The second contrast is acquired in the same manner only with the tip angle of the preparation set to zero. All calculations are done by the reconstruction system and returned as a tip angle map in DICOM format.

3.4 Quantitative Imaging

The term quantitative imaging, also often called parameter mapping, refers to techniques that do not only reveal morphological structure as a contrast-weighted image, but give exact values of the physical parameters that cause the weighting. Such techniques hold far more information than conventional imaging. A weighted image can be considered to be a single snap-shot of a dynamic process, while a quantitative map can be considered as raw data; any weighted image can be calculated from here.

The characterization of relaxation times for example, allows a clearer discrimination of tissue types, the segmentation, and thus the classification of it. Furthermore, quantitative imaging allows for the comparison of the parameters within multi-site and longitudinal studies. With such a tool, diagnostics, therapy monitoring, as well as surgical planning and procedures could become more precise and thus be of a higher impact on the outcome. In-flow perfusion studies [Detre et al., 1992], dynamic contrast agent studies [Gowland et al., 1992], diagnosis of epilepsy [Pitkanen et al., 1996], and the determination of the severeness of PARKINSON's disease [Vymazal et al., 1999] are just a few examples.

This thesis deals with the quantitative determination of the longitudinal relaxation time. Three different methods will be introduced below. At first the gold standard and most accurate approach is outlined in section 3.4.1. Section 3.4.2 deals with a faster method that is based on the FLASH technique. And finally sections 3.4.3 and 3.4.4 show some further development to perform quantitative imaging at higher static magnetic field strengths.

3.4.1 Inversion Recovery

In section 2.1.4, the longitudinal relaxation and the corresponding BLOCH equation have been introduced. When deflected from its equilibrium state M_0, the longitudinal component of the magnetization M_z is building up again. Mathematically this can be described by equation 2.45:

$$M_z(t) = M_z(0)e^{-t/T_1} + M_0(1 - e^{-t/T_1}) \ ; \tag{3.8}$$

with T_1 being the longitudinal relaxation time, and t an elapsed time frame following the deflection. If the initial deflected state of M_z corresponds to a perfect inversion of the equilibrium magnetization, the equation from above simplifies to:

$$M_z(t) = M_0(1 - 2e^{-t/T_1}) \ \text{ with } \ M_z(0) = -M_0 \ . \tag{3.9}$$

By deliberately changing the time frame t, the so generated data of M_z can be fitted by an exponential curve revealing the longitudinal relaxation time T_1 besides other parameters.

The longitudinal magnetization cannot be measured directly, as the signal is proportional to the transverse component only (see section 2.2.2). In an inversion recovery experiment, the macroscopic magnetization is inverted by a preparation RF pulse. For practical reasons, this pulse is followed by a spoiler gradient; destroying a potentially remaining transverse component. After a waiting time, called inversion time TI, the resulting z-component of the macroscopic magnetization is tipped again by a readout RF pulse and detected as a signal S:

$$S_{\mathrm{IR}}(TI) = \rho(M_0)(1 - 2e^{-TI/T_1})\sin(\alpha) \ ; \tag{3.10}$$

with $\rho(M_0)$ being proportional to the equilibrium magnetization, TR the repetition time of the preparation block, and α the readout tip angle. Intentionally, all sequence parameters are selected in such a way, that any other weightings are minimized.

Since the magnetization needs to return to equilibrium before the next preparation block is executed, this method takes a long time. For a complete relaxation, approximately five

times T_1 has to go by. The longitudinal relaxation time of gray matter of the brain at a magnetic field strength of 7 T, for example, is around 2250 ms. This means, that the acquisition of a single-slice map takes time in the order of more than one hour. Volumetric measurements cannot be performed at all (except for slice-interleaved 2D mapping). This is one major reason why quantitative imaging is not applied in clinical routine yet.

3.4.2 DESPOT1

A fast method to map the longitudinal relaxation time T_1 has been revised and introduced again in 2003: driven-equilibrium single-pulse observation of T_1 relaxation (DESPOT1) [Deoni et al., 2003]. The approach with variable tip angles has first been published nearly 30 years earlier [Christensen et al., 1974] and further investigated by a number of researchers [Homer and Beevers, 1985; Homer and Roberts, 1987; Wang et al., 1987; Homer and Roberts, 1990].

DESPOT1 is also based on the FLASH technique mentioned in section 2.2.3. The signal S from equation 2.66 depends on a number of parameters:

$$S = \rho(M_0)\frac{1 - e^{-tr/T_1}}{1 - e^{-tr/T_1}\cos(\alpha)}e^{-te/T_2^*}\sin(\alpha) \ ; \tag{3.11}$$

with $\rho(M_0)$ being a factor proportional to the macroscopic magnetization in equilibrium, α the tip angle, te and tr the echo and repetition time, and T_1 and T_2^* the longitudinal and apparent transverse relaxation time, respectively. It is simplified by neglecting T_2^* contributions to:

$$S = \rho(M_0)\frac{1 - E_1}{1 - E_1\cos(\alpha)}\sin(\alpha) \ , \tag{3.12}$$

with

$$E_1 = e^{-tr/T_1} \ \text{ and } \ e^{-te/T_2^*} \to 1 \ \text{ for } \ te \to 0 \ . \tag{3.13}$$

For a fixed setup, meaning static FOV and constant te and tr, the signal only depends on α. The equation can be rewritten in a linear form:

$$\frac{S}{\sin(\alpha)} = E_1\frac{S}{\tan(\alpha)} + \rho(M_0)(1 - E_1) \ . \tag{3.14}$$

A linear regression is performed on the data of at least two different tip angles:

$$f(x) = ax + b \ , \tag{3.15}$$

revealing the desired parameters of the longitudinal relaxation time and the signal of the equilibrium magnetization:

$$T_1 = \frac{-tr}{\ln a} \ \text{ and } \ \rho(M_0) = \frac{b}{1 - a} \ . \tag{3.16}$$

An optimization of the distribution of the two tip angles showed, that it is ideal when the difference of the linearized data points is maximized on the one hand, and the signal itself is maximized for SNR reasons too. This is the case for tip angles smaller and larger than the Ernst angle with a signal of a factor of 0.71 of the signal at the Ernst angle itself [Wang et al., 1987; Deoni et al., 2003]. T_1 parameter maps at a magnetic field strength of 1.5 T of the whole brain with 1 mm isotropic resolution can be acquired within 13 min [Deoni et al., 2005]. The DESPOT1 method is widely used within clinical trials.

3.4.3 Three-Point DESPOT1

For the DESPOT1 method to work proper, the actual tip angle α needs to be known. In section 2.3.3, the misfit of inhomogeneous RF field distributions and variations of the tip angle has been outlined. In 2006, a three-point DESPOT1 approach was presented to overcome this problem [Li and Deoni, 2006]. Instead of regarding variations of α directly, the actual tip angle was handled by calculating the ratio of signal values of different nominal tip angles set within the sequence protocol.

Taking a look at the FLASH signal equation 3.12 from section 3.4.2, it becomes clear how the signal S only depends on the actual α value.

$$S = \rho(M_0)\frac{1 - E_1}{1 - E_1\cos(\alpha)}\sin(\alpha) \ ; \tag{3.17}$$

$\rho(M_0)$ being proportional to the equilibrium magnetization, and E_1 the T_1 weighting by the repetition time tr from section 3.4.2. Two ratios a_1 and a_2 can be computed from three measurements with the tip angles α, 2α, and 4α:

$$\frac{S(\alpha)}{S(2\alpha)} = a_1 \ \text{ and } \ \frac{S(2\alpha)}{S(4\alpha)} = a_2 \ , \tag{3.18}$$

so that:

$$a_1 = \frac{\sin(\alpha)\Big(1 - E_1\cos(2\alpha)\Big)}{\Big(1 - E_1\cos(\alpha)\Big)\sin(2\alpha)} = \frac{1 - E_1\Big(2\cos(\alpha)^2 - 1\Big)}{2\Big(1 - E_1\cos(\alpha)\Big)\cos(\alpha)} \ , \tag{3.19}$$

and

$$a_2 = \frac{\sin(2\alpha)\Big(1 - E_1\cos(4\alpha)\Big)}{\Big(1 - E_1\cos(2\alpha)\Big)\sin(4\alpha)} = \frac{1 - E_1\Big(2\cos(2\alpha)^2 - 1\Big)}{2\Big(1 - E_1\cos(2\alpha)\Big)\cos(2\alpha)} \ . \tag{3.20}$$

A polynomial expression is derived and simplified with the following two substitutions:

$$x = \cos(\alpha) \ \text{ and } \ \cos(2\alpha) = 2\cos(\alpha)^2 - 1 = 2x^2 - 1 \ . \tag{3.21}$$

Solving the polynomial on a pixel by pixel basis leads to the values of the longitudinal relaxation and equilibrium magnetization:

$$-4a_2x^4 + (4a_1 + 4a_1^2)x^3 + (4a_1 + 4a_2 - 2a_1a_2 - 1)x^2 + (1 - a_1 - a_2) = 0 \ . \tag{3.22}$$

The method was successfully applied *in vivo* at a static magnetic field strength of 7 T [Li and Deoni, 2006]. Effects such as central brightening could be corrected revealing maps with an accuracy of 0.1 s. Appearances of additional banding artifacts due to variations in the static magnetic field were reported. The temporal efficiency of the mapping method compared to standard DESPOT1 was reduced by 30 %.

3.4.4 DESPOT1-HIFI

An alternative approach to allow quantitative imaging at high static magnetic field strengths was presented in 2007. As an extension of DESPOT1 the DESPOT1 with high-speed incorporation of RF field inhomogeneities method makes use of different generations of the T_1 contrast within the experiment to regard variations in the actual tip angle α [Deoni, 2007].

The basis of the first part of the experiment is given by the DESPOT1 method and hence the FLASH technique. Its signal equation 3.12 from section 3.4.2:

$$S = \rho(M_0)\frac{1-E_1}{1-E_1\cos(\alpha)}\sin(\alpha) \ , \tag{3.23}$$

with $\rho(M_0)$ proportional to the equilibrium magnetization and E_1 the weighting of longitudinal relaxation time T_1 for a given repetition time tr, must be extended to incorporate tip angle variations:

$$S = \rho(M_0)\frac{1-E_1}{1-E_1\cos(\alpha_{\mathcal{T}})}\sin(\alpha_{\mathcal{T}}) \ \text{ with } \ \alpha_{\mathcal{T}} = \kappa\alpha \ , \tag{3.24}$$

with κ being a spatially varying scaling factor. The second contribution is given by an inversion recovery experiment as described in detail in section 3.4.1 above:

$$S_{\mathrm{IR}}(TI) = \rho(M_0)(1-2e^{-\mathcal{TI}/T_1}+e^{-\mathcal{TR}/T_1})\sin(\kappa\alpha) \ , \tag{3.25}$$

with TI being the inversion time, and TR the repetition time of the magnetization preparation. Least squares matching is performed instead of just fitting one analytical model to the data:

$$\begin{aligned} f(\rho(M_0),T_1,\kappa) = &\sum_i^{N_\alpha}\Big[\Big(\rho(M_0)\frac{1-E_1}{1-E_1\cos(\kappa\alpha_i)}\sin(\kappa\alpha_i)\Big) - S(\alpha_i)\Big]^2 \\ &+\sum_i^{N_{\mathcal{TI}}}\Big[\Big(\rho(M_0)(1-2e^{-\mathcal{TI}_i/T_1}+e^{-\mathcal{TR}/T_1})\sin(\kappa\alpha)\Big) - S_{\mathrm{IR}}(TI_i)\Big]^2 \ , \end{aligned} \tag{3.26}$$

with N_α and $N_{\mathcal{TI}}$ being the number of DESPOT1 and inversion recovery experiments, respectively.

In a typical protocol setup for measurements at a magnetic field strength of 3.0 T, one inversion recovery and two DESPOT1 data points are included [Deoni, 2007]. The error is specified to be 5 % at an overall measurement time of approximately 10 min. In this cited study, the inversion recovery experiment was performed with half of the resolution of the FLASH measurements and interpolated to the same matrix size; this is justified by the smoothness of the RF field distribution. At this point in time, the DESPOT1 with high-speed incorporation of RF field inhomogeneities (DESPOT1-HIFI) method has found its way into first clinical trials.

4 Results Part I: Introduction of Novel Methods

The following sections are the first part of the results comprising new methods to approach the challenges of volumetric quantitative imaging at ultra high field (UHF). A new simulation tool capable of numerically describing the magnetization and signal evolution through a magnetic resonance imaging (MRI) experiment is presented in section 4.1. Based on this tool, a novel approach for fast quantitative imaging of the longitudinal relaxation time is introduced in section 4.2. How these simulation-based methods perform in phantom and *in vivo* measurements is evaluated in the experimental results section 6.2.

4.1 Simulations of Spin Interactions

Within this thesis, a numerical solver for the magnetization's equation of motion and the Bloch equations was developed and implemented. To allow for a wide variety of applications, a new framework needed to be designed. This section will lead through the mathematical core of solving the Cartesian product of the macroscopic magnetization and the effective magnetic field from arbitrary input conditions in section 4.1.1. The impact of relaxation phenomena is shown in section 4.1.2 along with modulation, noise effects, and motion as outlined in section 4.1.3. An outlook is given of how problems such as multichannel transmission are addressed, as shown in section 4.1.4. Composite pulses as well as complete magnetic resonance sequences can be simulated as described in section 4.1.5. Section 4.1.6 closes these considerations with some brief remarks on high performance computing and a complexity estimation. In section 8 of the appendix, it is explained how the simulation tool is operated, which input variables are needed and how the output is controlled.

4.1.1 Rotation Matrix Approach

As described in section 2.1.3, the macroscopic magnetization is performing a precession motion defined by its state $\vec{M}$ and the effective magnetic field $\vec{B}_{\text{eff}}$. The effective magnetic field is composed of the static magnetic field $\vec{B}_0$ and the magnetic field component of the radio frequency (RF) pulse. While the amplitude B_0 is constant, the RF pulse is defined by its behavior of the amplitude B_1 and the frequency ω over time as well as by its initial phase ϕ (see section 2.2.1). For the time being, ϕ will not be set to zero as done in equation 2.40, so that the equation of motion comes out to:

$$\left.\frac{\partial \vec{M}}{\partial t}\right|_{\text{rot}} = \vec{M} \times \begin{pmatrix} B_1 \sin(\phi) \\ B_1 \cos(\phi) \\ \frac{\Delta\omega}{\gamma} \end{pmatrix} \quad ; \tag{4.1}$$

$\Delta\omega$ being the off-resonance to the Larmor frequency $\omega_{\mathcal{L}}$, and γ the gyromagnetic ratio. With a finite time step $\Delta\tau$, as it needs to be considered for implementation reasons, the discretized temporal derivative does not preserve the length of the magnetization vector. If the differential equation is solved, it unfolds to a rotation which is preserving the length of the rotated vector. The rotation approach bears a smaller error at larger time steps compared to the Cartesian product and thus, is more suitable as a numerical kernel.

From the effective magnetic field, a rotation matrix $\mathcal{R}$ can be designed so that a consecutive step $\vec{M}_{i+1}$ of $\vec{M}_i$ can be calculated by:

$$\vec{M}_{i+1} = \mathcal{R} \cdot \vec{M}_i \ . \tag{4.2}$$

The rotation matrix is defined by the tip angle α and the normalized rotation axis $\vec{n}$:

$$\mathcal{R} = \begin{pmatrix} n_x^2(1-c_\alpha)+c_\alpha & n_y n_x(1-c_\alpha)+n_z s_\alpha & n_z n_x(1-c_\alpha)-n_y s_\alpha \\ n_x n_y(1-c_\alpha)-n_z s_\alpha & n_y^2(1-c_\alpha)+c_\alpha & n_z n_y(1-c_\alpha)+n_x s_\alpha \\ n_x n_z(1-c_\alpha)+n_y s_\alpha & n_y n_z(1-c_\alpha)-n_x s_\alpha & n_z^2(1-c_\alpha)+c_\alpha \end{pmatrix} \ . \tag{4.3}$$

The trigonometric variables and the rotation axis are defined by:

$$c_\alpha = \cos(\alpha) \ , \ s_\alpha = \sin(\alpha) \ \text{ and } \ \vec{n} = \begin{pmatrix} n_x \\ n_y \\ n_z \end{pmatrix} \ , \tag{4.4}$$

while α and $\vec{n}$ themselves can be determined through:

$$\alpha = -\gamma |\vec{B}_{\text{eff}}| \Delta\tau \ \text{ and } \ \vec{n} = \frac{\vec{B}_{\text{eff}}}{|\vec{B}_{\text{eff}}|} \ . \tag{4.5}$$

This tip angle must not be mistaken as necessarily having the same effect as described in section 2.2.1. It is a rotation around the normalized rotation axis which points into the same direction as $\vec{B}_{\text{eff}}$.

Any RF pulse with varying amplitude and/or frequency and/or phase shifts must be subclassified into N rectangular pulses with constant amplitudes $B_{1,i}$, frequencies ω_i, phases ϕ_i, and durations $\Delta\tau_i$. Each of these subpulses gets its own rotation matrix $\mathcal{R}_i$ assigned and is computed consecutively with the innermost matrix operation on the initial magnetization $\vec{M}_0$ first:

$$\vec{M}_n = \prod_i^N \mathcal{R}_i \cdot \vec{M}_0 \ , \tag{4.6}$$

or as a more general expression:

$$\vec{M}_n = \prod_i^n \mathcal{C}_i(\vec{M}_0) = \mathcal{C}_n\Big(\mathcal{C}_{n-1}\Big(\dots \big(\mathcal{C}_1(\vec{M}_0)\big)\Big)\Big) \ \text{ with } \ \mathcal{C}_i(\vec{M}_{i-1}) = \mathcal{R}_i \cdot \vec{M}_{i-1} \ . \tag{4.7}$$

A stepwise approximation of the varying pulse forms causes simulation errors in each computation. The shorter the time step gets, the finer is the discretization and the higher the accuracy will be.

Two additional remarks must be made: on the one hand on the dimension of $\vec{M}$, and on the other hand on the composition of $\vec{B}_{\text{eff}}$.

The magnetization does not need to be a single vector, but it can span a vector field. Interpreting this field as a position space, it could be a point, line, plane, or volume of interest. In any of these cases, each entry at the position $\vec{r}$ relative to the magnetic isocenter holds the magnetization as a vector $\vec{M}(\vec{r})$ and must be computed independently from all neighbors with its own rotation matrix $\mathcal{R}(\vec{r})$. Equation 4.6 can be written as:

$$\vec{M}_n(\vec{r}) = \prod_i^N \mathcal{R}_i(\vec{r}) \cdot \vec{M}_0(\vec{r}) \ . \tag{4.8}$$

As before, the initial magnetization vectors $\vec{M}_0(\vec{r})$ can be of arbitrary values; either representing the equilibrium magnetization or a disturbed state.

Alternatively, the vector field can also be interpreted as a parameter space. In this case, each position holds information about the local conditions. Instead of referring to a magnetization by its position as in the equation above, it is addressed by its parameters $\vec{p}$:

$$\vec{M}_n(\vec{p}) = \prod_i^n \mathcal{R}_i(\vec{p}) \cdot \vec{M}_0(\vec{p}) \ . \tag{4.9}$$

For implementation reasons, $\vec{M}_0(\vec{p})$ is still limited to be a three-dimensional object at maximum. If the parameter space is of a higher order, it can be linearized because of the independence of its position and meet the input requirements.

The definition of the effective magnetic field is more complicated if additional conditions to the ideal case are regarded. Contributions to the z-component of $\vec{B}_{\text{eff}}$ might not only be due to off-resonance from the RF pulse, but also result from B_0 inhomogeneity ΔB_0, which is one of the entries of $\vec{p}$, scalar gradient fields G, and inner-voxel supersampling G_s:

$$B_{\text{eff},z}(\vec{r},\vec{p}) = \left(\frac{\Delta\omega}{\gamma} + \Delta B_0(\vec{r},\vec{p}) + G(\vec{r}) + G_s(\vec{r}_s)\right) \quad ; \tag{4.10}$$

while $\vec{r}$ still is the position relative to the magnetic isocenter and $\vec{r}_s$ the position within a voxel and relative to its center. ΔB_0 can be used to regard various combinations of a chemical shift between spin species, a change in susceptibility, or a variation of the static magnetic field. The scalar gradient field $G(\vec{r})$ is a distance map, in most cases linear. Directional information is regarded by the distance to the isoplane of the gradient. Both matrices ΔB_0 and G are of the same size as M_0. In the case of inner-voxel supersampling, each entry is subclassified into subentries, superimposed with an additional scalar gradient field $G_s(\vec{r}_s)$, computed independently, but passed back only as a complex sum. The supersampling is needed for accurate simulation of the apparent transverse relaxation process and is also called dephasing. In this case, all matrices have the size of the magnetization space times the supersampling factor in the respective direction. The z-component of the effective magnetic field is a pointwise addition of all contributions.

Furthermore, since the RF field also underlies spatial variations, see section 2.3.3, the amplitude can be altered and a phase offset can occur:

$$\begin{pmatrix} B_{\text{eff},x}(\vec{r},\vec{p}) \\ B_{\text{eff},y}(\vec{r},\vec{p}) \end{pmatrix} = \kappa(\vec{r},\vec{p}) \begin{pmatrix} B_1(\vec{r})\sin(\phi(\vec{r}) + \phi_{\text{off}}(\vec{r},\vec{p})) \\ B_1(\vec{r})\cos(\phi(\vec{r}) + \phi_{\text{off}}(\vec{r},\vec{p})) \end{pmatrix} \quad ; \tag{4.11}$$

κ is a point wise scaling factor, and ϕ_{off} is a point wise phase shift. Both are part of the parameter space $\vec{p}$, are matrices of the size of M_0, and come from a complex RF field map. This inhomogeneity is especially present if the RF pulse is transmitted by a number of sources as in the case of a birdcage coil. Interference effects (as discussed in section 2.3.3) cannot only cause phase shifts and amplitude modulations, but also off-resonant frequency contributions to the z-component of the effective magnetic field as mentioned above.

4.1.2 Transverse and Longitudinal Relaxation

From section 2.1.4 it is known how the transverse and the longitudinal relaxation influence the macroscopic magnetization and how the two can be handled via the Bloch equations. Transverse relaxation only affects the x- and y-components of $\vec{M}$. It is a time-dependent scaling by a time constant T_2 and can be implemented into a diagonal matrix $\mathcal{A}'$:

$$\mathcal{A}' = \begin{pmatrix} e^{-\Delta\tau_i/T_2} & 0 & 0 \\ 0 & e^{-\Delta\tau_i/T_2} & 0 \\ 0 & 0 & 0 \end{pmatrix} \quad . \tag{4.12}$$

With this matrix, a consecutive step of the relaxing magnetization can be computed by:

$$\vec{M}_{i+1} = \mathcal{A}^{'} \cdot \vec{M}_i \ . \tag{4.13}$$

Additionally, the longitudinal relaxation is building up the z-component of $\vec{M}$ by the time constant T_1 towards the equilibrium state. To implement this, $\mathcal{A}^{'}$ must be adapted to $\mathcal{A}$ and a second matrix $\mathcal{B}$ is needed so that:

$$\vec{M}_{i+1} = \mathcal{A} \cdot \vec{M}_i + \mathcal{B} \ , \tag{4.14}$$

with:

$$\mathcal{A} = \begin{pmatrix} e^{-\Delta\tau_i/T_2} & 0 & 0 \\ 0 & e^{-\Delta\tau_i/T_2} & 0 \\ 0 & 0 & e^{-\Delta\tau_i/T_1} \end{pmatrix} \text{ and } \mathcal{B} = \begin{pmatrix} 0 \\ 0 \\ 1 - e^{-\Delta\tau_i/T_1} \end{pmatrix} \ . \tag{4.15}$$

Both, T_2 and T_1 are part of the set of parameters $\vec{p}$ and of the same size as the matrices listed above. Alternatively, T_2 can be replaced by the apparent transverse relaxation time T_2^* to get a rough estimation without regarding the dephasing accurately.

In combination with a non-zero effective magnetic field, the resulting mathematical operation for a time step is:

$$\vec{M}_{i+1} = \mathcal{A} \cdot (\mathcal{R} \cdot \vec{M}_i) + \mathcal{B} \ , \tag{4.16}$$

or in the general expression:

$$\mathcal{C}_i(\vec{M}_{i-1}) = \mathcal{A} \cdot (\mathcal{R}_i \cdot \vec{M}_{i-1}) + \mathcal{B} \ , \tag{4.17}$$

This is the kernel of all numerical simulations within this framework. It is solely formulated in a rotation matrix style.

The major limitation of this solver is the fact that the rotation and relaxation matrices do not permute. For this approach, the rotation is performed first and thus, relaxation effects are not completely accurate. However, as long as the time steps are chosen small enough, these errors can be neglected.

4.1.3 Modulation, Noise Effects and Motion

The computational kernel will not be influenced by any of the described extensions from this section by any means. Pulse modulation is based on the fact, that the analytical functions that define the pulse forms of the amplitude and frequency as well as the initial phase are altered by either continuous or stepwise functions. The supporting points of the RF pulse can be altered completely isolated from each other:

$$B_{1,i}^{\text{mod}} = f_i^{\text{mod}} B_{1,i} \ , \tag{4.18}$$

$$\omega_i^{\text{mod}} = g_i^{\text{mod}} \omega_i \text{ and} \tag{4.19}$$

$$\phi^{\text{mod}} = \phi + \phi_{\text{off}}^{\text{mod}} \ , \tag{4.20}$$

as well as the supporting points of the gradients:

$$G_i{}^{\mathrm{mod}}(\vec{r}) = h_i^{\mathrm{mod}}(\vec{r})G_i(\vec{r}) \text{ and} \tag{4.21}$$

$$G_{s,i}^{\mathrm{mod}}(\vec{r}) = h_i^{\mathrm{mod}}(\vec{r}_s)G_{s,i}(\vec{r}_s) \ ; \tag{4.22}$$

f_i^{mod} and g_i^{mod} are modulation factors of the pulse amplitude and frequency, $\phi_{\mathrm{off}}^{\mathrm{mod}}$ a phase modulation offset, and $h_i^{\mathrm{mod}}(\vec{r})$ a manipulation of the directions and amplitudes of the gradients G and G_s, respectively. Typical examples for this modulation have already been given in section 2.2.1 in terms of a HAMMING or HANNING filtered cardinal sine (sinc) pulse. More advanced applications such as the SHINNAR-LE ROUX (SLR) technique or variable-rate selective excitation (VERSE) pulses are also dealt with in such a manner [Shinnar et al., 1989; Le Roux, 1986; Conolly et al., 1988]. The modulation is manipulating the RF pulse before it is handed to additional alterations or the mathematical kernel of the simulation tool.

The RF pulse and the gradient can also have noise contributions attached to them. It can either be in terms of a random jitter, a systematic drift, or a periodic pattern. All of those options influence how the pulse and gradient characteristics behave in time and influence the effective magnetic field for a certain time step. By processing such a distortion matrix before the computation kernel is executed, this can easily be regarded for. The mathematical implementation is similar to the one for pulse modulation (see above):

$$B_{1,i}^{\mathrm{noise}} = f_i^{\mathrm{noise}} B_{1,i} \text{ and} \tag{4.23}$$

$$\omega_i^{\mathrm{noise}} = g_i^{\mathrm{noise}} \omega_i \ , \tag{4.24}$$

as well as:

$$G_i{}^{\mathrm{noise}}(\vec{r}) = h_i^{\mathrm{noise}}(\vec{r})G_i(\vec{r}) \text{ and} \tag{4.25}$$

$$G_{s,i}^{\mathrm{noise}}(\vec{r}) = h_i^{\mathrm{noise}}(\vec{r}_s)G_{s,i}(\vec{r}_s) \ ; \tag{4.26}$$

again, f_i^{noise} and g_i^{noise} are noise factors of the pulse amplitude and frequency as well as $h_i^{\mathrm{noise}}(\vec{r})$ for the directions and amplitudes of the gradients G and G_s, respectively. Now, the gradient is not only noisy in time, but also potentially noisy in space. The so altered RF signal is passed to the kernel of the simulation tool.

Influences by a pulse modulation and the effects of noise can accumulate. As the modulation is usually performed within the RF synthesizer, and noise effects come into account in the line to the magnetic resonance (MR) tomograph and the coil itself, the modulation is performed first.

More complicated is the significance of movement, e. g. flow, of the magnetization space throughout the simulation. A displacement of a magnetization vector to $\vec{r}\,'$ by $\Delta\vec{r}$:

$$\vec{r}\,' = \vec{r} + \Delta\vec{r} \ , \tag{4.27}$$

causes a change in the local conditions listed above. The most obvious alteration will appear in the local gradient fields $G(\vec{r})$ and $G_s(\vec{r}_s)$ as $\vec{r}$ and $\vec{r}_s$ change. The same accounts for the amplitude and frequency of the RF pulse. Going one step further, a subvoxel shift

or a discrepancy from the continuity equation will cause a new composition of spin entities within one voxel and thus new effective values for all parameters.

For this tool, a different approach is pursued. Instead of shifting the magnetization, the local conditions are shifted in space. This way, all spin entities are preserved in time and can be used to assemble the final state. All spins must be part of the initial magnetization space; the effect of $\vec{B}_{\text{eff}}$ is only calculated within the field of view (FOV). A displacement can be of a continuous or non-continuous nature as for example a periodic motion. The transition vector $\Delta\vec{r}_i$ is defined for each time step:

$$\vec{r}_i{}' = \vec{r}_i + \Delta\vec{r}_i \ . \tag{4.28}$$

It shifts the effective magnetic field and hence the rotation matrix to $\mathcal{R}_i(\vec{r}_i{}')$ before the kernel is executed. Subvoxel shifts are dealt with by interpolating the local conditions; this holds a much smaller computational burden than for the first approach listed above as less rotation operations are performed.

4.1.4 Single- and Multi-Channel Transmission

Multi-channel transmission, simultaneous or consecutive, can also be addressed within this framework. Instead of having only one transmission element, a coil can have a number of such. Each transmission element has its own FOV with a certain phase correlation to the others. The correlation can be static, e. g. for constant frequencies, or dynamic.

To regard these non-general conditions, the effective magnetic field $\vec{B}_{\text{eff}}$ must be manipulated. As described in section 4.1.1 above, it can be calculated for each transmission element independently from the others. In the most simple case, the phase correlation is static. Now the total $\vec{B}_{\text{eff}}$ is the sum of all contributing transmission elements:

$$\vec{B}_{\text{eff}} = \sum_{i}^{N_{\text{FOV}}} \vec{B}_{\text{eff},i} \ ; \tag{4.29}$$

with N_{FOV} being the number of contributing transmission elements. However, if the phase correlation changes with more complex dependencies, the complex RF field maps must hold for these conditions and are usually loaded from a predefined field map library.

4.1.5 Composite Pulses and Pulse Sequences

To simulate sequential arrangement of pulses, e. g. an excitation followed by relaxation, the program can be called several times. The first call may compute the equilibrium magnetization as the initial state and stores the result to the hard drive. The second call loads this result and uses it as the new initial state, the equilibrium magnetization is still the same though. An alternative approach would be, to define the succession of the two simulations as one external pulse. In either case, composite pulses or complete pulse sequences can be simulated. A virtual k-space can be simulated as described above. Instead of filtering the k-space of an object, this tool offers some insights on how the magnetization behaves in position space through an MRI experiment.

4.1.6 High Performance Computing, and Complexity Estimation

Functions of high computational burden have been written and compiled as MEX-files (C/C++ standard) and have been implement into the MATLAB code. This is the case for the definition of the gradient field and the dephasing field, as well as for the mathematical kernel. In the case of the gradient fields, the speedup factor was measured as a factor of 10–20 in comparison to MATLAB code. For the mathematical kernel, it is of a factor of 100 and above.

The acceleration mentioned above is the reason why the code is parallelized on the scale of larger subtasks only. Parallelization within the simulation, e. g. for the magnetization space, is not profitable as the overhead is too large compared to the computational burden of a single point kernel execution. The framework can be executed on a local client or the high performance computing (HPC) cluster described in section 3.1.3. The acceleration does not scale linearly with the number of working nodes. Deviations from the linear relationship are hard to quantify but the performance is more than 90 % of the expected.

In general, the computation time of the initialization and preparation section goes linear with the number of time steps and gradient orientations. The dependencies within the run section are more complex. Depending on the impact of the simplification, the computational time might not be influenced at all or by a factor of 1000 and more. It is important how unique the magnetization space and all physical parameters can be expressed. The time needed for the calculation of each rotation matrix goes nearly linear with the number of matrix entries and hence, with the simplification as well. The computation time of the mathematical kernel is composed of a static overhead to call the MEX-file, and the time for the calculation itself. In most cases, the relation of the computation time to the number of matrix entries is sublinear. The three data storages to the hard drive can take a significant amount of time that might outweigh the computation time itself.

4.2 Volumetric T_1 Quantification

4.2.1 Remarks on Three-Point DESPOT1

The three-point driven-equilibrium single-pulse observation of T_1 relaxation (DESPOT1) method was investigated regarding its performance at a static magnetic field strength of 7 T. None of the experiments within this thesis was capable of reproducing the published results [Li and Deoni, 2006]. For this reason, a thorough analysis of the theory was undertaken.

As introduced in all three DESPOT1 approaches, see sections 3.4.2, 3.4.3, and 3.4.4, the *fast low angle shot* (FLASH) technique holds as a basis. Its signal equation 2.66 with signal S is:

$$S = \rho(M_0)\frac{1 - e^{-tr/T_1}}{1 - e^{-tr/T_1}\cos(\alpha)}e^{-te/T_2^*}\sin(\alpha) \ , \tag{4.30}$$

with $\rho(M_0)$ being a factor proportional to the signal in the equilibrium state, T_1 and T_2^* the longitudinal and apparent transverse relaxation times, te and tr the echo and the repetition

time, and α the tip angle. It can be rewritten and simplified to:

$$S = \rho(M_0)\frac{1 - E_1}{1 - E_1\cos(\alpha)}\sin(\alpha) \tag{4.31}$$

with

$$E_1 = e^{-tr/T_1} \text{ and } e^{-te/T_2^*} \to 1 \text{ for } te \to 0 \ . \tag{4.32}$$

The proposed ratios a_1 and a_2 of signals at three different tip angles α, 2α, and 4α are defined by the expressions:

$$a_1 = \frac{S(\alpha)}{S(2\alpha)} = \frac{\sin(\alpha)\Big(1 - E_1\cos(2\alpha)\Big)}{\Big(1 - E_1\cos(\alpha)\Big)\sin(2\alpha)} \text{ and} \tag{4.33}$$

$$a_2 = \frac{S(2\alpha)}{S(4\alpha)} = \frac{\sin(2\alpha)\Big(1 - E_1\cos(4\alpha)\Big)}{\Big(1 - E_1\cos(2\alpha)\Big)\sin(4\alpha)} \ . \tag{4.34}$$

With the final substitution of:

$$\sin(2\alpha) = 2\sin(\alpha)\cos(\alpha) \text{ and } \cos(2\alpha) = 2\cos(\alpha)^2 - 1 \ , \tag{4.35}$$

the expressions can be rewritten to:

$$a_1 = \frac{1 - E_1\Big(2\cos(\alpha)^2 - 1\Big)}{2\Big(1 - E_1\cos(\alpha)\Big)\cos(\alpha)} \text{ and} \tag{4.36}$$

$$a_2 = \frac{1 - E_1\Big(2\cos(2\alpha)^2 - 1\Big)}{2\Big(1 - E_1\cos(2\alpha)\Big)\cos(2\alpha)} \ . \tag{4.37}$$

So far the theory is correct [Li and Deoni, 2006]. Taking a different way of substituting the cosine terms by:

$$x_1 = \cos(\alpha) \text{ and } x_2 = \cos(2\alpha) \ , \tag{4.38}$$

the ratios a_1 and a_2 can be solved for E_1, respectively:

$$E_1 = \frac{2a_1(x_1) - 1}{(2a_1 - 2)(x_1^2) + 1} \text{ and} \tag{4.39}$$

$$E_1 = \frac{2a_2(x_2) - 1}{(2a_2 - 2)(x_2^2) + 1} \ . \tag{4.40}$$

A polynomial expression can be set up and comes out to

$$\begin{aligned}&(4a_1a_2 - 4a_1)(x_1x_2^2) + 2a_1(x_1) - (2a_2 - 2)(x_2^2) - 1\\ =&(4a_1a_2 - 4a_2)(x_1^2x_2) + 2a_2(x_2) - (2a_1 - 2)(x_1^2) - 1 \ .\end{aligned} \tag{4.41}$$

Finally, with the simplification below, the expression can be expanded to:

$$\begin{aligned}(8a_1a_2 - 8a_1)x^5 - (4a_1a_2 - 4)x^4 - (8a_1a_2 - 8a_1)x^3 + \\ (2a_1a_2 + a_1 - 5)x^2 + (2a_1a_2 - a_1)x + 1 = 0\end{aligned} \tag{4.42}$$

with

$$x = x_1 = 2x_2^2 - 1 \ . \tag{4.43}$$

This expression differs from the published polynomial presented in equation 3.22. Detailed studies upon this new theory are not presented within this thesis. It is noteworthy though, that in the ideal case the determination of the longitudinal relaxation times is technically feasible. However, the evaluation of simulation and measurement data showed, that the new theory is not stable enough to be applied in routine *in vivo* examinations. The impact of noise, even at small, non-realistic levels, disturbs the calculation of E_1. Deviations from the expected value are not just of a systematic nature, but rather fail totally. The three-point DESPOT1 method has not been investigated any further.

4.2.2 Remarks on DESPOT1-HIFI

The second approach of DESPOT1 with high-speed incorporation of RF field inhomogeneities (DESPOT1-HIFI) for the quantification of the longitudinal relaxation time has also been tested to hold at a magnetic field strength of 7 T. Initial results of such an evaluation are presented in section 6.2.2 and show systematic errors. To understand the origin of these errors, a more detailed analysis of the theory is given below.

From the sections 2.1.4 about relaxation and 3.4.1 about the inversion recovery (IR) experiment it is known, how the longitudinal component of the magnetization $M_{z,i}$ recovers in time:

$$M_{z,i} = M'''_{z,i-1} e^{-TI/T_1} + M_0(1 - e^{-TI/T_1}) \ , \tag{4.44}$$

with $M'''_{z,i-1}$ being the available magnetization before the inversion, M_0 the equilibrium magnetization, T_1 the longitudinal relaxation time, and TI the inversion time. At the inversion time, a readout pulse with the tip angle α excites the magnetization and reduces its z-component to $M'_{z,i}$:

$$M'_{z,i} = M_{z,i} \cos(\alpha) \ . \tag{4.45}$$

From here, the magnetization recovers again analogous to the first step. However, the time frame is not defined by the inversion time, but by the remaining time until the next inversion is performed. The repetition time of the preparation TR yields a longitudinal magnetization $M''_{z,i}$ of:

$$M''_{zi} = M'_{z,i} e^{-(TR-TI)/T_1} + M_0(1 - e^{-(TR-TI)/T_1}) \ . \tag{4.46}$$

And finally this magnetization is inverted by the tip angle β to the initial state $M'''_{z,i}$ of the next preparation block.

$$M'''_{z,i} = M''_{z,i} \cos(\beta) \ . \tag{4.47}$$

By taking a look at the following step $M_{z,i+1}$, which is defined by:

$$M_{z,i+1} = M_{z,i}^{'''} e^{-TI/T_1} + M_0(1 - e^{-TI/T_1}) \ , \tag{4.48}$$

the equation from above can be followed backwards in time. The aim of this is to become free of the iterative dependence. A perfect inversion with 180 ° for β yields:

$$M_{z,i+1} = -M_{z,i}^{''} e^{-TI/T_1} + M_0(1 - e^{-TI/T_1}) \ . \tag{4.49}$$

$M_{z,i}^{''}$ still depends on $M_{z,i}^{'}$ which indirectly depends on $M_{z,i-1}^{'''}$. Setting the readout tip angle α to 90 ° cancels this dependency. The final equation can be written as:

$$M_{z,i+1} = -M_0(1 - e^{-(TR-TI)/T_1})e^{-TI/T_1} + M_0(1 - e^{-TI/T_1}) \ , \tag{4.50}$$

and simplified to:

$$M_{z,i+1} = M_0(1 - 2e^{-TI/T_1} + e^{-TR/T_1}) \ . \tag{4.51}$$

Concluding, the signal equation from the publication [Deoni, 2007]:

$$S_{\mathrm{IR}}(TI) = \rho(M_0)(1 - 2e^{-TI/T_1} + e^{-TR/T_1}) \sin(\kappa\alpha) \ , \tag{4.52}$$

is only true for readout tip angles of 90 °.

This is typically not the case for a FLASH readout. Multi-line readout trains with individual excitations do not hold the desired information; prior excitations have a spoiling effect. In general, spin-echo sequences would fulfill this criterion, but would take a long time and the issue of a heterogeneous RF field distribution at ultra high magnetic fields strength is an additional restraint. Within the next sections, a new approach is presented to overcome these limitations: a fast and accurate method for T_1 quantification by single-shot IR gradient-recalled echo (GRE) sequences.

4.2.3 Insights into the Inversion Recovery Experiment

Instead of trying to describe the behavior of the macroscopic magnetization by analytical expressions, it can also be calculated by an iterative numerical approach. The newly developed simulation tool, presented in section 4.1, is capable of performing such calculations. Each time step, no matter whether it corresponds to an RF and/or a gradient object or a free relaxation period is computed consecutively.

Once again, an idealized IR experiment is outlined. The magnetization $\vec{M}$ is in the equilibrium state at the starting point. A 180 ° RF pulse inverts $\vec{M}$ and any possibly remaining transverse magnetization is dephased by spoiling gradients. During the inversion time TI, it recovers to a certain degree; depending on the longitudinal relaxation time T_1. Up to this point, the evolution can be described by the theory outlined above. From here on, three different manipulations of the magnetization must be differentiated. The most simple one is a readout with an infinitesimal tip angle α. The longitudinal recovery is not distorted and the relaxation continues as before. A second option is given by a 90 ° readout (see above). All of the longitudinal magnetization is tipped to the transverse plane. From

this point on, the relaxation can be expressed as a saturation recovery (SR) evolution. Yet in reality, none of the two readout techniques is practicable in general. The tip angle, whether nominal or altered by the RF field inhomogeneity, is of a deliberate value.

If the repetition time of the preparation *TR* is long enough compared to T_1 and α, then the considerations from above are not of any concern. The only difference would be visible in the signal amplitude and thus, the signal to noise ratio (SNR). In this case however, the total acquisition time would exceed any reasonable time frame. Depending on the ratio of *TR* to the available delay time *TD* after the readout, the longitudinal magnetization available for the following preparation is reduced (comparable to figures 4.1(a,b) and explained below). As a consequence, the magnetization cannot be described by the common theory any longer.

Furthermore, for a multi-line FLASH readout the situation is even more complicated. A readout train does not just disturb the longitudinal magnetization once, but many times. No matter what the starting point of the readout is, it will always drive the magnetization into the FLASH steady-state; this is indicated in figures 4.1(a,b). How fast this steady-state is reached, i. e. the number of readout pulses, depends on multiple parameters: the initial state of $\vec{M}$ defined by the *TI* (see figure 4.1(a)), as well as α and the repetition time of the readout *tr* (see figure 4.1(b)).

If the readout train would be long enough and the FLASH steady-state always reached, then the FLASH signal equation could be used to calculate the initial state of the magnetization prior to the preparation. However, this cannot be ensured; tissues with long T_1 values do not fulfill this criterion, e. g. gray and white brain matter. Independent of this steady-state though, another steady-state caused by the preparation will form as shown in figure 4.1(c). It must be pointed out, that this preparation steady-state is different than the one for the original IR experiment, i. e. the equilibrium state, as well as for the 90 ° readout IR experiment with a reduced *TR* (see equation 4.52). Eventually, such a simulation can be performed for any magnetization of the respective physical parameters and any MRI sequence.

4.2.4 Predicting the MR Signal

Knowing how the magnetization actually evolves throughout an MRI experiment allows for the use of this knowledge in more sophisticated evaluation techniques. In section 3.4 about quantitative imaging techniques, it has been outlined how each of these approaches relies on the regression of an analytical model to the signal values. If the evolution of the signal values is disturbed, the model will no longer fit. In this thesis it has been proposed, that the deviations of the signal values can be corrected for based upon simulations. This and the following sections introduce a number of strategies how this can be achieved.

At first, the signal must be obtained by the simulation. To do so, the sequences must be parameterized and broken down into two nested loops. The outer loop handles the preparation with the four steps of the inversion, recovery time, readout, and repetition time of the preparation. The inner loop is located within the readout and encompasses the excitation, echo time, data sampling, and the readout repetition time. Relaxation effects throughout each object are additionally regarded for. Eventually, the signal is

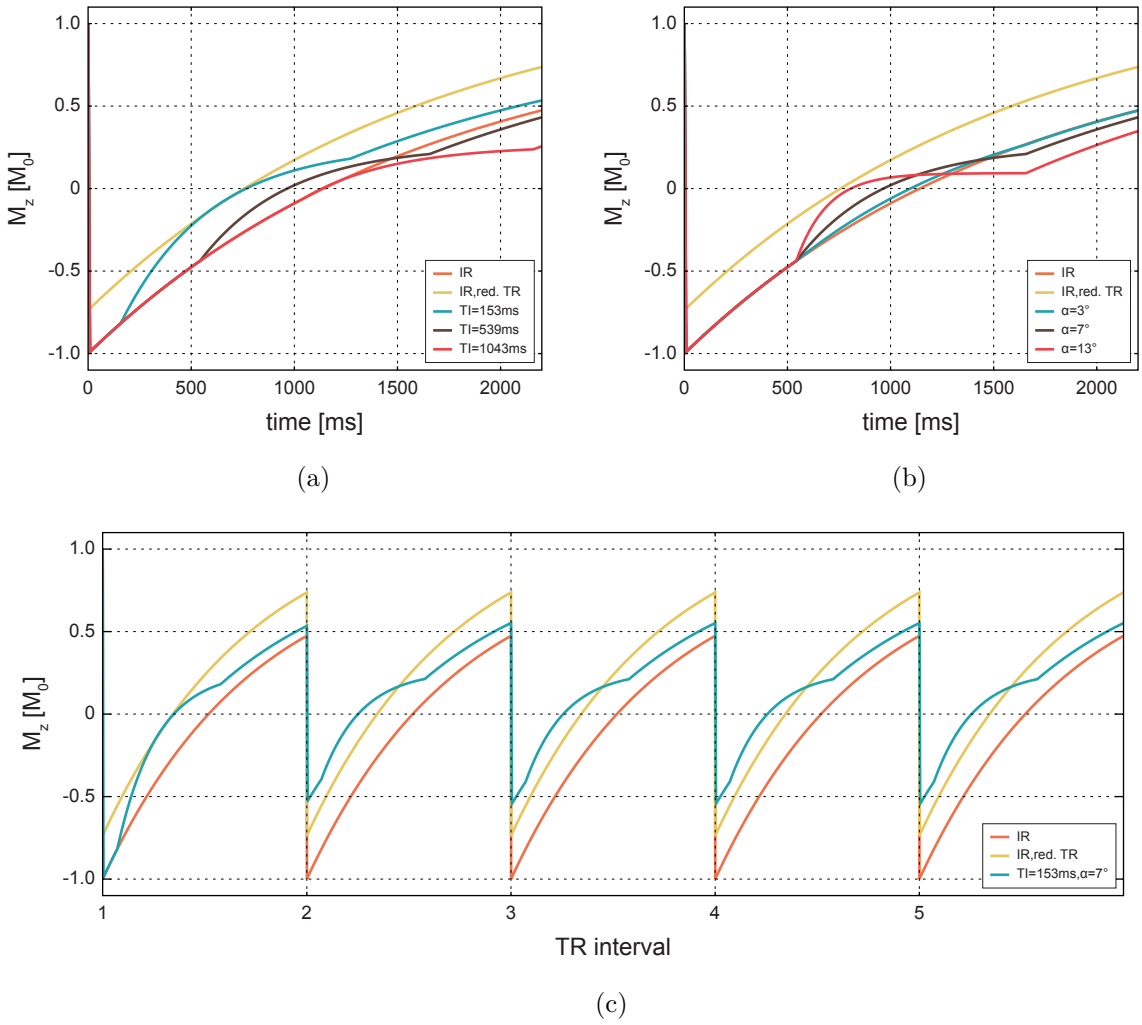

Figure 4.1: Insights into the IR experiment: All sequence parameters accord to the experiments described in section 5.2.1. The orange and yellow curves describe the original IR evolution and the one for a 90 ° readout with a reduced repetition time of the preparation *TR*. (a) The recovery process of the longitudinal magnetization M_z is shown for the original IR experiment (orange curve) and for the one with a 90 ° readout and a reduced repetition time of the preparation (yellow curve). A readout of a multi-line FLASH sequence distorts the imprinted contrast at different inversion times *TI* (blue: 153 ms, brown: 539 ms, red: 1043 ms). (b) The distortion itself depends on the tip angle α of the excitation pulse besides other (blue: 3 °, brown: 7 °, red: 13 °). (c) A steady-state of the preparation with a constant magnetization available prior to the inversion is reached after just a few *TR* intervals. In every *TR* interval, the recovery process of the original IR is assumed to start from an inverted equilibrium magnetization M_0.

given by the transverse magnetization at a time point defined to the virtual analog digital converter (ADC) event (see section 4.1.5. As already outlined above, this signal value is specific not only for the sequence parameters but also for the physical properties and the static magnetic and RF field. Because the deviation of the signal from theory is mainly caused by the offset of the initial magnetization, it will be referred to as the `offset` signal in the following.

4.2.5 Regarding the *k*-Space Filter Effects

Furthermore, it is shown in section 2.2.2 about k-space, that the major portion of the image energy is located at low frequencies near the k-space center. The assumption to condense it into a single point, as it is done for the signal simulation above, is not accurate.

The readout of magnetization that is not in a steady-state is influenced by two phenomena. One is the blurring due to the point spread function (PSF). The other is the composition of the signal of differently contrasted k-space lines. A closer look at figure 4.2(a) shows, how the resulting signal is changes in time. Again, for an IR experiments with sufficiently long repetition times of the preparation, this can simply be regarded for by an effective inversion time. However, if the repetition time is shortened, the signal must be simulated.

To accomplish this, a simulation of a complete imaging experiment must be performed as before (see section 4.2.4). However, instead of calculating only one signal value, a weighting matrix in k-space must be regarded. This weighting matrix is composed of the signal evolution throughout the MRI experiment similar to the concept of excitation k-space. To calculate the filter effect, a reference object is required. For this reason, a cubic structure is created within the image space. It is FOURIER transformed and pointwise multiplied with the weighting matrix. Its inverse FOURIER transform reveals the weighted structure in image space again. Intensity variations from blurring and ringing near the edges of the cube are not given any respect to at this point. The simulated signal is calculated from the average within the cube, and it is different from the `offset` signal. In the following, it will be referred to as the `filter` signal.

The basis of the signal deviation is given by the so called k-space filter. Three different k-space filters must be differentiated.

- read: Once excited, the signal decays by its apparent transverse relaxation. The k-space is weighted by an exponential function as shown in figures 4.2(b) and 4.3(b).
- phase: This filter especially appears for magnetization prepared sequences as described above. Its shape cannot be generalized but rather depends on its initial state and the readout train. In figures 4.2(a,c) it is demonstrated how the signal is driven into the FLASH steady state. The filter has the shape of a curved wedge (shown in figures 4.3(a,d)).
- partition: Most filters in partition direction are of a minor importance. It is nearly not recognizable in figure 4.3(c). For IR sequences it appears as transient oscillation before the preparation steady-state is reached.

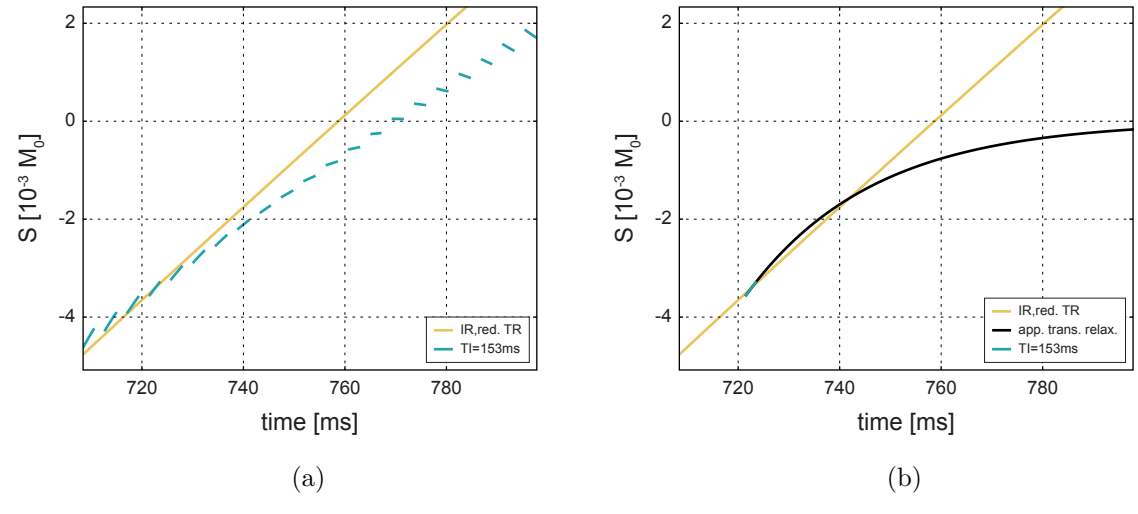

(a)

(b)

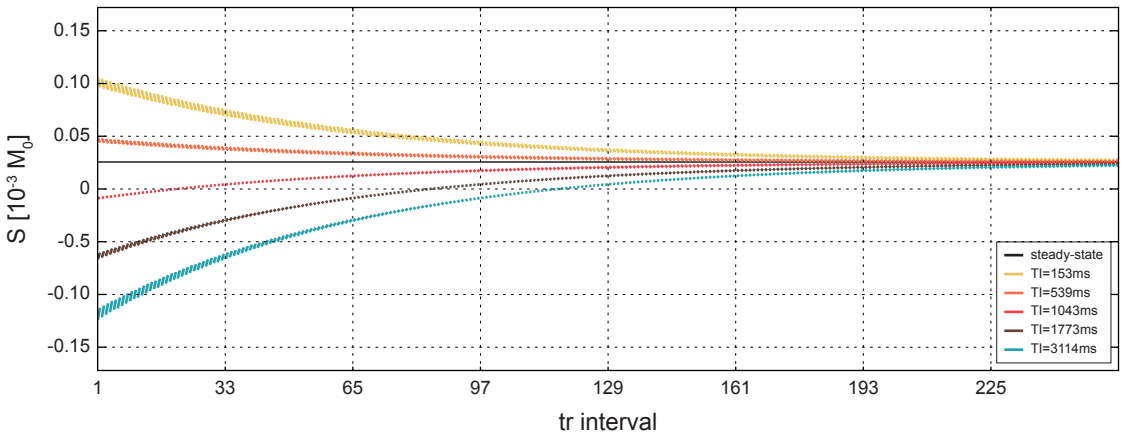

(c)

Figure 4.2: Simulation of the IR signal: All sequence parameters accord to the experiments in section 5.2.1. (a) A simulated (blue curve) signal S at an inversion time TI of 153 ms deviates from the theory of the IR experiment with a 90 ° readout (yellow curve). The curvature of the line segments is due to the exponential decay of the signal by the apparent transverse relaxation. It is noteworthy, that the signal always strives for a zero value. (b) The line segment is just a very short time frame off the theoretical relaxation process (black curve). (c) Despite the state of the magnetization before the start of the readout, the signal will always converge to the FLASH steady-state (black line). This is again demonstrated for different inversion times (blue: 153 ms, brown: 539 ms, red: 1043 ms, orange: 1773 ms, yellow: 3114 ms).

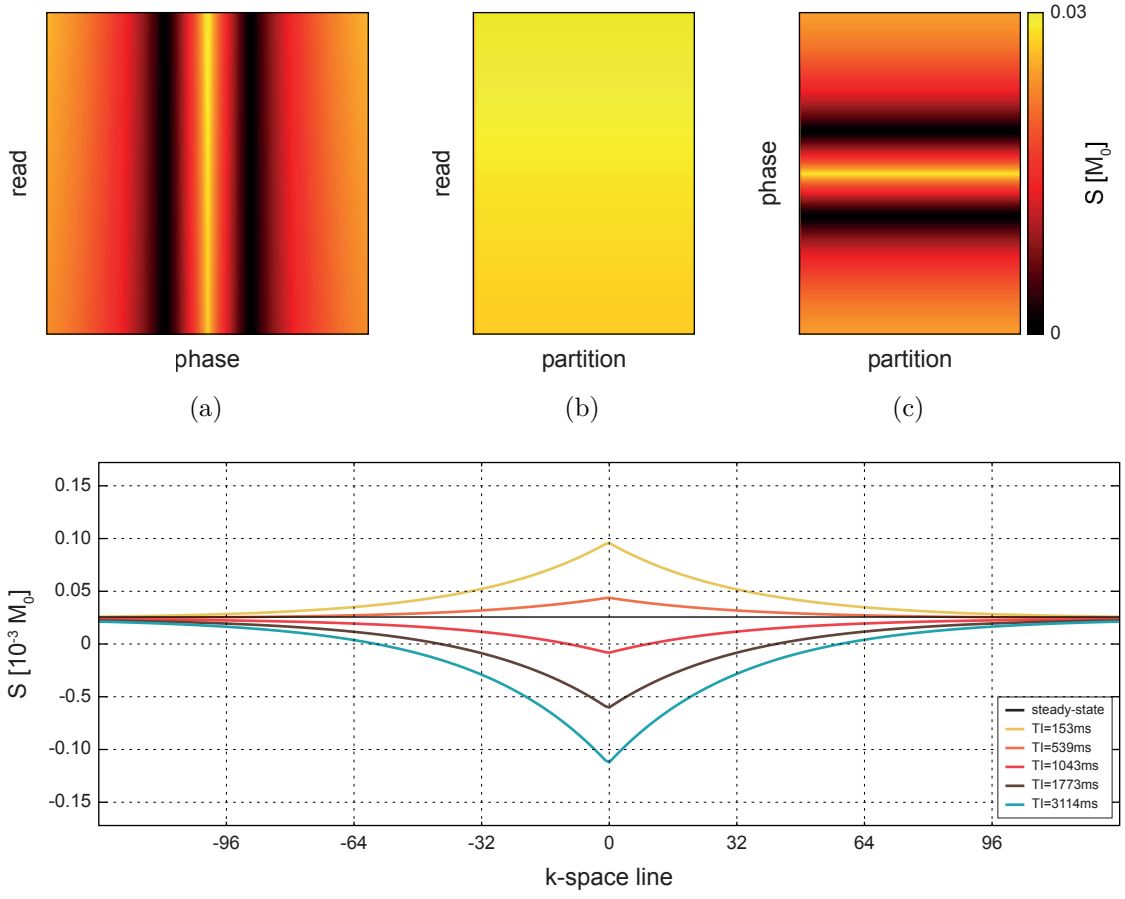

Figure 4.3: k-Space filter: All sequence parameters accord to the experiments in section 5.2.1. The readout of an MRI sequence distorts the imprinted contrast in all k-space directions. (a) This is especially significant in phase direction. Depending on the initially imprinted contrast, the readout drives the magnetization into the FLASH steady state. The signal S is zero when the magnetization passes the transverse plane. (b) In read direction, the sample points are weighted by the exponential decay of the signal due to the apparent transverse relaxation. (c) A partition filter only occurs for magnetization prepared experiments. It is hardly visible in the diagram above but causes some light ghosting artifacts. (d) It is shown how the initial state of the magnetization, defined by the inversion time TI, influences the filter shape; it appears as a curved wedge (a folded wedge when the absolute values are considered).

4.2.6 Signal Correction Techniques

The simulation, regardless whether of the `offset` or the `filter` signal, can be used to correct the signal deviations between theory and measurement. Three different approaches are represented within this section: signal scaling, virtual initial magnetization estimation, and simulation matching. A comparison between theoretical and simulated data points is exemplified in figure 4.4(a).

The signal evolution from the simulation S_{sim} is set into relation with the theoretical values S_{theo}. From the ratio of the two, a scaling factor can be derived. It is a constant for a fixed set of sequence parameters, especially the corresponding inversion time, and the targeted relaxation times. Mathematically it does not make a difference whether to calculate the scaling parameter ξ by:

$$\xi = \frac{S_{\text{theo}}}{S_{\text{sim}}} \text{ or } \xi = \frac{S_{\text{sim}}}{S_{\text{theo}}} \ , \tag{4.53}$$

but for practical considerations regarding the numerical stability, it must be pointed out here. The proper values for the respective regression functions are calculated by:

$$f_{\text{fit}} = \frac{f_{\text{theo}}}{\xi} \text{ or } f_{\text{fit}} = \xi f_{\text{theo}} \ , \tag{4.54}$$

with f_{fit} and f_{theo} being the actual and theoretical function values, respectively.

This method shall be called signal scaling. It does not make a difference whether the theory of the standard IR (referred to as `scaled IR`) experiment or the one with the 90 ° tip angle and reduced repetition time of the preparation TR (referred to as `scaled IRTR`) is used; as long as the scaling parameter ξ is calculated accordingly.

An alternative approach is given by use of the knowledge about the magnetization available prior to the preparation. Equation 3.10 for the signal $S_{\text{IR}}(TI)$ from above only accounts for a perfect inversion:

$$S_{\text{IR}}(TI) = \rho(M_0)(1 - 2e^{-TI/T_1} + e^{-TR/T_1}) \sin(\alpha) \ ; \tag{4.55}$$

with $\rho(M_0)$ being proportional to the signal of the equilibrium magnetization, T_1 the longitudinal relaxation time, and TI and TR the inversion time and repetition time of the preparation, respectively. If the inversion is non-perfect or less magnetization is available before the inversion pulse, it can be regarded for by:

$$S_{\text{IR}}(TI) = \rho(M_0) \left(1 - \left(1 - \frac{\rho(M_z^{'})}{\rho(M_0)}\right) e^{-TI/T_1}\right) \sin(\kappa\alpha) \ ; \tag{4.56}$$

with $\rho(M_z^{'})$ being proportional to the longitudinal magnetization available at the beginning of the preparation and κ a scaling factor of the tip angle. This ratio of $\rho(M_z^{'})$ and $\rho(M_0)$ can be extracted from the simulation in the following manner:

$$\frac{\rho(M_z^{'})}{\rho(M_0)} = 1 - \left(1 - \frac{S_{\text{sim}}}{S_{\text{sim},0}}\right) \frac{1}{e^{-TI/T_1}} \ , \tag{4.57}$$

with $S_{\text{sim},0}$ being the simulation signal of the equilibrium magnetization. As the signal scaling factor introduced above, this constant does only account for a specific set of sequence parameters, especially concerning the inversion time.

This method will be called virtual initial magnetization estimation from here on. The notation "virtual" refers to the fact that it is not about a real magnetization, but rather about an apparent one. With the calculation of the `offset` signal from section 4.2.4, the virtual and real magnetization come up to the same. If the k-space filter effect is regarded, the actual signal value is shifted compared to the signal value of the k-space center line. It can be looked at in the following way: each sample point of the IR curve gets its own initial magnetization assigned and thus, its own IR curve; this is shown in figure 4.4(b). For the experiment, the totality of all recovery evolutions is only valid in the according TI time points. This instance becomes obvious when the transgression of the absolute value of $\rho(M_z')$ over $\rho(M_0)$ is considered. It is very contra intuitive but absolutely mandatory to fulfill the signal equation at the time point TI.

A third technique to correct the readout effects is by matching the simulated signal to the measurement data directly. It is simple and straight forward. The only difference between a measurement and the according simulation, with respect to all required parameters, lies in the signal amplitude. With a free scaling parameter λ, the entries of the lookup table can be matched:

$$S_{\text{theo}} = \lambda S_{\text{sim}} \ . \tag{4.58}$$

It is also specific for a defined set of physical parameters.

This approach will be called simulation matching and will be referred to as `matched` in the following. The scaling parameter holds information similar to $\rho(M_0)$ and thus, to the signal amplitude.

4.2.7 Simulation-Based Inversion Recovery

This section describes a new T_1 quantification technique by an extension to the IR experiment. It is the one of the two main outcomes of this thesis. The knowledge of the behavior of different types of tissue, characterized by the physical parameters, is used to correct systematic errors in quantitative imaging. A new method called simulation-based IR (SIMBA IR) is introduced at this point. The complete setup of a SIMBA IR experiment is classified into three steps and will be outlined in the following: a one-time creation of a lookup table library, the actual magnetic resonance imaging measurements, and the evaluation.

At first, the parameters for the MRI sequences must be defined. The full potential of this method unfolds for 3D imaging at high resolution. Benefits of a higher signal from static magnetic field strengths greater than 3 T help with SNR limitations. The spoiled GRE sequence is defined by:

- matrix size: in read, phase, and partition direction,
- excitation pulse object: tip angle and duration, and
- timings: echo, repetition, and ADC dwell time.

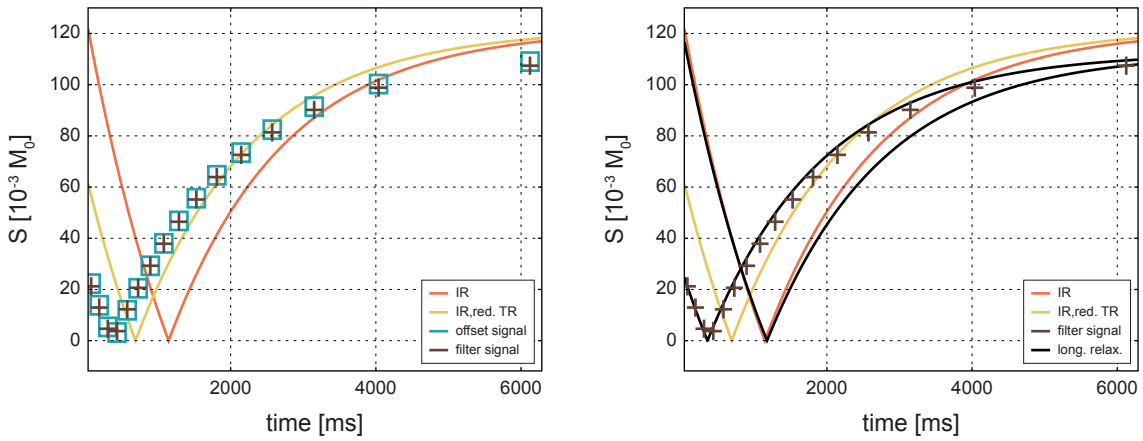

(a) (b)

Figure 4.4: Simulation-based signal correction techniques: All sequence parameters accord to the experiments in section 5.2.1. (a) The longitudinal recovery process is shown for the original IR experiment in orange and for the approach of a 90 ° readout in yellow. Blue squares and brown crosses indicates the amplitude of the simulations of the `offset` and `filter` signal S, respectively. A strong deviation from theory can be depicted at short inversion times TI. (b) When the virtual initial magnetization correction is applied, each TI data points is getting its own recovery curve assigned. The two exemplary black curves are only valid at the corresponding inversion times 42 ms and 6087 ms. Although it is contra intuitive, the absolute value of virtual magnetization can exceed the one of the equilibrium state.

Additional parameters for the spoiled IR GRE sequence are:

- preparation pulse object: tip angle and duration and
- timings: inversion and repetition time of the preparation.

These parameters may not be changed for the actual measurements without adapting the simulation as well. The timings should be depicted in such a way, that the total acquisition time of the experiment is within a reasonable time frame.

Lookup tables are calculated from here based on the `offset` signal (see section 4.2.4) and the `filter` signal (see section 4.2.5) as well as for all correction approaches introduced above (see section 4.2.6). Magnetic properties of the simulated tissue types collapse to the longitudinal relaxation time and the local tip angle scaling only. The transverse relaxation does not play a role in spoiled GRE sequences, and the apparent transverse relaxation time usually varies so little, that it can be approximated by an average value of the region of interest. Concerning the local magnetic field conditions, the variations only have a small influence on the effect of the applied RF pulses and nearly none on the readout itself. The result of this step is a set of lookup tables for the correction of the signal within the SIMBA IR method.

The second step is rather simple. From the set of predefined IR GRE sequence protocols, a number is depicted and applied in a measurement. However, some regards must be made. On one side, the constraints of specific absorption rate (SAR) and peripheral nerve stimulation (PNS) must be maintained. On the other hand, the total acquisition time must

be held short enough to neglect patient movement. Otherwise, registration techniques must be applied before the evaluation can be processed.

In the third step, the image data is evaluated to obtain the quantified parameter maps. Depending on the signal simulation procedure and the correction methods, the corresponding lookup table is selected. Within each iteration of the optimization, the entries are extracted from the lookup tables according to the trial parameters. The target function is minimized when the best fit of the lookup table is identified thus, holding the quantitative results.

The evaluation itself is performed via a constrained non-linear sequential quadratic programming method. Finite differences are used to approximate the derivatives. No-grid criteria such as a maximum number of iterations as well as tolerances for the parameters and the function values are also specified. The optimization can be started on a single-starting point of parameters (referred to as `single-start` in the following), or from a number of such (also referred to as `multi-start`). By using the latter approach, the risk of drifting into a local minimum of the target function can be degraded. A check of whether or not the optimization drives the parameter into the same optimum and on the gradient of the parameter space gives a visualization of the reliability of the result. Of course this comes with a significant cost of computational burden.

4.2.8 Simulation-Based DESPOT1-HIFI

The second main outcome and a fast quantification technique introduced in this thesis is the simulation-based DESPOT1-HIFI (SIMBA DESPOT1-HIFI) method. A transition from a SIMBA IR experiment to a SIMBA DESPOT1-HIFI approach is simple. Analogous to the simulation process and correction techniques of the IR sequence, a FLASH sequence at different tip angles can be computed. The measurement step is extended by the execution of predefined GRE sequences. Finally, the evaluation is analogous to the originally proposed method and only aided by the correction presented within this section.

The evaluation software is implemented as specified above. All optimization parameters listed in the same section also account for the simulation-based DESPOT1-HIFI.

5 Parameters and Setups of Simulations and Experiments

This chapter presents the experimental magnetic resonance (MR) measurement setups necessary for the evaluation of the robustness and performance of the novel simulation-based quantitative imaging approach. First, the system imperfections and parameter uncertainties are addressed by the experiments listed in section 5.1. In the following section 5.2, parameter studies by the simulation of different simulation-based IR (SIMBA IR) and simulation-based DESPOT1-HIFI (SIMBA DESPOT1-HIFI) methods for quantitative imaging are described. Furthermore, parameters of phantom and *in vivo* measurements are listed. The results of the experiments on the parameter uncertainties can be found in section 6.1, which is followed by section 5.2 on the results for the simulation-based T_1 quantification, as well as phantom and *in vivo* measurements.

5.1 Parameter Uncertainties

Within this section, the experimental setups for the measurements regarding the quantification of the parameter uncertainties are specified. All of the following sections can be read side by side to the corresponding results in section 6.1. Section 5.1.1 gives a description of the experiment to quantify the variations of the static magnetic field. The determination of the radio frequency (RF) field inhomogeneity is addressed by the experiment delineated in section 5.1.2.

5.1.1 Static Magnetic Field Inhomogeneity

To quantify the static magnetic field inhomogeneity for *in vivo* conditions in a spatially resolved manner, the method outlined in section 3.3.1 was applied. Three healthy volunteers (volunteer A: male, 80 kg, 32 yr; volunteer B: female, 70 kg, 27 yr; volunteer C: female, 78 kg, 28 yr) were examined. The Siemens sequence *gre_field_map* was set to the parameters listed in table 5.1. This sequence acquires a k-space line twice with the same tr, but alternating between the two echo times. In this case the difference of the echo times is fixed to 1.02 ms. Within the specific absorption rate (SAR) and peripheral nerve stimulation (PNS) constraints, the total measurement time was 4:16 min for each orientations. Imaging was performed with the 24-channel Nova Medical coil in three orthogonal orientations: coronal, sagittal, and transverse plane. For all datasets the brain was segmented and then evaluated by a self-implemented MATLAB-based plug-in for the DIPP environment. The results are shown in section 6.1.1 and discussed in section 7.1.

Table 5.1: Sequence parameters: ΔB_0 quantification *in vivo*. Listed are the readout tip angle α, echo time te, repetition time tr, readout bandwidth BW, and resolution Δr. The sequence is based on a multi-contrast GRE imaging scheme.

	readout				field of view		
contrast	α [°]	te [ms]	tr [ms]	BW [Hz/px]	slices	matrix [px^3]	Δr [mm^3]
1	47.0	3.25	n/a	488	16	192×256×1	1×1×3
2	47.0	4.27	660.00	488	16	192×256×1	1×1×3

5.1.2 Radio Frequency Field Inhomogeneity

The *in vivo* RF field inhomogeneity was quantified spatially resolved by the method presented in section 3.3.2. As for the B_0 quantification in section 5.1.1, the same three subjects were holding as volunteers. All important imaging parameters of the applied work-in-progress sequence *tfl_WIP543_B1map* by Siemens are specified in table 5.2. The preparation parameters are given in a separate table 5.3. The total measurement time was 3:33 min per orientation, respecting all safety constraints. Again, imaging was performed in all three orthogonal orientations with the 24-channel Nova Medical coil. Data was evaluated by a self-implemented MATLAB-based DIPP plug-in on the segmented brain. The B_1 maps and values are presented and discussed in sections 6.1.2 and 7.1, respectively.

Table 5.2: Sequence parameters: ΔB_1 quantification *in vivo*. Listed are the readout tip angle α, echo time te, repetition time tr, readout bandwidth BW, and resolution Δr. The two contrasts were acquired within the same sequence, but in consecutive measurements; readout and FOV parameters were identical. All parameters regarding the preparation are specified in table 5.3.

	readout				field of view		
contrast	α [°]	te [ms]	tr [ms]	BW [Hz/px]	slices	matrix [px^3]	Δr [mm^3]
all	7.0	2.33	n/a	488	16	192×256×1	1×1×3

Table 5.3: Preparation parameters: ΔB_1 quantification *in vivo*. Listed are the preparation tip angle α_{prep}, inversion time TI, and repetition time TR of the preparation. An inversion time is not regarded within the evaluation process and is assumed to be effectively zero.

	preparation		
contrast	α_{prep} [°]	TI [ms]	TR [ms]
1	0.0	eff. 0	6600
2	90.0	eff. 0	6600

5.2 Volumetric T_1 Quantification

This section specifies the simulation parameters and the experimental setups for all investigations of the longitudinal relaxation times by the novel simulation-based quantitative imaging methods. The following sections can be read side by side to the corresponding results in section 6.2, respectively. It starts off with the descriptions of the simulations and experiments regarding the SIMBA IR method in section 5.2.1. In section 5.2.2, the simulation analyses and phantom measurements by the SIMBA DESPOT1-HIFI method are delineated. Eventually, section 5.2.3 specifies the setup for experimental *in vivo* imaging of two different parts of the human body.

5.2.1 Simulation-Based Inversion Recovery

For all sections regarding the SIMBA IR experiments, a set of lookup tables has been calculated from the simulations. It encompasses the correction techniques of signal scaling by the inversion recovery (IR) signal equation as well as by the approach with a reduced repetition time of the preparation, virtual initial magnetization, and signal matching. The longitudinal relaxation time T_1 and the tip angle scaling factor κ have been varied in the ranges from 500 ms to 4500 ms in steps of 10 ms and 0.025 to 2.500 in steps of 0.025, respectively (see figure 5.1(a)). All sequence parameters are summarized in table 5.4; the inversion time and the repetition time of the preparation were varied throughout the experiments and specified in the corresponding sections. The matrix was set to a size of 256×256×176 px^3.

A sample dataset consists of variation of the longitudinal relaxation time T_1 and the tip angle scaling factor κ in the ranges from 1100 ms to 2200 ms in steps of 100 ms as well as one value of 4000 ms and 0.25 to 1.50 in steps of 0.25, respectively (see figure 5.1(b)). The equilibrium magnetization M_0 was normalized to 1 and the noise N was set to 0.

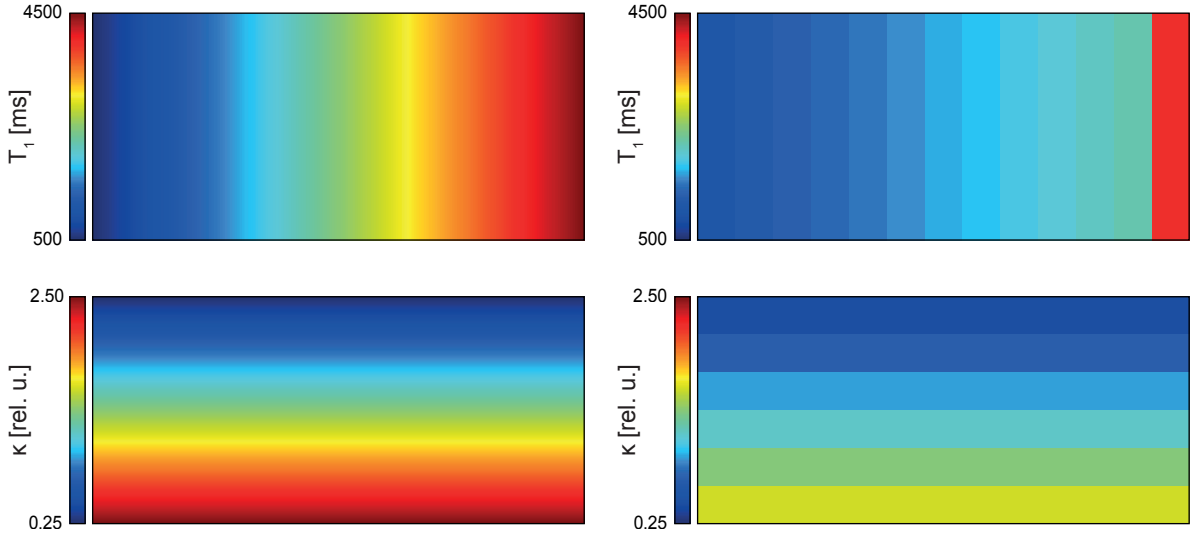

(a) (b)

Figure 5.1: Magnetization parameters: (a) A highly resolved parameter space of a variation of the longitudinal relaxation time T_1 (left to right) and the scaling factor of the tip angle κ (top to bottom) was used for the calculation of the correction lookup tables. (b) The sample dataset consisted only of a few sample point typically encountered for *in vivo* conditions.

Table 5.4: General simulation parameters: SIMBA IR. All important sequence parameters are listed: pulse durations τ, tip angles α, echo time te, repetition time tr, and bandwidth BW. The resolution does not play a role for the calculation of the correction libraries. The inversion and repetition times of the preparation are given for the specific experiments.

preparation			readout				
τ_{prep} [ms]	α_{prep} [°]	ordering	τ [ms]	α [°]	te [ms]	tr [ms]	BW [Hz/px]
10.24	180.0	centric	1.00	7.0	1.99	4.36	488

Evaluation Strategies The intention of this experiment it to evaluate the performance of the different evaluation strategies introduced in section 4.2. For this reason, the MR signal for each data point of the sample dataset from has been simulated. The simulation parameters correspond to those of the following experiment with a minimized repetition time *TR* of the preparation in section 5.2.1: Variation of the Repetition Time. The longitudinal relaxation time T_1 was quantified by the two different optimization approaches (`single-start`, `multi-start`), the two signal simulations (`offset`, `filter`), and the four different correction techniques (`scaled IR`, `scaled IRTR`, `virtual M`, `matched`). The corresponding results and conclusion are shown in section 6.2.1: Evaluation Strategies.

Variation of the Repetition Time The aim of this experiment was to reveal the impact of the repetition time *TR* of the preparation on the evaluation quality. This experiment is also based on the simulated MR signal of each data point of the sample dataset. 16 inversion times *TI* were distributed equidistantly along the signal evolution for a longitudinal

relaxation time T_1 of 1650 ms. The inversion was performed by an optimized adiabatic hyperbolic secant (HS) pulse with a tip angle of 180 ° and the readout was a single-shot *fast low angle shot* (FLASH) technique, all k-space lines were acquired following one preparation. All sequence parameters regarding the preparation are listed in table 5.5. The evaluation was again performed by all combinations of the optimization, signal simulation, and correction approaches. The results are presented in section 6.2.1: Variation of the Repetition Time.

Table 5.5: Preparation simulation parameters: Variation of the Repetition Time. The magnetization preparation was realized by an adiabatic HS pulse. Each signal was simulated at different inversion times *TI*. The repetition times *TR* of the preparation were chosen in such a way, that the delay time *TD* between the readout and the next preparation accounted to 3000 ms and 0 ms, respectively.

	preparation		
contrast	*TI* [ms]	*TR* [ms]	TR_{min} [ms]
1	42	4164.03	1164.03
2	153	4275.03	1275.03
3	271	4393.03	1393.03
4	399	4521.03	1521.03
5	539	4661.03	1661.03
6	689	4811.03	1811.03
7	857	4979.03	1979.03
8	1043	5165.03	2165.03
9	1251	5373.03	2373.03
10	1491	5613.03	2613.03
11	1773	5895.03	2895.03
12	2109	6231.03	3231.03
13	2536	6658.03	3658.03
14	3114	7236.03	4236.03
15	4001	8123.03	5123.03
16	6087	10209.03	7209.03

Variation of the Pulse Class This experiment was intended to point out the impact of the pulse class of the preparation on the evaluation quality. The MR signal of each data point of the sample dataset was simulated. The preparation was performed by a non-adiabatic rectangular pulse. All timing parameter were selected corresponding to the experiment above (see experiment in section 5.2.1: Variation of the Repetition Time). Slight changes come from the difference of the inversion pulse duration which has been reduced from 10.24 ms to 1.00 ms. The respectively adapted preparation parameters are listed in table 5.7. All evaluation strategies were applied within the evaluation process. The results are presented in the corresponding section 6.2.1: Variation of the Pulse Class.

Table 5.6: General simulation parameters: Variation of the Pulse Class. All important sequence parameters are listed: pulse durations τ, tip angles α, echo time te, repetition time tr, and bandwidth BW. The resolution does not play a role for the calculation of the correction libraries. The inversion and repetition times of the preparation are given for the specific experiments.

preparation			readout				
τ_{prep} [ms]	α_{prep} [°]	ordering	τ [ms]	α [°]	te [ms]	tr [ms]	BW [Hz/px]
1.00	180.0	centric	1.00	7.0	1.99	4.36	488

Table 5.7: Preparation simulation parameters: Variation of the Pulse Class. The magnetization preparation was realized by a non-adiabatic rectangular pulse. Each signal was simulated at different inversion times TI. The repetition times TR of the preparation were chosen in such a way, that the delay time TD between the readout and the next preparation accounts to 3000 ms and 0 ms, respectively.

	preparation		
contrast	TI [ms]	TR [ms]	TR_{min} [ms]
1	42	4158.61	1158.61
2	153	4269.61	1269.61
3	271	4387.61	1387.61
4	399	4515.61	1515.61
5	539	4655.61	1655.61
6	689	4805.61	1805.61
7	857	4973.61	1973.61
8	1043	5159.61	2159.61
9	1251	5367.61	2367.61
10	1491	5607.61	2607.61
11	1773	5889.61	2889.61
12	2109	6225.61	3225.61
13	2536	6652.61	3652.61
14	3114	7230.61	4230.61
15	4001	8117.61	5117.61
16	6087	10203.61	7203.61

Measurements This experiment consists of the actual measurements and evaluations with the SIMBA IR method. The impact of a variation of the repetition time *TR* of the preparation and of the pulse class was investigated by a measurement of the contrast phantom described in section 3.1.4. The respective sequence parameters can be depicted from tables 5.4, 5.5, and 5.7, respectively. The measurement was performed with the 24-channel Nova Medical coil, and detailed imaging parameters are listed in section 6.2.2. The evaluation was conducted by the `single-start` optimization based on both signal simulations (`offset`, `filter`) and the `matched` correction only. All results are presented and interpreted in section 6.2.1: Measurements.

5.2.2 Simulation-Based DESPOT1-HIFI

Analogous to section 5.2.1 about the experimental setup of the SIMBA IR method, this section lists the respective setups of the SIMBA DESPOT1-HIFI experiments. The correction tables were based on the same parameter spaces as illustrated in figure 5.1. The sequence parameters as listed in table 5.4.

Furthermore, a second set of sequence protocols was set up for the *in vivo* examinations. Respect has been given to the SAR and PNS constraints. As a consequence, the tip angles were reduced and the timings were prolonged, respectively. The adapted parameters are presented in table 5.8. This time, the tip angle of the readout was also varied for the FLASH experiments. All parameters influencing the desired contrasts are listed for the respective experiment.

Table 5.8: General simulation parameters: SIMBA DESPOT1-HIFI. All important sequence parameters are listed: pulse durations τ, tip angles α, echo time *te*, repetition time *tr*, and bandwidth BW. The resolution does not play a role for the calculation of the correction libraries. The inversion and repetition times of the preparation are given for the specific experiments.

preparation			readout				
τ_{prep} [ms]	α_{prep} [°]	ordering	τ [ms]	α [°]	*te* [ms]	*tr* [ms]	BW [Hz/px]
10.24	180.0	centric	1.00	n/a	1.99	5.43	488

Combination Strategies To identify the combination of IR and FLASH contrast which performs the most accurate, all possible sets are tried out. For this reason, the MR signal was simulated for each contrast and data point of the sample dataset. The inversion time *TI* has been varied in the range of 250 ms and 2000 ms with a fixed repetition time *TR* of the preparation of 3000 ms. The readout tip angle α of the FLASH experiments was varied between 3 ° and 12 °. All simulation parameters are listed in table 5.9. Additionally, the stability regarding *in vivo* like noise was investigated. Each entry in the sample dataset was attributed by random noise 192 times. The complex noise level was estimated from a measurement to be 2.00 % of the equilibrium signal and was not affected by the signal level itself. On a magnitude signal, the noise level can be defined by:

$$N_{\text{mag}} = \frac{1}{0.66}\sqrt{N_{\text{real}}^2 + N_{\text{imag}}^2} \ , \tag{5.1}$$

and comes out to 4.29 %. All evaluation strategies are applied within the evaluation process. The respective results are presented in the section 6.2.2: Combination Strategies.

Table 5.9: Preparation simulation parameters: Combination Strategies. Each signal was simulated at different inversion times *TI* and the corresponding repetition time *TR* of the preparation of the IR experiments (left table) as well as for different readout tip angles α of the FLASH experiments (right table).

	preparation	
contrast	*TI* [ms]	*TR* [ms]
1	250	3000
2	500	3000
3	750	3000
4	1000	3000
5	1250	3000
6	1500	3000
7	1750	3000
8	2000	3000

	readout
contrast	α [°]
1	3.0
2	6.0
3	9.0
4	12.0
5	15.0
6	18.0

Measurements At last, quantitative imaging of the longitudinal relaxation time by the SIMBA DESPOT1-HIFI experiment was performed by a magnetic resonance imaging (MRI) experiment with the contrast phantom specified in section 3.1.4. The first half of the sequence parameters can be extracted from table 5.9. For the second half, the adapted timing parameters are listed in table 5.10. The measurements were performed with the 24-channel Nova Medical coil, and detailed imaging parameters are listed in section 6.2.2. The evaluation was conducted by the `single-start` optimization based on both signal simulations (`offset`, `filter`) and the `matched` correction only. All results are presented and interpreted in section 6.2.2: Measurements.

Table 5.10: Preparation simulation parameters: Combination Strategies. Each signal was simulated at different inversion times *TI* and the corresponding repetition time *TR* of the preparation of the IR experiments.

	preparation	
contrast	*TI* [ms]	*TR* [ms]
1	1251	1934.95
2	3114	4509.95

5.2.3 Simulation-Based DESPOT1-HIFI *in vivo*

This last section holds the descriptions of the experiments for *in vivo* quantitative imaging. For the analyses of the acquired datasets, the SIMBA DESPOT1-HIFI method was used. In these experiments, the lookup tables were the same as for the phantom experiments specified in section 5.2.2.

Whole Brain For this experiment, one healthy volunteer (male, 64 kg, 23 yr) was examined with the SIMBA DESPOT1-HIFI method. Two adiabatically prepared IR and two FLASH contrasts were acquired within 28:57 min. The measurement was conducted with the 24-channel Nova Medical coil, and detailed imaging parameters are listed in section 5.2.2. Additionally, the inhomogeneities of the static magnetic and the RF field were measured in transverse orientation. For those, the same parameters were used as given in sections 5.1.1 and 5.1.2. The image data was evaluated with a `single-start` optimization based on the `filter` signal simulation and corrected with the `matched` approach. More information on this evaluation is given in section 5.2.1). The results of the whole brain evaluation are given in section 6.2.3: Whole Brain.

Calf Muscle In this experiment, one healthy volunteer (female, 80 kg, 30 yr) was examined with the non-adiabatic SIMBA DESPOT1-HIFI method. Imaging was performed with the 28-channel Siemens knee coil and imaging parameters identical to those of the phantom measurements described in section 5.2.2. The measurement was carried out within 28:55 min. For the quantification of static magnetic and RF field inhomogeneities, the same measurements were conducted as stated in section 5.2.3 above. Also similar to the experiment above was the data analysis. The results of this experiment are presented in section 6.2.3.

6 Results Part II: Evaluation of Simulations and Experiments

In this chapter, the results of simulations as well as phantom and *in vivo* measurements are presented for the novel simulation-based quantitative imaging approach. The evaluation strategies that lead to these results are stated in chapter 5. Initially, the ranges of parameter uncertainties encountered in real experiments are evaluated in section 6.1. All results of validation experiments in simulations and phantom experiments for the simulation-based quantitative imaging techniques are shown in the first part of section 6.2. The last part in section 5.2.3 concludes with the findings of two different *in vivo* experiments. All results presented here are discussed in the chapter 7, section 7.1 for the impact of the parameter uncertainties and section 7.3 for the performance of the simulation-based quantitative imaging in the respective experiments.

6.1 Parameter Uncertainties

In this section, the results of the measurements for the quantification of the parameter uncertainties are presented. The two sections below can be read side by side to the description of the experimental setups in section 5.1 according to the numbering. Section 6.1.1 holds the information about the inhomogeneity of the static magnetic field and quantifies the dynamic range of the field amplitude variations. The respective results of the radio frequency (RF) field inhomogeneity measurements are presented in section 6.1.2 in images and in numbers.

6.1.1 Static Magnetic Field Inhomogeneity

The intention behind this experiment is to quantify the variations of the static magnetic field strength. If the statistics of the spatial distribution are known, then the effects of the applied RF pulses on the magnetization can be investigated to be independent of the off-resonances within the respective dynamic range. This information is necessary for the correction libraries of the simulation-based correction techniques to be valid, see section 4.2. The experimental setup for the quantification is described in section 5.1.1.

At first, figure 6.1 shows three exemplary slices for one volunteer in coronal, sagittal, and transverse orientation, respectively. Only the brain is extracted from the original image data. The variations of the static magnetic field are specified by deviations from the nominal magnetic field ΔB_0 according to the LARMOR frequency defined by the system adjustments. Greenish colored regions show nearly on-resonant conditions, while the blue and red areas indicate negative and positive field strength deviations. Overall, the maps appear smooth. A drop of the static magnetic field in feet direction can be depicted from the coronal view in figure 6.1(a). More striking is the strong regional inhomogeneity in the proximity to the nasal cavities marked by the blue arrows in figures 6.1(b,c). The deviation comes out to more than 1.65 ppm which is the maximum resolvable value in this experiment. To interpret this correctly, the theory from section 3.3.1 must be recalled. This method is based on the phase shift of the complex signal in the time between the two echoes due to off-resonance. If the phase shift exceeds the angle of π, a phase wrap occurs and leads to false results. The hard drop from red to blue colored values in figure 6.1(b) is indicating this; the apparent negative deviations are actually positive. Both appearances of the static magnetic field inhomogeneity are caused by the hard change in the susceptibility of the cavities filled with air, bone, and the soft tissue of the brain.

The second figure 6.2 shows the normalized histograms of the static magnetic field deviations for the three volunteers. Each is represented by an individual color (blue, green, red), but hard to differentiate from the others. The centers of all distributions are located at nearly the same position and the full width at half maximum (FWHM) values are also similar. The offset of the centers of gravity is due to the fact, that contributions only from the brain are regarded. Deviations of the subcutaneous fat and the throat region are not taken into account, but included in the system adjustments volume. The asymmetry of the histogram towards lower values, appearing as a broadening of the distribution from -0.25 ppm to -0.50 ppm, is caused by the same reason. Because the results are reproducible on a number of volunteers, the resulting statistics are based on the totality of all three volunteers.

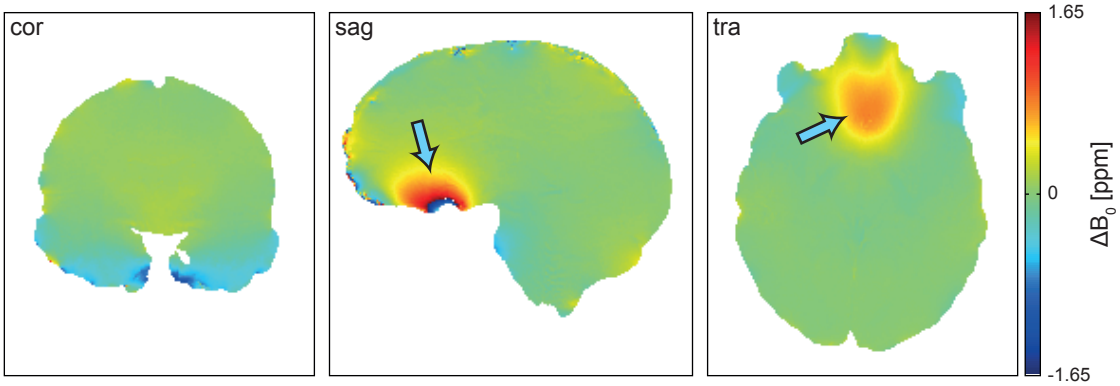

(a) (b) (c)

Figure 6.1: Static magnetic field map *in vivo*: (a) A coronal, (b) sagittal, and (c) transverse view of one healthy volunteer is shown; FOV of 256×256 mm^2, 16 slices for each orientation, resolution of 1 mm, slice thickness of 3 mm, and acquisition time of 4:13 min. The deviation ΔB_0 from the nominal B_0 value is presented in the unit parts per million. A smooth drop of the field strength can be observed in the feet direction in the coronal view (a). In the proximity of the nasal cavities, a strong regional inhomogeneity of more than 1.65 ppm is marked by the blue arrows in the sagittal and transverse view (b,c). Both appearances are caused by the hard change in the susceptibility of cavities filled with air, bone, and the soft tissue of the brain.

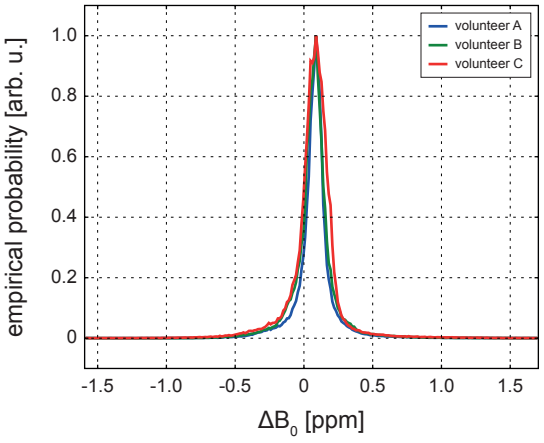

Figure 6.2: Static magnetic field distribution: The data is presented for three healthy volunteers. Shown is the normalized empirical probability of the different static magnetic field deviations ΔB_0. The differently colored line profiles (blue, green, red) of the volunteers show a strong agreement. The centers of gravity have an offset from zero and a slight asymmetry towards lower ΔB_0 values appears. This is due to the masking; structures outside the mask but within the system adjustment volume would correct for this.

Table 6.1: Static magnetic field percentiles: average of three healthy volunteers. The extremum values of the static magnetic field deviation ΔB_0 specify the range outside of which the given percentage p of the distribution is located.

p [%]	$\Delta B_{0,\min}$ [ppm]	$\Delta B_{0,\max}$ [ppm]
95	0.007	0.059
90	-0.007	0.073
75	-0.033	0.099
50	-0.099	0.139
25	-0.218	0.218
10	-0.455	0.416
5	-0.627	0.680

The complete experiment is summarized in table 6.1 at last. Here, the minimum $\Delta B_{0,\min}$ and maximum values $\Delta B_{0,\max}$ of the static magnetic field deviations for the corresponding relative fractions outside of the respective dynamic ranges are listed. The asymmetric distribution can be reconstructed from the nonuniform shift of the ΔB_0 limits. An average FWHM accounts to 0.238 ppm. Vice versa to the presented numbers of table 6.1, it can be concluded, that 90 % of all data points are within $\Delta B_{0,\min}$ and $\Delta B_{0,\max}$ of -0.455 ppm and 0.416 ppm, respectively. Thus, the corresponding variation width comes out to 0.871 ppm. This value will hold as a reference for the range in which the quantitative imaging approach, presented in section 4.2, must cope with the variations of the static magnetic field.

Not shown within this thesis is the experimental validation of the performance of a rectangular and a hyperbolic secant (HS) RF pulse for these off-resonances. These pulses are used for the novel simulation-based quantification of the longitudinal relaxation time. Studies performed on the homogeneity phantom, see section 3.1.4, revealed that the changes in the effect of the different RF pulses do not significantly impact the evaluation accuracy. Thus, the inhomogeneity of the static magnetic field must not be regarded for within the simulation. This way, one free regression parameter can be omitted, stabilizing the evaluation, and the computational burden for the calculation of the lookup tables for the correction is reduced.

6.1.2 Radio Frequency Field Inhomogeneity

This section holds the results of the experiments about the inhomogeneity of the RF field distribution. A variation of the tip angle leads to a deviation in the signal and thus, it must be known to be handled properly by the simulation-based correction techniques, see section 4.2. The experimental setup of the experiment is described in section 5.1.1.

Analogous to the section above, three orthogonal views of the relative ΔB_1 map are shown in figure 6.3. Again, the results are only presented for the extracted brain. The ΔB_1 values are presented in units relative to the nominal B_1 set in the imaging sequence. Regions where the actual tip angle equals the nominal one are colored in green. Deviations to lower and higher values are colored in blue and red, respectively. Four appearances within the figure must be pointed out. At first, a drop of the B_1 amplitude can be observed towards the feet direction in figures 6.3(a,b) and in the left and right outer regions in figure 6.3(c). The drop towards the feet is due to the limited field of view (FOV) and the geometry of the transmission RF coil (see section 3.1.2). Why the RF field amplitude drops towards the sides of the brain is unknown. The second appearance is the hyperintense region in the center of the brain; also called central brightening and introduced in section 2.3.3. Two more phenomena of unknown cause are also present in the ΔB_1 maps. One is the appearance of anatomical structures within the maps. Especially in the areas of central brightening, the ventricles filled with cerebrospinal fluid (CSF) can be depicted by the red arrows. It is unclear whether the CSF focuses the B_1 field of the RF wave or the evaluation method fails. One reason for the failure might be due to the long longitudinal relaxation time of CSF and thus, the incomplete relaxation process between the data acquisitions. Finally the last appearance is the scattered cut at very low ΔB_1 values from blue to white shown in figures 6.3(a,b) at the bottom and marked by the yellow arrows. This is not caused by the masking of the brain, but rather by a failure of the evaluation process at

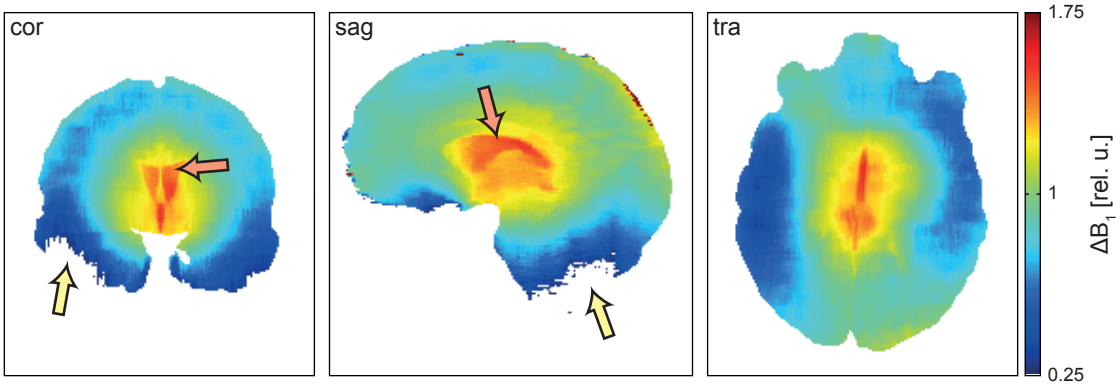

(a) (b) (c)

Figure 6.3: Radio frequency field map *in vivo*: (a) A coronal, (b) sagittal, and (c) transverse view of one healthy volunteer is shown; FOV of 256×256 mm^2, 16 slices for each orientation, resolution of 1 mm, slice thickness of 3 mm, and acquisition time of 4:13 min. The deviation ΔB_1 from the nominal value is presented as a relative scaling factor. Four appearance catch the eye: i) a low value region in feet directions in (a,b) and to both sides of the brain in (c), ii) a high value region of the central brightening, iii) the presence of anatomical structure, e. g. the ventricles marked by the red arrows, in the RF field maps, iv) and the failure of the evaluation process in the lower parts of (a,b) for B_1 values close to zero (indicated by yellow arrows).

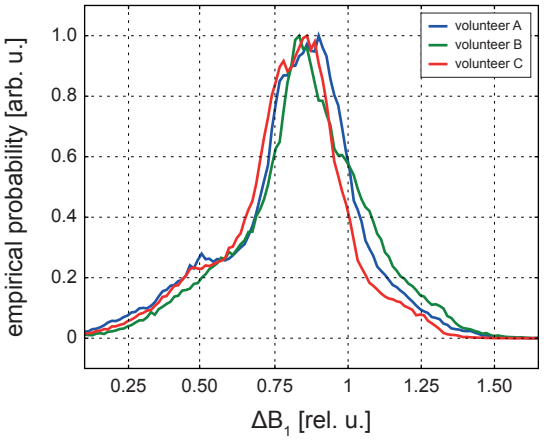

Figure 6.4: Radio frequency field distribution:The data is presented for three healthy volunteers. The normalized empirical probability of the RF field deviations ΔB_1 is shown. All values for the volunteers (blue, green red) are in good agreement with each other. The distributions are asymmetric with preferences to lower values. Likewise, the centers of gravity are shifted towards lower values. Again, this is due to the masking; structures outside the mask but within the system adjustment volume would correct for this.

Table 6.2: Radio frequency field percentiles: average of three healthy volunteers. The minimum and maximum values of the RF field deviation ΔB_1 specify the range outside of which the given percentage p of the distribution is located.

p [%]	$\Delta B_{1,\mathrm{min}}$	$\Delta B_{1,\mathrm{max}}$
95	0.756	0.927
90	0.743	0.940
78	0.690	1.006
50	0.467	1.111
25	0.309	1.269
10	0.178	1.348
5	0.099	1.992

B_1 and signal values close to zero. Overall, the maps hold as a good approximation of the actual RF field distributions for *in vivo* conditions.

Figure 6.4 shows the distributions of the RF field inhomogeneity ΔB_1 for all volunteers. In general, the distributions are in a good agreement with each other. The centers of gravity of the determined distributions are shifted again. This is for the same reason as for the deviation of the static magnetic field above. Regions excluded by the evaluation mask, especially those in proximity to the coil itself, do not contribute to these statistics but to the reference within the system adjustment value. The asymmetry of the distribution is more obvious than before; a higher probability exists for low ΔB_1 values. For two of the volunteers, a local maximum of the empirical probability exists close to ΔB_1 values of 0.5.

The statistics of the totality of all volunteers are presented in table 6.2. Percentiles are defined by the minimum $\Delta B_{1,\mathrm{min}}$ and maximum values $\Delta B_{1,\mathrm{max}}$ that define the dynamic range outside of which the respective fraction of data points is located. The mean FWHM of the distributions comes out to 0.644. By taking the 90 % percentile as a reference value again, the respective variation width is 1.170. As a consequence, the novel quantitative imaging method presented in section 4.2 must handle ΔB_1 values between 0.178 and 1.348.

The calculation of the lookup tables of the correction libraries, outlined in section 5.2, has been based on this dynamic range. For more information on how the evaluation performs see the corresponding experiments in sections 6.2.1, 6.2.2, and 6.2.3.

6.2 Volumetric T_1 Quantification

This section holds the results of the simulation analyses as well as the phantom and *in vivo* measurements regarding the quantification of the longitudinal relaxation time T_1. All of the following sections can be read side by side to the respective descriptions of the parameters and setups listed in section 5.2.

The results are split up into three parts. At first, it is demonstrated in section 6.2.1 how the simulation-based IR (SIMBA IR) evaluation strategies perform under various sequence protocol settings. To make the technique feasible for *in vivo* applications within a clinical time frame, the transition to the simulation-based DESPOT1-HIFI (SIMBA DESPOT1-HIFI) method is carried out and presented in section 6.2.2. In section 6.2.3, initial *in vivo* examinations of two different parts of the human body are shown at last.

6.2.1 Simulation-Based Inversion Recovery

The investigation of the different evaluation strategies of the SIMBA IR method on an exemplary sample dataset is presented at first. The second experiment regards the variation of the repetition time of the preparation and how it impacts the measurement time and the evaluation accuracy. Next, the variation of the pulse class of the preparation is addressed and how it influences the quantification performance. At last, the phantom measurements will serve as a validation of the new method for the quantification of the longitudinal relaxation time.

Evaluation Strategies This experiment is intended to investigate the performance of the different evaluation strategies and point out the main advantages and disadvantages. A

description of the simulation parameters is given in section 5.2.1: Evaluation Strategies.

Figure 6.5 shows the results of the quantification of the equilibrium magnetization M_0, the longitudinal relaxation time T_1, the tip angle scaling factor κ, and the noise N. Two optimization approaches (`single-start`, `multi-start`) were applied as presented in section 4.2.7. Furthermore, the corrections were based on two different signal simulations (`offset`, `filter`) that have been introduced in sections 4.2.4 and 4.2.5. The different correction techniques (`scaled IR`, `scaled IRTR`, `virtual M`, `matched`) are outlined in section 4.2.6. Each of the 4×4 fields of the mosaic-view holds the results for the sample dataset shown in figure 5.1(b). Figure 6.5(a) holds the absolute values of the parameters and figure 6.5(b) the respective relative deviations from the nominal values.

At first, the performance of the two optimizations strategies is analyzed. For all simulation and correction approaches, the `single-start` and the `multi-start` technique reveal nearly the same results for most of the data points within each sample dataset (top two rows versus bottom two rows of the mosaic-views). A reduction of the number of failed evaluations from 14.7 % to 9.8 % can be depicted for the `multi-start` approach. Not shown within the figure is the computational burden. For the `single-start` approach the average computation time accounts to 1.3 s for one data point and to 37.4 s for the `multi-start` approach.

Next, the effects of the different correction approaches based on the `offset` signal are evaluated. Reading the mosaic-views from top to bottom: The equilibrium magnetization is mainly constant for all correction techniques and only features a few outliers for long nominal T_1 and small κ values (top row and right column of each mosaic-field in figure 6.5(a)). Figure 6.5(b) verifies these observations by highlighting these data points with the clipped color map in yellow and green. The deviation offset is smaller for the `matched` than for the other correction approaches. Furthermore, the deviation increases with for nominal κ values different from 1. The results for T_1 are an indicator for the failure of the evaluation as pointed out above. Especially short nominal T_1 data points corrected by the `scaled IR` and `scaled IRTR` approach are affected; the reason for this is explained below. In general, the remaining data point values are in good agreement with the sample dataset in figure 5.1(b). The same accounts for the tip angle scaling factor κ. Only κ values for data points with a failed evaluation as well as long nominal T_1 and large κ values show a deviation from the reference values. Noise terms N are nearly constant and close to zero. The target function of the failed data points is minimized by an overestimation of N.

The results for the corrections based on the `filter` signal show nearly the same dependencies. One striking difference regards the accuracy of the evaluation in evidence in figure 6.5(b). The disturbance by the readout due to a variation of the nominal κ values is resolved by considering the k-space filters. Neither M_0, κ, nor T_1 depend on the readout and are presented with a constant deviation near zero.

The cause of the evaluation failure is featured by the correction lookup tables as exemplarily shown in figure 6.6. Its color map is of an arbitrary scale and the entries correspond to the reference dataset presented in figure 5.1(a). The absolute values do not allow any conclusion about the accuracy or stability of the evaluation. It is different for the gradient of the correction values though. Both mosaic-fields for the `scaled IR` and the `scaled IRTR` approach show singularities at certain T_1 values. The line does smear out for large κ values. It changes its position in T_1 with a changing inversion time TI (not shown by figure 6.6). For the `scaled IRTR` approach, this transition takes effect more intense and thus, less TI

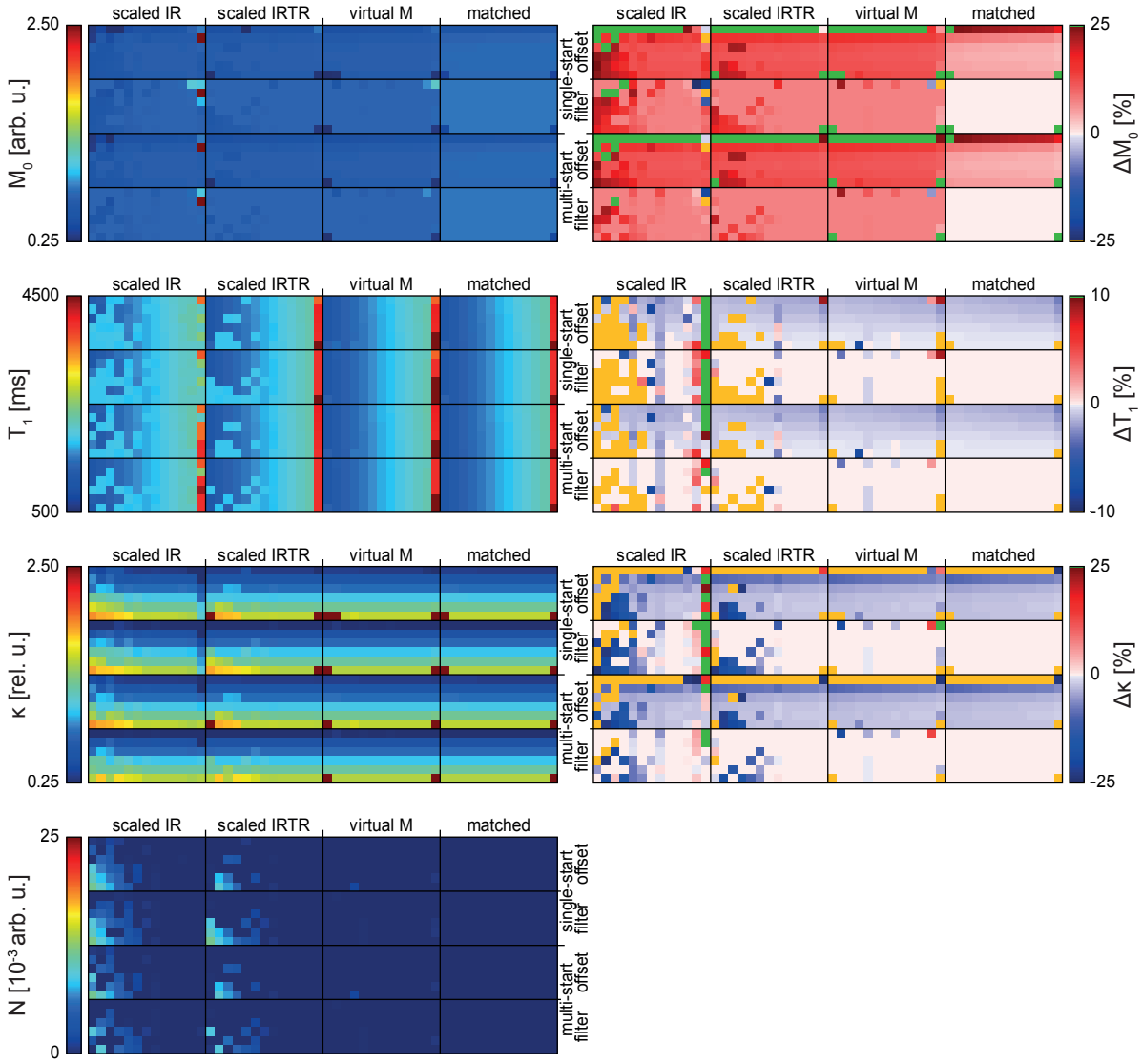

Figure 6.5: Evaluation strategies of the SIMBA IR experiment: The evaluations were performed on for the next experiment with an adiabatic preparation and a minimized repetition time TR of the preparation (see section 6.2.1: Variation of the Repetition Time). (a) The quantified parameters of the equilibrium magnetization M_0, the longitudinal relaxation time T_1, the tip angle scaling factor κ, and the noise N for different optimization (`single-start`, `multi-start`), signal simulation (`offset`, `filter`), and correction (`scaled IR`, `scaled IRTR`, `virtual M`, `matched`) approaches of the sample dataset are shown in each field of the mosaic-view. (b) The percental deviation from the nominal values is illustrated in a clipped color map. The main observations are: i) The additional computational burden of the `multi-start` optimization comes without a significant improvement of the quantification accuracy, ii) evaluations based on the `offset` signals are more stable but show a stronger deviations from the nominal longitudinal relaxation times, and iii) the corrections of the `matched` approach by the `filter` signals show the most accurate results.

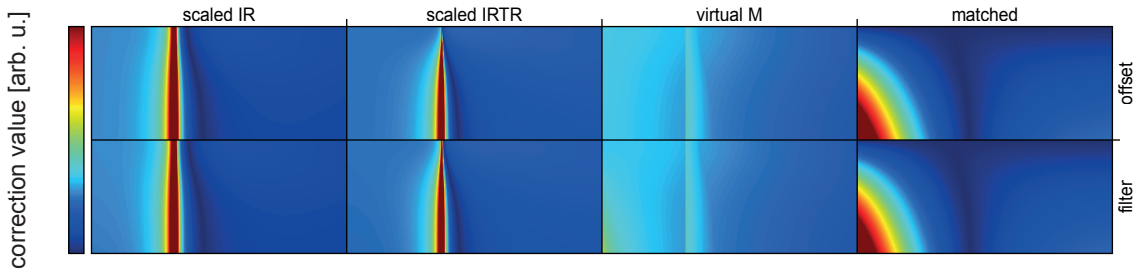

Figure 6.6: Correction lookup tables: The lookup tables belong to an adiabatic preparation and an inversion time TI of 1385 ms. All correction values are represented in arbitrary values. The two correction approaches `scaled IR` and `scaled IRTR` reveal a singularity at distinct T_1 values. This is caused by the calculation of the correction values and a division of zero values; the theoretical and simulated signal evolution have different temporal crossing of the transverse plane. Approaches by the `virtual M` and the `matched` correction do not feature such singularities. Especially for the lookup table of the `matched` correction, a smooth but strong curvature for the correction values exists.

sample points are affected. The singularity and the steep drop are the result of a division of zero values. Both, the theoretical and the simulated signal evolution have different temporal crossing of the transverse plane. With respect to the way the correction parameter is defined, see section 4.2.6, a rapid change of correction values of infinity and zero originates. Errors from the interpolated drawings from the lookup table in the region of singularities cause significant numerical instabilities within the optimization. As a result, a barrier in the target space is created. Literally speaking, if the momentum of the optimization algorithm is not sufficient, the barrier cannot be crossed, and the optimization will drift into a local minimum. The correction tables of the `virtual M` and `matched` approach are free of such singularities. Especially the `matched` correction methods show a smooth and strong curvature of the correction space.

The main conclusions of this experiment are summarized: An optimization by the `multi-start` approach comes with a high cost of computational burden and does not improve the quantification accuracy. The `offset` signal simulation yields a stable evaluation but strong deviation from the nominal parameters. Both signal scaling corrections `scaled IR` and `scaled IRTR` are sensitive to the distribution of the inversion time sample points. The highest and most stable evaluation accuracy is achieved with a `single-start` optimization, the `filter` signal simulation, and the `matched` correction.

Variation of the Repetition Time This experiment points out the benefits and drawbacks by a reduction of the repetition time TR of the magnetization preparation. The repetition time influences the available magnetization prior to the following preparation; see section 4.2.3. On the one hand this defines the dynamic range of the contrasts, and on the other hand it significantly impacts the total measurement time. The parameters of the simulation are listed in section 5.2.1: Variation of the Repetition Time.

The results for the quantification of the longitudinal relaxation time T_1 for two TR settings are presented in figure 6.7. Shown are the T_1 mean deviations ΔT_1 from the nominal values and the respective standard deviations averaged over the complete sample dataset. The blue markers belong to the TR settings that hold a delay time TD of 3000 ms. The brown

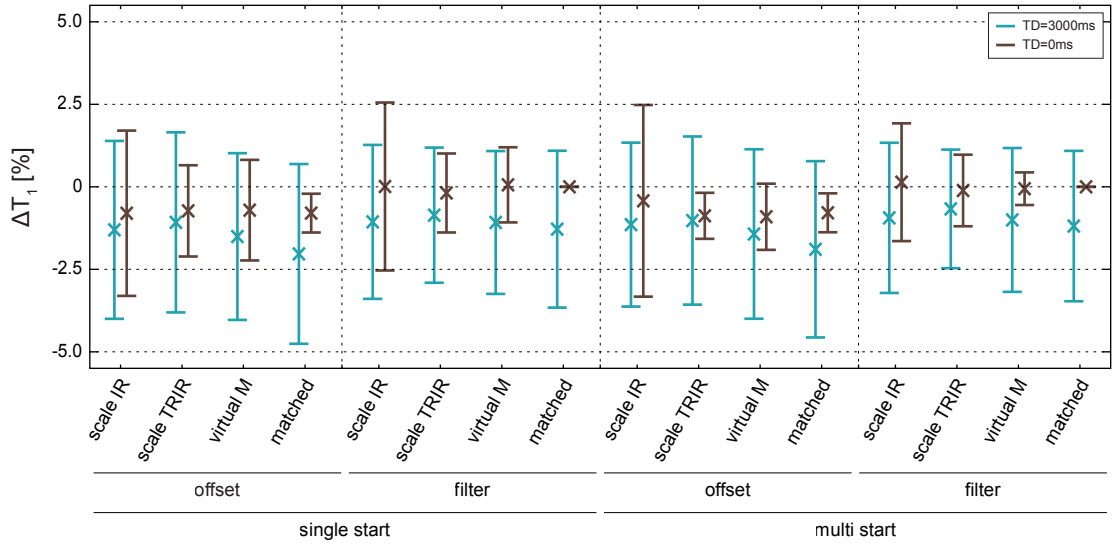

Figure 6.7: Statistics of SIMBA IR experiments with varying *TR*: The adiabatic preparation was performed with the repetition times *TR* of the preparation according to a delay time *TD* of 3000 ms (blue markers) and 0 ms (brown markers). Mean deviations from the nominal values of the longitudinal relaxation time ΔT_1 are presented in the units percent. The different evaluation strategies perform with the same characteristics as outlined in the experiment above (see section 6.2.1: Evaluation Strategies). Most striking is the impact on the evaluations due to a minimization of *TR*. Using an imperfectly relaxed state of the magnetization for the preparation yields a stronger weighting by T_1 and κ. Thus, the accuracy of the SIMBA IR improves with a reduction of *TR*. Additionally, the total measurement time is shortened by up to 50 %.

markers indicate the results without a delay time and thus the minimized *TR*. Again, the results are presented for the two different optimization approaches (`single-start` and `multi-start`), the two different signal simulations (`offset` and `filter`), and the four different correction techniques (`scaled IR`, `scaled IRTR`, `virtual M`, `matched`).

The main observations of this figure concern the performance for a variation of *TR* and not the evaluation strategies themselves (see section 6.2.1: Evaluation Strategies). The delay time is played out for each partition and thus 176 times within one inversion recovery (IR) sequence. With a minimization of *TD* from 3000 ms to 0 ms and for 16 different inversion times, the total measurement time is reduced by 140:48 min. Depending on the respective *TI* settings, this can add up to more than 50 % of the measurement time.

An imperfect relaxation prior to the inversion of the magnetization causes a strong weighting by the final state of the preceding preparation interval. For a fixed sequence protocol, this state depends on T_1 and κ only. As a consequence, the contrasts are differentiated more clearly. The common IR theory cannot predict this state to make use of it though. This is the reason why its performance is inaccurate by a systematic error for both experiment (see section 6.2.1: Measurements). However, the SIMBA IR method is capable of regarding it.

the following results can be derived from figure 6.7. The brown markers for the experiment corresponding to a minimized *TR* show a smaller deviation than the blue marker corresponding to the experiment with a *TD* of 3000 ms. An improvement in the accuracy can be determined for the `matched` correction based on the `filter` signal by 1.28 %. With a minimized *TR*, the evaluations are in a perfect agreement with all nominal values.

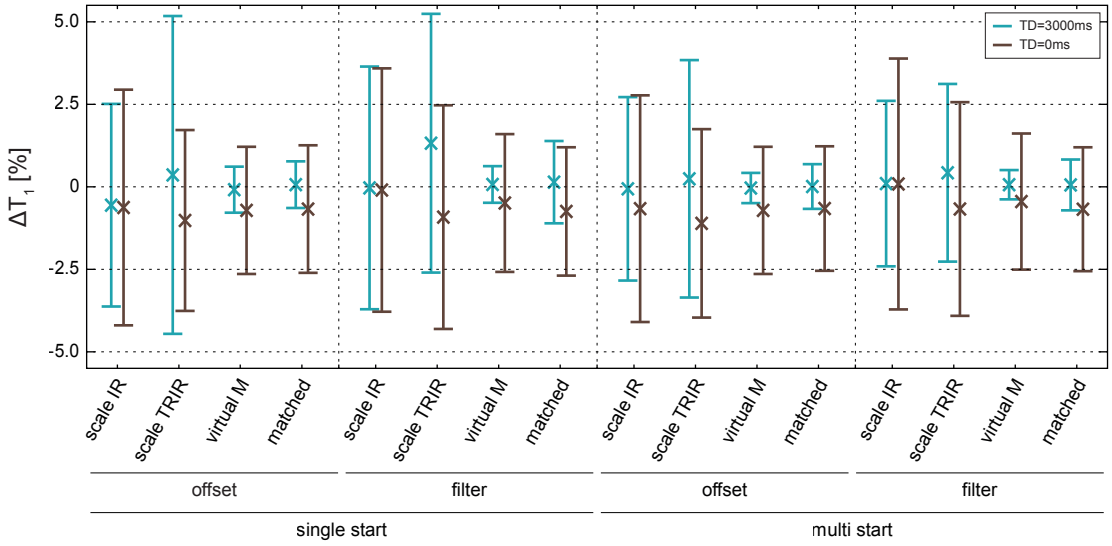

Figure 6.8: Statistics of SIMBA IR experiments with varying pulse class: The non-adiabatic preparation was performed with the repetition times TR of the preparation according to a delay time TD of 3000 ms (blue markers) and 0 ms (brown markers). Mean deviations from the nominal values of the longitudinal relaxation time ΔT_1 are presented in the units percent. In contrast to an adiabatic preparation (see figure 6.7), the reduction of TR reduces the uniqueness of the signal evolutions. Thus, the accuracy and the robustness of the quantification are impaired. Similar to the repetition time, κ also defines the initial state within the preparation from which the T_1 relaxation process starts. A feasible TR value improves the evaluation quality.

The main conclusions of this experiment are summarized again. A minimization of the repetition time TR of the preparation leads to a stronger weighting by the longitudinal relaxation time T_1 as well as the tip angle scaling factor κ and thus, a higher quantification accuracy. Along with this advantage additionally comes a significant reduction of the total measurement time by up to more than 50 %.

Variation of the Pulse Class This experiment has the intention to show the impact of the pulse class of the magnetization preparation on the evaluation accuracy and robustness. Replacing the adiabatic preparation pulse by a non-adiabatic rectangular pulse alters the quality of the contrast and the specific absorption rate (SAR) exposure. A detailed description of the experiment is given in section 5.2.1: Variation of the Pulse Class.

The results are again presented as a statistical analysis in figure 6.8. All sequence parameters have been specified to yield the same contrasts and timings as for the experiment above (see section 6.2.1: Variation of the Repetition Time).

The main focus of this experiment is on the effect of the non-adiabatic preparation and not on the evaluation strategies themselves (see section 6.2.1: Evaluation Strategies for more information). To recapitulate the basics again, the SAR exposure scales with B_1^2. Depending on the exact shape of the amplitudes of the RF pulses, the SAR exposure can be reduced by up to 70 % (not shown within the figure). This allows the imaging of organs of risk as well as imaging with inefficient coils that would exceed the SAR constraints.

The results are different and more complex to explain than for the adiabatic preparation (see figure 6.7). Besides the influence of TR on the initial state of the magnetization does the tip angle of the inversion pulse also has an impact on this. While κ values of 0.5 and 1.5

stand for a saturation recovery (SR) experiment, a value of 2.0 yields a tip angle of 360 ° and thus no preparation at all. For small and large κ values, the dynamic range in which the signal evolves during the inversion recovery time frame is reduced. The consequence is a reduced contrast. As a result, the reduced contrast degrades the uniqueness of the T_1 relaxation and thus the quantification accuracy of the longitudinal relaxation time.

The evaluation of the experiment with a partially relaxed magnetization by a prolonged *TR* generates more accurate results by 0.60 %. In comparison to the adiabatic preparation, the inversion by a rectangular pulse holds degraded quantification accuracy for a minimized repetition time of the preparation by 0.75 %. With a prolonged *TR* however, both preparation yield approximately the same accuracy and robustness.

A short summary of this experiment is given: The advantage of a non-adiabatic preparation is a significant reduction of the SAR exposure of up to 70 %. The disadvantage is a loss in uniqueness of the signal evolution due to a lack of contrast and thus a more inaccurate and unstable performance. However, with a feasible long repetition time, this can be counterbalanced.

Measurements The last section of the SIMBA IR experiments closes with the measurements of the contrast phantom described in section 3.1.4. The experiment is intended to validate the simulation-based evaluation strategies, show the impact of a reduction of the repetition time *TR* as well as the change of the pulse class of the preparation. Detailed information about the experimental setup and all sequence parameters is given in section 5.2.1: Measurements.

The evaluation is performed by the `single-start` optimization, both signal simulations, and the `matched` correction only. It is known from the experiments above, that the `multi-start` optimization approach does not improve the accuracy of the evaluation but comes at a high cost of computational burden. Corrections by the signal scaling and the virtual initial magnetization are inferior at certain inversion time sample points and the overall evaluation quality and are therefore disregarded.

Figure 6.9 shows the results of the quantification of the longitudinal relaxation time T_1. The determined T_1 values of this experiment are plotted against the reference values from an IR spin echo (SE) experiment (listed in table 3.2 in section 3.1.4 about the contrast phantom). A red diagonal marks the perfect correlation. The red and brown markers belong to the `offset` and `filter` signal simulation-based quantification, respectively. The blue markers belong to the evaluation by the common IR theory. Each marker's center is the mean value of T_1 within a region of interest (ROI) for each test tube. Its error bars indicate the corresponding standard deviations. Figure 6.9(a) holds the results for a delay time *TD* of 3000 ms and figure 6.9(b) for a *TD* of 0 ms.

The brown and the red markers overlap in figure 6.9. Both underestimate the reference values of the longitudinal relaxation time $T_{1,\mathrm{ref}}$. The deviation from the correlation diagonal increases for short and long $T_{1,\mathrm{ref}}$ values. Only for the two test tubes of the highest T_1 values is the reference overestimated. Just as a reminder it must be noted, that the distribution of inversion time sample points is optimized for a T_1 value of 1650 ms. The more the quantified parameters differ from the calibration the more inaccurate the results are. The values based on the `filter` signal simulation are closer to the reference value than the `offset` signal-based quantifications; except for the longest T_1 sample.

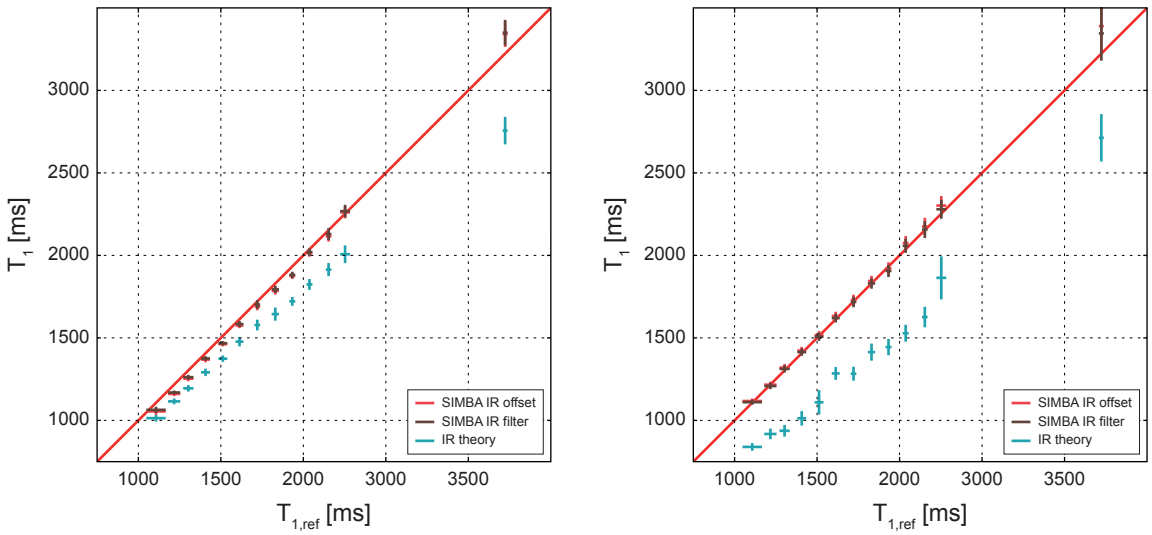

Figure 6.9: T_1 values by the adiabatic SIMBA IR method: The repetition time *TR* of the magnetization preparation is varied to correspond to (a) a delay time *TD* of 3000 ms and (b) a *TD* of 0 ms. A FOV with a 256×256×176 px^3 matrix and 1 mm isotropic resolution was acquired at 16 different inversion time *TI* values. The evaluation was performed with a `single-start` optimization based on the `filter` and `offset` signal and the `matched` correction. A red diagonal line represents a perfect correlation between the reference $T_{1,\mathrm{ref}}$ values determined by an IR SE experiment and the T_1 values of the SIMBA IR method (brown markers: `filter` signal, red marker:s `offset` signal) and the evaluation by common IR theory (blue markers). The center and the error bars of each marker correspond to the respective mean values and standard deviations within a ROI for each test tube of the contrast phantom. All values determined by the simulation-based evaluation strategies are in a strong agreement with the reference. The quantification based on the `filter` signal is slightly more accurate than based on the `offset` signal. Evaluations by the common IR theory show a strong overestimation of T_1 that increases with the $T_{1,\mathrm{ref}}$. A minimization of the repetition time of the preparation improves the accuracy of the simulation-based evaluations strategies and reduces the overall measurement time.

For medium T_1 values, the standard deviations are hardly noticeable. The variances get larger for short and long longitudinal relaxation times. As above, this fits to the SIMBA IR theory.

Evaluations by the common IR theory underestimate the T_1 stronger than by the simulation-based theory. The offset increases for long $T_{1,\mathrm{ref}}$ values. As before, this is partially due to the k-space filters, but not only. In the beginning of this section the meaning of the `offset` signal simulation has been introduced. The magnetization is in a different state at the end of each preparation block than predicted by the common theory. The signal magnitude is higher for short and lower for long inversion times. This flattens out the recovery curve and leads to an underestimation of the curvature and the T_1 value. A quantitative analysis of the different evaluations is given in the following.

The results have also been analyzed regarding the mean deviations $\Delta T_{1,\mathrm{mean}}$ of all quantified values and the corresponding standard deviations $\Delta T_{1,\mathrm{std}}$ as well as the coefficient of determination R^2. This is presented in table 6.3.

Table 6.3: T_1 accuracy by the adiabatic SIMBA IR method: Listed are the mean deviations $\Delta T_{1,\mathrm{mean}}$ and the corresponding standard deviations $\Delta T_{1,\mathrm{std}}$ as well as the coefficient of determination R^2 of the quantified longitudinal relaxation times presented in figure 6.9. The main conclusions are: i) The SIMBA IR approaches show a stronger correlation to the gold-standard than the common IR theory does; R^2 of 0.99 against 0.78. ii) Evaluations based on the `filter` signal simulation are more accurate than those based on the `offset` signal. iii) The minimization of *TR* leads to the most accurate results.

	TR			min. *TR*		
	original	SIMBA IR		original	SIMBA IR	
		offset	filter		offset	filter
$\Delta T_{1,\mathrm{mean}}$ [%]	9.79	2.14	1.61	23.68	-1.22	-0.42
$\Delta T_{1,\mathrm{std}}$ [%]	1.82	2.23	2.11	3.77	1.40	1.23
R^2	0.78	0.99	0.99	0.25	0.99	1.00

The mean deviations from the reference for the quantification by the `filter` and the `offset` signal simulations account to $(2.14 \pm 2.23)\,\%$ and $(1.61 \pm 2.22)\,\%$, respectively. This shows the strong agreement of the novel approach with the gold-standard of quantitative T_1 imaging with an R^2 of 0.99. An error in the range of a few percent at a reduction of the total measurement time of several hours for one slice by the gold standard to 2:16 h for 176 slices is possible. Performing the analysis of such fast data acquisition with the common IR theory holds an error of $(9.79 \pm 1.82)\,\%$. Although the standard deviation is smaller than for the SIMBA IR approaches, the mean deviation is too high for the method to be applicable for quantitative imaging.

Even higher is the accuracy for the data acquisition with a minimized repetition time *TR* of the preparation. The evaluations by the `filter` signal simulation overestimate the $T_{1,\mathrm{ref}}$ values by $(-0.42 \pm 1.23)\,\%$. The corresponding R^2 rounded to the second digit behind the comma comes out to 1.00. In contrast to this improvement, the common IR theory performs less accurate. An error of approximately 25 % is the result. As for the experiment with a prolonged *TR*, the standard deviation is small though.

The results for the SIMBA IR experiment and a non-adiabatic preparation are shown in figure 6.10 and table 6.4 in the same manner as for the results above; see descriptions of figure 6.9 and table 6.3, respectively. Only the difference between the results of the two different preparations will be pointed out.

For a prolonged *TR*, the SIMBA IR methods based on the `offset` and on the `filter` signal feature a mean deviation to the reference of $(5.61 \pm 1.57)\,\%$ and $(5.64 \pm 1.45)\,\%$, respectively. Thus, both quantifications are less accurate than for the experiment with an adiabatic preparation by approximately 4 %. This can also be observed in figure 6.10 by the stronger underestimation. From this figure it can also be depicted, that the new simulation-based approaches are capable of regarding for the imperfect inversion in contrast to the common IR theory. Evaluating the data by this common theory yields a deviation of $(17.42 \pm 3.05)\,\%$.

By minimizing *TR*, the same general observation can be concluded as above. One exception is the behavior of the standard deviation. While the mean deviation $\Delta T_{1,\mathrm{mean}}$ is

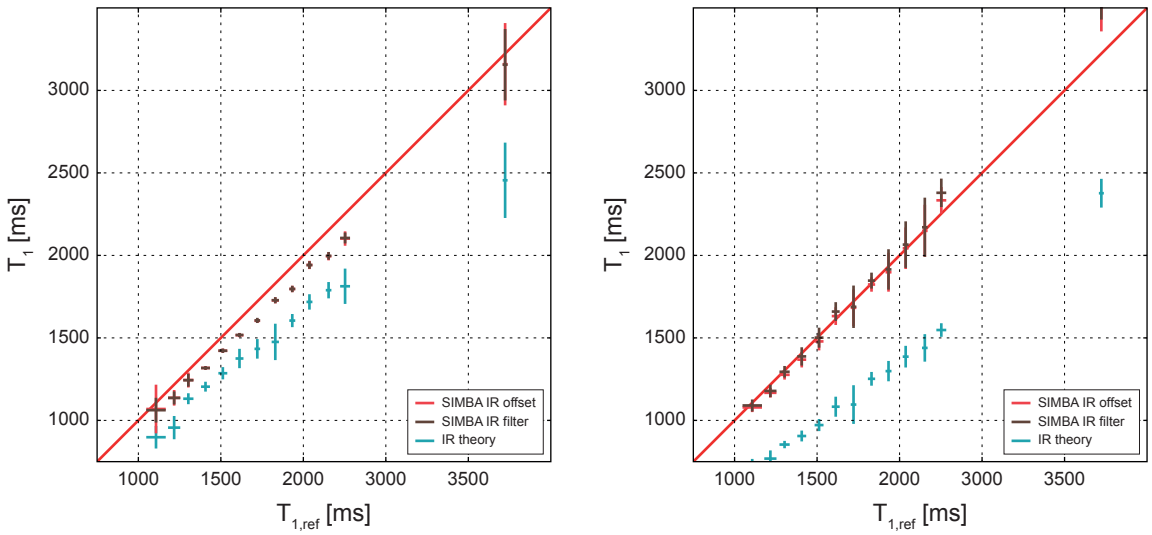

Figure 6.10: T_1 values by the non-adiabatic SIMBA IR method: The repetition time *TR* of the magnetization preparation is varied to correspond to (a) a delay time *TD* of 3000 ms and (b) a *TD* of 0 ms. A FOV with a 256×256×176 px^3 matrix and 1 mm isotropic resolution was acquired at 16 different inversion time *TI* values. The evaluation was performed with a `single-start` optimization based on the `filter` and `offset` signal and the `matched` correction. A red diagonal line represents a perfect correlation between the reference $T_{1,\mathrm{ref}}$ values determined by an IR SE experiment and the T_1 values of the SIMBA IR method (brown markers: `filter` signal, red marker:s `offset` signal) and the evaluation by common IR theory (blue markers). The center and the error bars of each marker correspond to the respective mean values and standard deviations within a ROI for each test tube of the contrast phantom. In comparison with the results of the experiment with an adiabatic preparation (see figure 6.9), the results of this experiment are more inaccurate and less robust. Results of the experiment with a prolonged *TR* feature an increasing systematic deviation with increasing $T_{1,\mathrm{ref}}$ values. With a minimized *TR*, a stronger correlation can be depicted from the mean values but the standard deviation indicates degraded evaluation stability.

reduced by approximately 5 %, the respective $\Delta T_{1,\mathrm{std}}$ value is doubled. This indicates a more unstable performance. Nevertheless, the results of the SIMBA IR experiment with a non-adiabatic preparation are in a good agreement with the reference and the simulation studies above.

The following conclusion about the SIMBA IR experiments can be drawn. A prediction of how the magnetization behaves throughout an magnetic resonance imaging (MRI) experiment and how the signal evolves can be predicted by simulations. The correction hereby is possible and allows for highly accurate quantitative imaging. By reducing the repetition time of the preparation and thus the measurement time, which is a benefit by itself, the accuracy is even further improved due to the higher uniqueness of the signal evolution. The replacement of an adiabatic by a non-adiabatic preparation reduces the SAR exposure and allows for applications previously restricted. All simulation and measurement experiments are in a strong agreement with the gold-standard reference.

Table 6.4: T_1 accuracy by the non-adiabatic SIMBA IR method: Listed are the mean deviations $\Delta T_{1,\text{mean}}$ and the corresponding standard deviations $\Delta T_{1,\text{std}}$ as well as the coefficient of determination R^2 of the quantified longitudinal relaxation times presented in figure 6.10. The main conclusions are: i) With a non-adiabatic preparation, the evaluation accuracy is decreased. ii) As for the adiabatic preparation, a minimization of the repetition time *TR* of the preparation improves the accuracy. However, the evaluation is more unstable.

	TR			min. *TR*		
	original	SIMBA IR		original	SIMBA IR	
		offset	filter		offset	filter
$\Delta T_{1,\text{mean}}$ [%]	17.42	5.61	5.64	33.48	0.20	-1.13
$\Delta T_{1,\text{std}}$ [%]	3.05	1.57	1.45	2.92	3.80	4.27
R^2	0.22	0.96	0.96	-1.01	0.97	0.96

6.2.2 Simulation-Based DESPOT1-HIFI

Within this section, the results of the SIMBA DESPOT1-HIFI experiments are presented. It builds up on the results of the SIMBA IR method. At first, the combinations of the IR and *fast low angle shot* (FLASH) sample points are addressed and the accuracy is evaluated for *in vivo* noise levels. Secondly, the influences of sample point combinations and the pulse class of the preparation on the evaluation accuracy is investigated in phantom measurements presented in section 5.2.2.

Combination Strategies The optimum sampling points of the IR and FLASH experiment are determined within this experiment. This is done to maximize the accuracy and robustness of the novel evaluation technique. The magnetic resonance (MR) signals were calculated for 192 noise datasets with a complex zero mean Gaussian distribution and noise level of 2 %. All evaluations were performed with the `single-start` optimization of both signal simulations (`offset`, `filter`) and the `virtual M` and `matched` correction. A detailed list of the simulation parameters is given in section 5.2.2: Combination Strategies.

Figure 6.11 holds the results for the mean deviation of the longitudinal relaxation time T_1 from the nominal values averaged over all noise datasets. The results for one IR and two FLASH contrasts in shown in figure 6.11(a) and for two IR and two FLASH contrasts in figure 6.11(b). From left to right of each figure, the combination of the inversion times *TI* varies and from top to bottom the combination of readout tip angles α. Data points colored in white show a perfect accordance to the nominal values.

At first figure 6.11(a) will be analyzed. The evaluation accuracy based on the corrections with the `filter` signal is slightly improved; this is in accordance to the experiments of the SIMBA IR method in section 6.2.1. Vertical streaks in α direction and of nearly constant values can be depicted. This indicates that the accuracy is indifferent to the choice of the tip angles. The best evaluation quality exists for a short *TI* value of 500 ms and the two α values of 3 ° and 9 °; 9 ° is the maximum tip angle within the SAR constraints. Mean deviations for T_1 of 2.66 % and 6.26 % can be depicted for the `virtual M` and `matched` correction, respectively. The `matched` approach distinguishes itself by a lower variance of the individual evaluations (not shown within the figure). However, initial measurement not

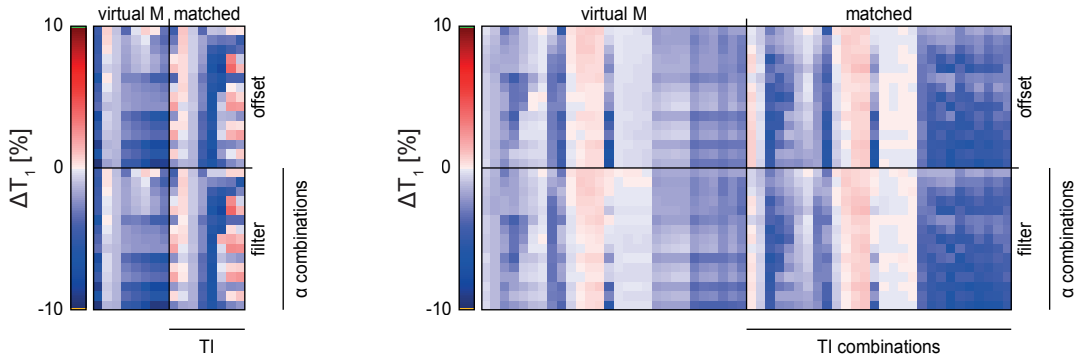

Figure 6.11: Combination strategies of the SIMBA DESPOT1-HIFI experiment: The evaluations were performed for two sets of contrasts with (a) one IR and two FLASH experiments as well as (b) two IR and two FLASH experiments. The evaluation was performed with a `single-start` optimization based on the `filter` and `offset` signal and the `virtual M` and `matched` correction. Presented is the mean deviation $\Delta T_{1,\mathrm{mean}}$ of the longitudinal relaxation time T_1 averaged over the total sample dataset and all 192 noise contributions. The combination of the inversion time *TI* varies from left to right. From top to bottom varies the combination of the angle α values. The main observations are: i) The tip angle only has a weak influence on the evaluation accuracy (nearly constant values along all combinations). ii) The use of only one IR contrast suggests the assignment of a short *TI* value. Yet, this method performs unstable in real measurements. iii) Two IR contrasts that are sufficiently unique and different from the FLASH contrasts stabilize the quantification and improve the accuracy of the method.

presented within this thesis have proven, that the use of only 3 data points perform highly unstable at a magnetic field strength of 7 T. One explanation for this could be the reduced native T_1 contrast of the FLASH technique that has been pointed out in section 2.2.3.

The use of two IR contrasts stabilizes the evaluation for real experimental conditions. Figure 6.11(b) indicates the larger number of possible *TI* combinations. Moreover, the accuracy is mainly attributed by the choice of the *TI* sample points and not by the FLASH readout tip angles. A distinct optimum exists for the *TI* combinations of 750 ms and 1500 ms as well as 750 ms and 1750 ms. The first inversion time must be long enough for the signal of different tissues to evolve a contrast, and the second must be sufficiently prolonged to create a dissimilar signal evolution to the first and to the FLASH contrasts. Again, the precision is the highest for the FLASH readout tip angles of 3 ° and 9 °. The respective accuracies of the two *TI* combination account to -0.71 % and -0.01 % for the matched correction, respectively. From this and the previous experiments the matched correction has proven to be the most stable approach.

The main consequences of this experiment are: Using only one IR contrast yields an unstable performance in real MRI experiments. The use of two IR contrasts improves this circumstance and needs to be validated in phantom measurements. It does not make a difference whether the preparation is performed by an adiabatic or a non-adiabatic preparation; the optimum sample points defining the respective contrasts are identical.

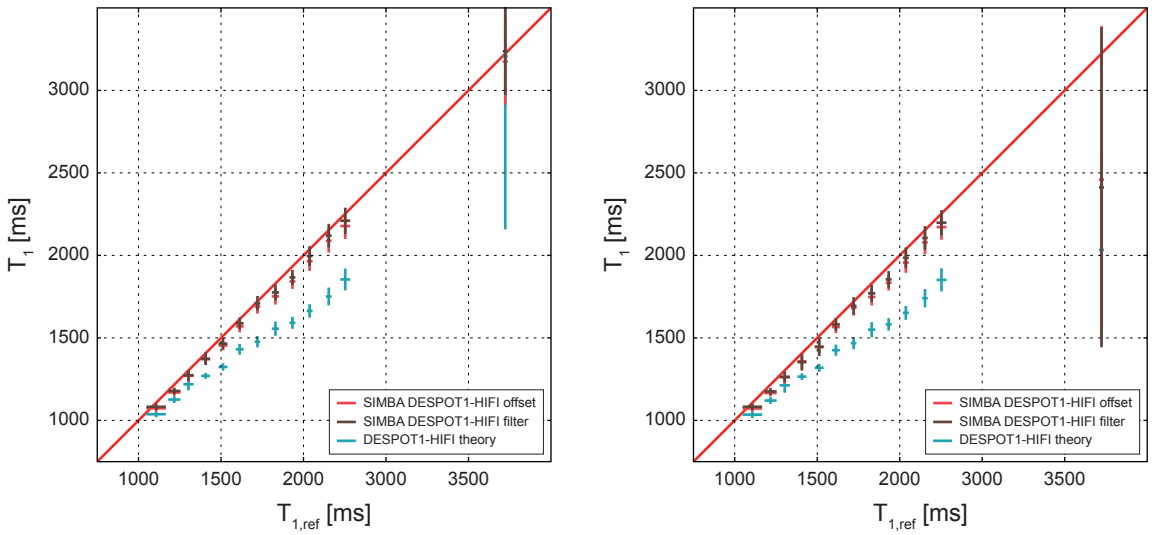

Figure 6.12: T_1 values by the adiabatic SIMBA DESPOT1-HIFI method: The IR experiment was performed for two set of inversion time *TI* values of (a) 750 ms and 1500 ms as well as (b) 750 ms and 1750 ms. The FLASH experiment was performed for the two tip angle α values of 3 ° and 9 °. A FOV with a 256×256×176 px^3 matrix and 1 mm isotropic resolution was acquired within a total measurement time of less than 30 min. The evaluation was performed with a `single-start` optimization based on the `filter` and `offset` signal and the `matched` correction. A red diagonal line represents a perfect correlation between the reference $T_{1,\mathrm{ref}}$ values determined by an IR SE experiment and the T_1 values of the SIMBA DESPOT1-HIFI method (brown markers: `filter` signal, red marker:s `offset` signal) and the evaluation by original DESPOT1-HIFI theory (blue markers). The center and the error bars of each marker correspond to the respective mean values and standard deviations within a ROI for each test tube of the contrast phantom. The T_1 values quantified with the SIMBA DESPOT1-HIFI method reveal a strong correlation with the reference values. All T_1 values are slightly overestimated though. The original DESPOT1-HIFI method yields results with a strong deviation from the reference. The accuracy and robustness of the new method is nearly identical for both sets of *TI* timings. The evaluation of the longest T_1 sample fails for all approaches.

Measurements This experiment tests the performance of the SIMBA DESPOT1-HIFI method with the optimum IR and FLASH contrasts from above in a phantom study. The experimental setup is described in section 5.2.2.

The correlation diagram in figure 6.12 opposes the quantified values of the longitudinal relaxation time by the new methods T_1 to the references $T_{1,\mathrm{ref}}$ determined with an IR SE experiment (see section 3.1.4). The red diagonal indicates a perfect correlation. Each brown (`filter` signal), red (`offset` signal), and blue (DESPOT1 with high-speed incorporation of RF field inhomogeneities (DESPOT1-HIFI) theory) marker corresponds to the mean T_1 value of a ROI within each test tube and the whisker to the corresponding standard deviations. Figure 6.12(a) holds the results for *TI* sample points of 750 ms and 1500 ms. The results for *TI* sample points with values of 750 ms and 1750 ms are presented in figure 6.12(b).

The results show a strong correlation with the reference values. All T_1 values are underestimated with a constant offset. Evaluations based on the `filter` signal are more

Table 6.5: T_1 accuracy by the adiabatic SIMBA DESPOT1-HIFI method: Listed are the mean deviations $\Delta T_{1,\text{mean}}$ and the corresponding standard deviations $\Delta T_{1,\text{std}}$ as well as the coefficient of determination R^2 of the quantified longitudinal relaxation times presented in figure 6.12. The following conclusions can be drawn: i) The accuracy is nearly identical for all the presented simulation-based evaluation strategies. ii) The original DESPOT1-HIFI method yields T_1 deviation larger than 10 %.

	$TI = 750/1500\,\text{ms}$			$TI = 750/1750\,\text{ms}$		
	original	SIMBA DESPOT1-HIFI		original	SIMBA DESPOT1-HIFI	
		offset	filter		offset	filter
$\Delta T_{1,\text{mean}}$ [%]	12.94	3.26	2.26	13.33	3.69	2.90
$\Delta T_{1,\text{std}}$ [%]	4.69	0.84	0.82	4.72	0.79	0.89
R^2	-0.16	0.97	0.99	-0.23	0.96	0.98

accurate than those based on the `offset` signal. The respective standard deviations increase for long $T_{1,\text{ref}}$ values. For the test tube of the longest T_1 the quantification of the longitudinal relaxation time fails; this is indicated by the large standard deviations. The DESPOT1-HIFI method (blue markers) holds a systematic deviations from the reference values that increase for long $T_{1,\text{ref}}$ values. This can be explained for the imperfect relaxation of samples with long T_1 values prior to the next preparations. Both TI sample point distributions perform nearly identical within T_1 range of 1100 ms and 3300 ms.

The statistics of this experiment is summarized in table 6.5. Listed are the mean deviation $\Delta T_{1,\text{mean}}$ of the quantified from the reference values of the longitudinal relaxation time T_1 and the respective standard deviation $\Delta T_{1,\text{std}}$. Furthermore, the coefficient of determination R^2 is shown.

Evaluations based on the `filter` signal show a higher accuracy than for the evaluations based on the `offset` signal. The mean deviation for this method varies between (2.26 ± 0.82) % and (3.69 ± 0.79) % for the two different TI sampling points distribution, respectively. The highest accuracy is achieved with the TI sampling points of 750 ms and 1500 ms with a corresponding R^2 of 0.99.

The originally published DESPOT1-HIFI method quantifies T_1 with a systematic deviation of more than 10 %. Due to the shift of the mean values does R^2 reveal negative values and has no reasonable meaning. The determination of prolonged longitudinal relaxation times, as encountered at a magnetic field strength of 7 T, is a limitation of this approach.

In section 6.2.1 the effect of a minimization of the repetition time TR of the magnetization is shown. For this reason, the TI sample points of 1251 ms and 3114 with minimized TR values were alternatively depicted. The total measurement time is nearly unaffected by this modification. Furthermore, the experiment was performed with an adiabatic and a non-adiabatic preparation of the magnetization.

The results are presented in a correlation diagram of the same concept as above in figure 6.13 and the corresponding table 6.6.

The results for the experiment with an adiabatic preparation are in a good agreement with the experiment above. All T_1 values are still underestimated although the deviation to

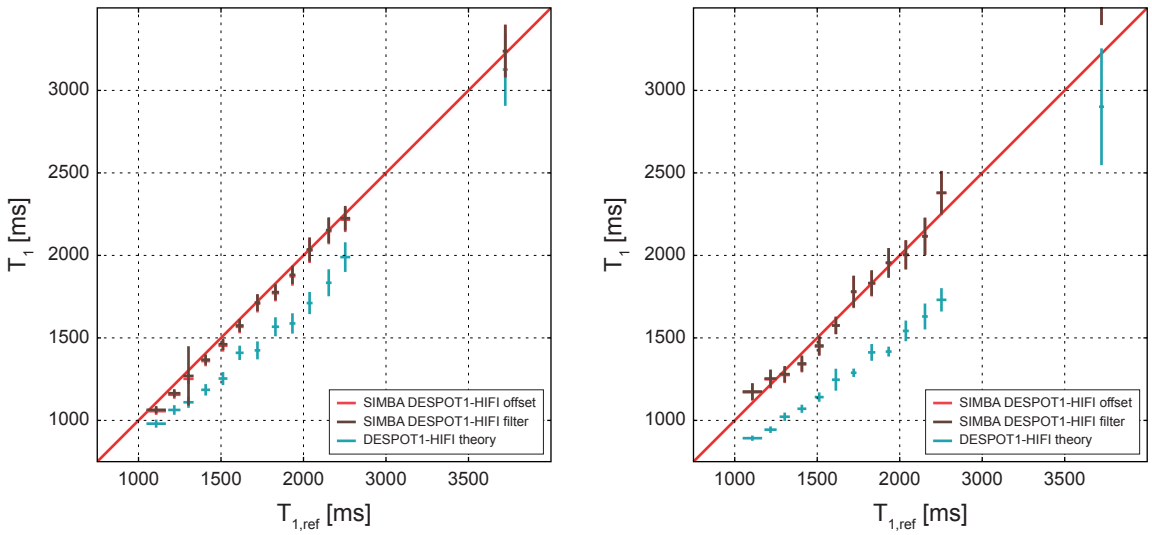

Figure 6.13: T_1 values by the SIMBA DESPOT1-HIFI method and minimized *TR*: The magnetization preparation was performed by (a) an adiabatic HS and (b) a non-adiabatic rectangular RF pulse. The IR experiment was performed for the two inversion time *TI* values of 1251 ms and 3114 ms. The FLASH experiment was performed for the two tip angle α values of 3 ° and 9 °. A FOV with a 256×256×176 px^3 matrix and 1 mm isotropic resolution was acquired within a total measurement time of less than 30 min. The evaluation was performed with a `single-start` optimization based on the `filter` and `offset` signal and the `matched` correction. A red diagonal line represents a perfect correlation between the reference $T_{1,\text{ref}}$ values determined by an IR SE experiment and the T_1 values of the SIMBA DESPOT1-HIFI method (brown markers: `filter` signal, red marker:s `offset` signal) and the evaluation by original DESPOT1-HIFI theory (blue markers). The center and the error bars of each marker correspond to the respective mean values and standard deviations within a ROI for each test tube of the contrast phantom. As for the SIMBA IR method, does a minimization of *TR* lead to high higher evaluation quality. With such long *TI* sampling points, the evaluation failure of the longest $T_{1,\text{ref}}$ sample is resolved. The results for the non-adiabatic experiment scatter across the correlation diagonal and show a larger standard deviations. Evaluations by the original DESPOT1-HIFI method show a larger systematic underestimation of all $T_{1,\text{ref}}$ values.

the reference is decreased. The difference in the quantification accuracy of the `filter` and `offset` signal-based quantification is degraded. The standard deviations do not feature the systematic dependencies as before and are rather statistically distributed. Evaluations by the original DESPOT1-HIFI still show a strong deviation from the reference values. However, with the long *TI* sampling point of 3144 ms the longest T_1 value is determined correctly by the new simulation-based methods. Overall, the mean deviations accounts to (2.26 ± 0.82) % and thus is more precise than for the measurements with a prolonged *TR*.

With a non-adiabatic preparation the results show a different behavior. The quantified T_1 values scatter around the correlation diagonal. All respective standard deviations indicate a distinct variance of the value and thus a more unstable evaluation. A mean deviation of (2.90 ± 0.89) % was determined. The degraded evaluation quality is a result of the reduced contrast of the magnetization samples (see section 6.2.1). The original DESPOT1-HIFI method cannot handle a non-perfect inversion and reveals a deviation of more than 10 %.

Table 6.6: T_1 accuracy by the SIMBA DESPOT1-HIFI method and minimized *TR*: Listed are the mean deviations $\Delta T_{1,\text{mean}}$ and the corresponding standard deviations $\Delta T_{1,\text{std}}$ as well as the coefficient of determination R^2 of the quantified longitudinal relaxation times presented in figure 6.13. The following conclusions can be drawn: i) The mean deviation decreases for a non-adiabatic preparation, the respective standard deviations increase though. This indicates a more unstable evaluation performance. ii) Evaluations based on either signal simulation hold nearly the same quantification quality.

	adiabatic preparation			non-adiabatic preparation		
	original	SIMBA DESPOT1-HIFI		original	SIMBA DESPOT1-HIFI	
		offset	filter		offset	filter
$\Delta T_{1,\text{mean}}$ [%]	13.79	2.51	1.99	23.41	-0.12	-0.32
$\Delta T_{1,\text{std}}$ [%]	3.87	1.80	1.58	1.86	3.56	3.56
R^2	0.79	0.99	1.00	-1.43	0.98	0.98

The following conclusions can be drawn for the new SIMBA DESPOT1-HIFI method. For the method to perform accurate and robust, two IR and two FLASH contrasts must be involved. The accuracy of the method is strongly impacted by the *TI* sample points. Within a total measurement time of less than 30 ms, a matrix of $256\times256\times176\,\text{px}^3$ can be acquired.

6.2.3 Simulation-Based DESPOT1-HIFI *in vivo*

This section holds the initial results of the SIMBA DESPOT1-HIFI *in vivo* experiments. Two different regions of the human body have been examined. At first the quantitative maps of the longitudinal relaxation of a human brain are presented. Secondly, the application of the method as well as the respective quantification on a human calf muscle is shown.

Whole Brain The whole brain was covered within a FOV of $256\times256\times176\,\text{mm}^3$ of 1 mm isotropic resolution. Two adiabatic IR contrasts with the inversion times of 1251 ms and 3114 ms as well as two FLASH contrasts with nominal tip angles of 3 ° and 9 ° were acquired within a total measurement time of 28:57 min. The computation time of the evaluation of one slice accounts to approximately 10 min. For more information see the respective experiment description in section 5.2.3: Whole Brain.

Figure 6.14 shows the acquired native image data for the quantification method and the reference scans of the static magnetic and RF field inhomogeneities. At first, an exemplary transverse slice of the head for the two IR and the two FLASH contrasts is pictured in the figure 6.14(a). The skin and the subcutaneous fat appear hyperintense in all images, the skull hypointense. A thin layer of CSF surrounds the cortex which consists of gray matter. Most of the brain is made up of white matter. Two ventricles (red arrow) are located in the center and are filled with CSF. The contrast of gray and white matter changes with the inversion time *TI* in IR experiments and with the tip angle α in FLASH sequences. All images are equally windowed so that the signal values can be interpreted in a direct correlation.

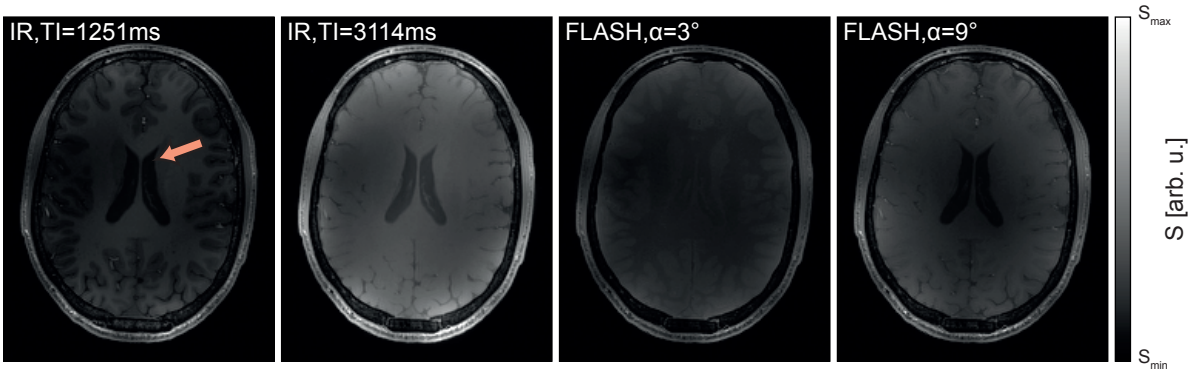

(a)

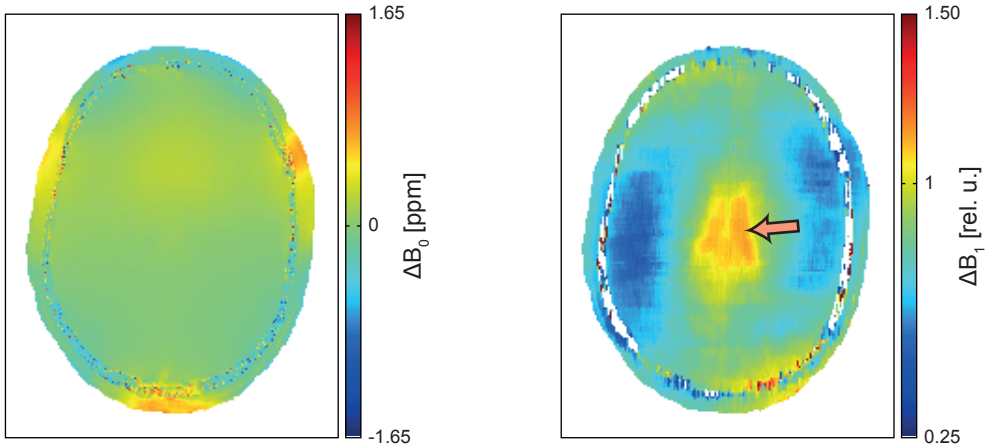

(b) (c)

Figure 6.14: Images of a human head: (a) Two IR and two FLASH contrasts as well as (b) the maps of the static magnetic ΔB_0 and (c) the RF field inhomogeneity ΔB_1 are shown. Red arrows mark the position of the CSF filled ventricles. The contrast of the gray and white brain matter changes with the inversion time TI in IR and the tip angle α in FLASH experiments. Both, the static magnetic and the RF field distribution agree with the expected behavior as described in section 6.1.1.

A field map of the static magnetic field ΔB_0 is presented in figure 6.14(b) as a deviation from the nominal field strength in units of parts per million. For a detailed analysis of the field inhomogeneity see section 6.1.1. The reference map shows, that the field distribution lies within the dynamic range identified in section 6.1.1 and regarded for by the simulations. The same accounts for the relative scaling map of the RF field ΔB_1 in figure 6.14(c). Regions of a low tip angle are present to the left and right side of the brain. The central brightening effect can also be depicted, as already described in section 6.1.2.

The results of the SIMBA DESPOT1-HIFI evaluation are shown in figure 6.15. From left to right, one coronal, sagittal, and transverse plane is presented for the quantified magnetization M_0, longitudinal relaxation time T_1, and tip angle scaling factor κ.

The magnetization in figure 6.15 features distinct hyperintense values (white arrows) near the surface of the brain. This is due to the bias of the receive field of the RF coil, and the effect depletes towards the center of the brain. The ventricles (red arrows) show up brighter than the white matter because of the higher proton density of the CSF. In the region of the nasal and oral cavities as well as the temporal bone (black arrows), the determination of M_0 fails due to the poor signal to noise ratio (SNR).

The tip angle scaling factor κ indicates clearly that the transmit field of the RF coil is isolated from the receive field. The maps with all respective κ values are in a strong agreement with the reference scan shown in figure 6.14(c). Towards the center, the quantified field amplitude appears to be of a lower value in comparison to the reference. The position as well as the slice thickness, 1 mm for the SIMBA DESPOT1-HIFI method and 3 mm for the reference scan, of the two methods differ slightly though. Additionally, the reference maps reveal anatomical structure such as the ventricles (red arrow) with an increased κ value. On the lower left side of the coronal view, the estimation of κ fails (black arrow) as the field amplitude drops and the SNR is not sufficient.

The main target of the experiment was the generation of T_1 maps. The longitudinal relaxation time values feature very little noise. Gray and white matter can be easily differentiated. The values for the CSF clip in the displayed color map and must not be misinterpreted as being smoothly distributed. In fact, the evaluation of the CSF signal fails as it has for the pure water in the respective phantom measurements (see section 6.2.2). At the position at which the quantification of M_0 and κ fails, T_1 is also determined incorrectly (black arrow on the lower left side of the coronal view). The cerebellum, shown on the lower right side of the sagittal view, holds the correct values for the longitudinal relaxation time even though the RF field amplitude has dropped by 50 %. Figure 6.16 holds 16 out of the 256 transverse slices of the T_1 maps of the same measurement. Averaged over the whole brain and with the respective standard deviations, the longitudinal relaxation times for the gray and white matter come out to (1916.51±95.20) ms and (1245.74±55.84) ms, respectively. The accuracies of these results are discussed in section 7.4.2.

Calf Muscle A human calf muscle of the left leg was examined with the same imaging protocol as initially set up for the head; this spared computational burden for the creation of new correction libraries. Again, two IR contrasts with inversion times of 1251 ms and 3114 ms and two FLASH contrasts with nominal tip angles of 3 ° and 9 ° were acquired in a total measurement time of 28:55 min. This time though, the IR experiments were prepared by a non-adiabatic pulse. The complete experiment is described in section 5.2.3:

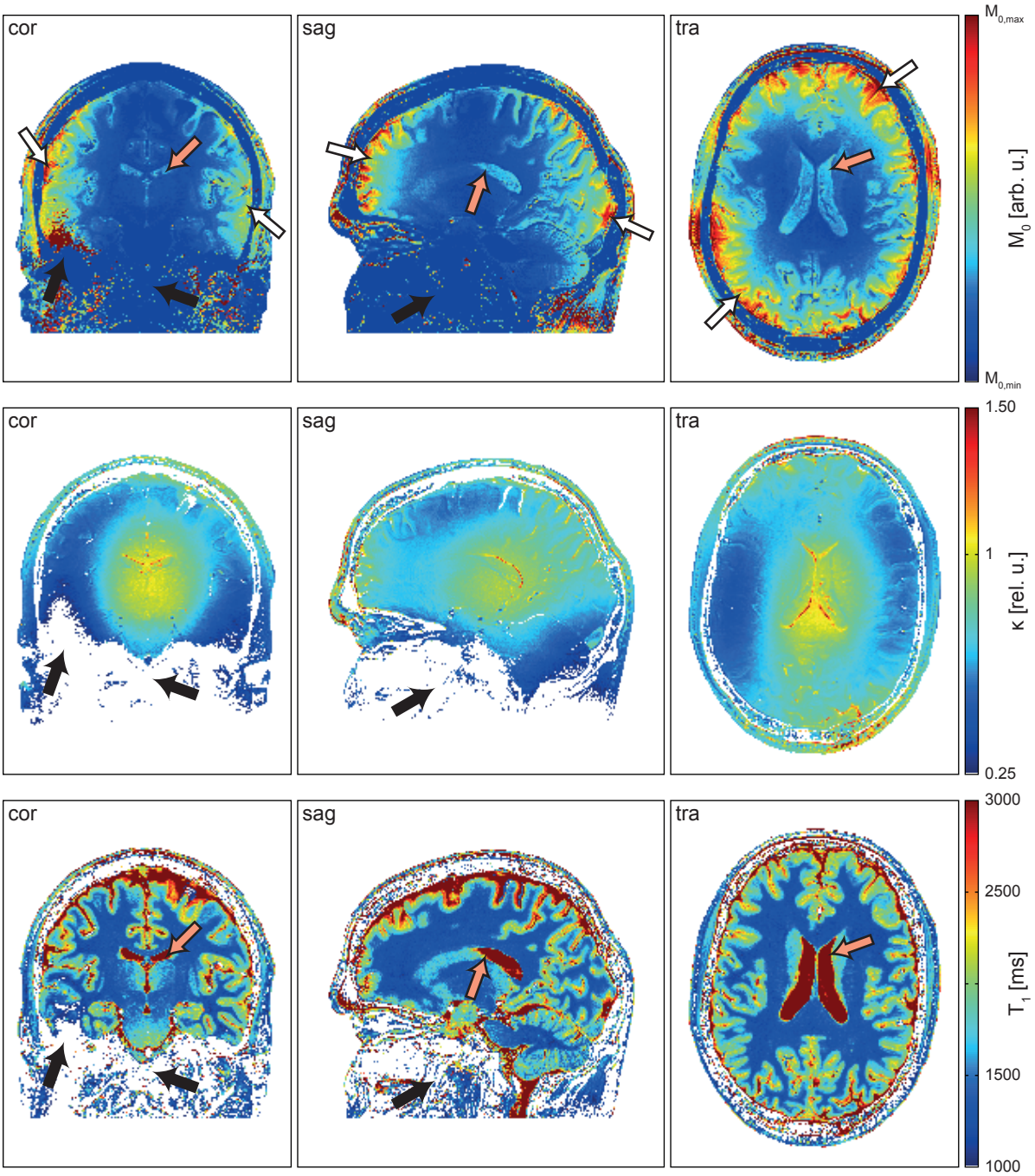

Figure 6.15: T_1 maps of the whole brain by the adiabatic SIMBA DESPOT1-HIFI method: From left to right, one coronal, sagittal, and transverse view of the magnetization M_0, the tip angle scaling factor κ, and the longitudinal relaxation time T_1 is illustrated. The FOV is 256×256×176 mm large with a 1 mm isotropic resolution and was acquired in 28:57 min. The ventricles are marked by red arrows. White and black arrows point out regions of an increased receive sensitivity of the coil and a reduced transmit field amplitude, respectively. M_0 is impacted by the bias of the receive field; only the CSF in the ventricles shows a proton density contrast. The tip angle map is in a strong agreement to the reference scan. The T_1 values in the gray and white matter show little noise and are accurate even at low RF field amplitudes in the cerebellum. Only the right temporal lobe (left side of the coronal view) features a small number of failed evaluations (black arrow).

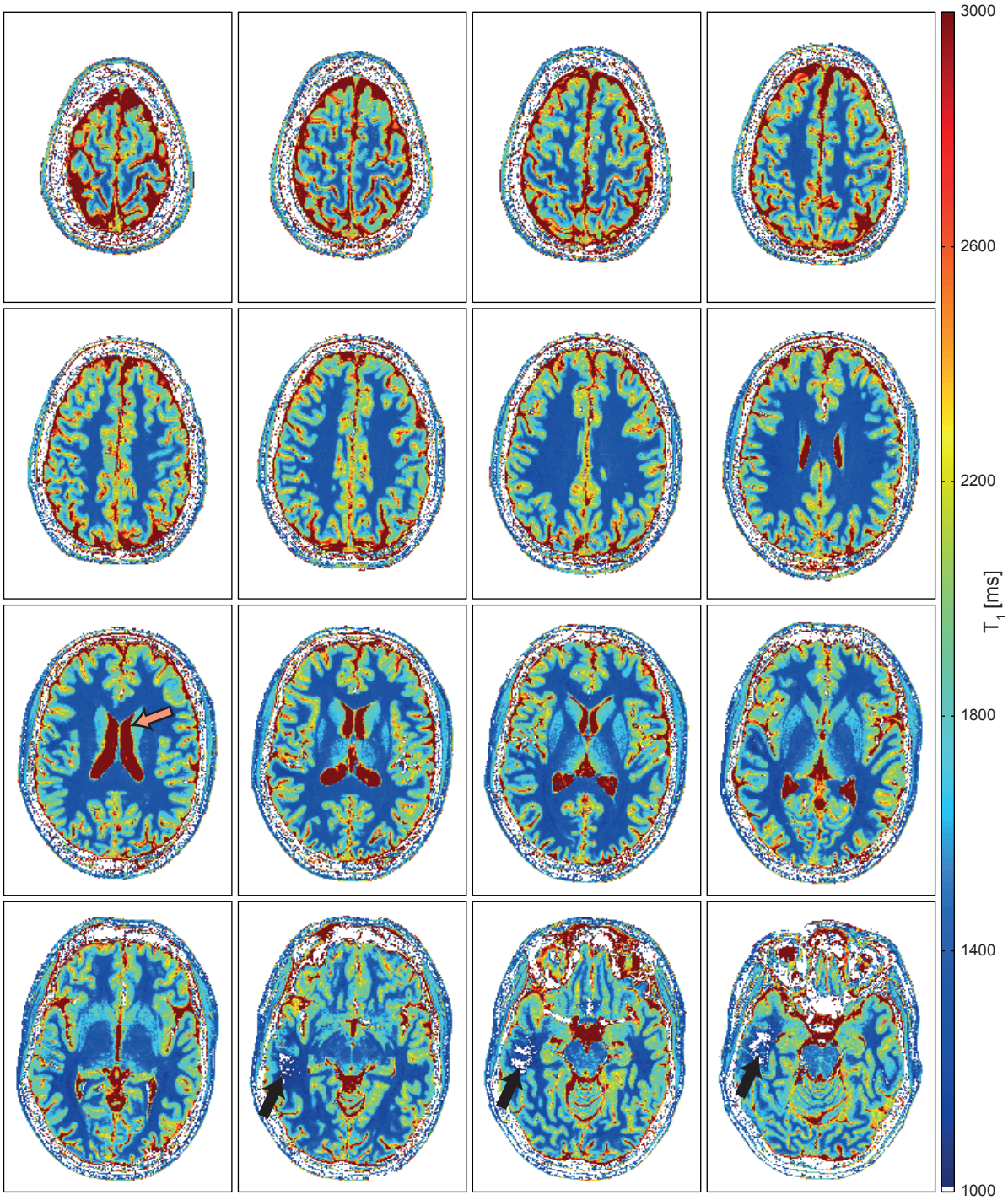

Figure 6.16: T_1 mosaic of the whole brain by the adiabatic SIMBA DESPOT1-HIFI method: 16 out of 256 transverse slices of the T_1 maps. A red arrow marks the position of the CSF filled ventricles. T_1 values are smoothly distributed across the whole brain in all slices. The gray and the white matter can be clearly differentiated. The evaluation fails only at very low RF field amplitudes. This is the case in the right temporal lobe shown on the left side of the image in the last 3 slices (black arrows).

Calf Muscle. All results are presented in the same manner as for the investigation of the brain.

The four imaging contrasts are shown by an exemplary transverse slice in figure 6.17(a). All general dependencies on the inversion time TI for the IR and on the tip angle α for the FLASH experiments apply as described before. Arrows mark the shinbone (blue) and the fibula (yellow). The bone structure itself can be depicted by its hypointense signal. The bone marrow is a fatty tissue and does hold a signal as well as the subcutaneous fat surrounding the calf muscle. On the upper right side of the slices, a strong hyperintense signal is apparent (white arrow). The IR contrasts do also feature the central brightening effect.

The distribution of the static magnetic field ΔB_0 is illustrated in figure 6.17(b). Blue and yellow arrows still mark the same anatomical structures. Variations of ΔB_0 are nearly constant over the whole muscle and do not show such a strong inhomogeneity as for the head. The signal of the subcutaneous fat and the bone marrow appears to be off-resonant by approximately 0.5 ppm. The protocol is set in such a way, that the fat signals of both contrasts are supposed to be in phase, thus appearing on-resonant. If the chemical shift of the fat does not equal the reference value of 3.4 ppm, the determined ΔB_0 value will be biased. Since this is not the case in the measurement, the off-resonance of the fat surrounding the calf muscle must be different chemical shift than the reference value of the MR system. Another proof of the strong off-resonance of fat is indirectly given by the map of the RF field in figure 6.17(c). Overall, the relative deviation from the nominal tip angle ΔB_1 is stronger than for the head. In the center of the muscle, ΔB_1 reaches a value of 2.25 while it drops to 0.5 in the outer regions. This is a feature of the 28-channel Siemens knee coil described in section 3.1.2. The B_1 method fails for the fatty tissues. The reason for this is given by the frequency response of the preparation pulse of the sequence. A rectangular pulse with a duration of 1 ms does not manipulate the fat with the desired effect. To overcome this limitation, either can the pulse duration be further reduced to offer a broader frequency response, or the transmission frequency can be centered on the fat resonance frequency.

The performance of the non-adiabatic SIMBA DESPOT1-HIFI method is presented in figure 6.18. Reading the figure from left to right, a coronal, sagittal, and transverse slice of the calf is shown. From top to bottom, the apparent magnetization M_0, the longitudinal relaxation time T_1, and the tip angle scaling factor κ are presented. The shine bone and the fibula are again marked by blue and yellow arrows, respectively.

The quantified magnetization M_0 in figure 6.18 also features the inhomogeneous receive field characteristics. This is indicated by the white arrows in the coronal and transverse plane. Additionally, the receive field is limited by the coil geometry in head-feet direction and the signal drops to a low SNR values (black arrows). The central brightening effect of the transmit field is fully corrected for.

The tip angle variation κ throughout the calf is also shown in figure 6.18. Again, the quantification by the simulation-based approach is in a strong agreement with the reference scan in figure 6.17(c). It is striking, that the field is smoothly distributed even for fatty tissues, although it is known from the M_0 map that the evaluation fails in these regions. Red arrows mark a phenomenon that will be interpreted for the evaluation of the T_1 maps.

The results of the quantification of the longitudinal relaxation time are presented in the

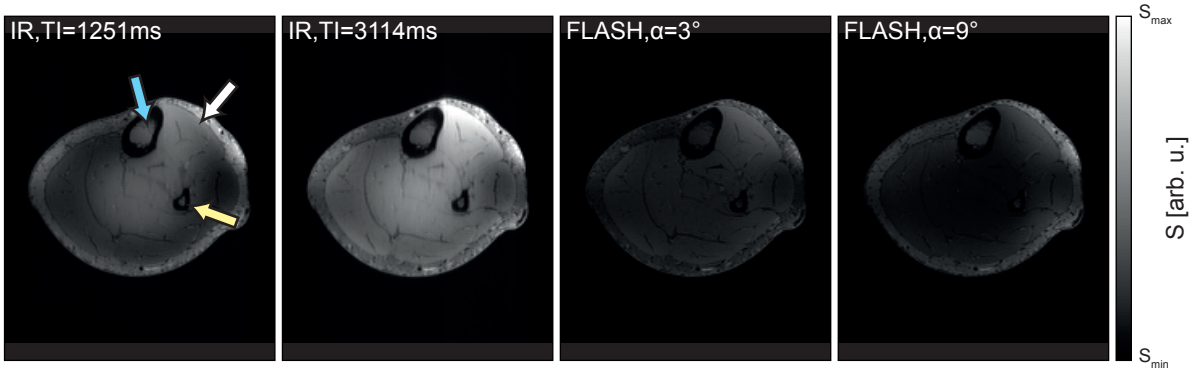

(a)

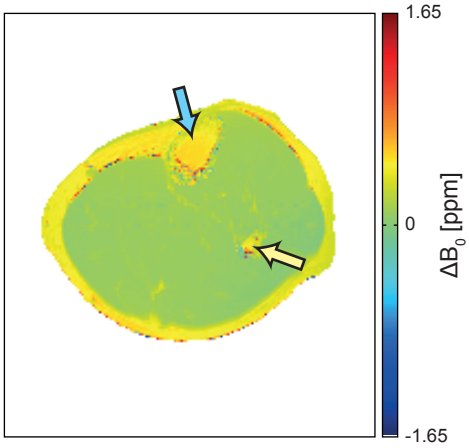

(b)

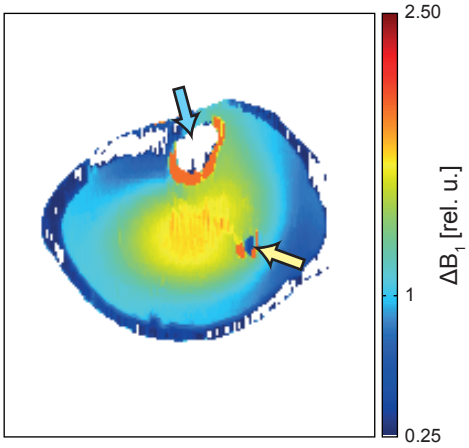

(c)

Figure 6.17: Images of a human calf: (a) Two IR and two FLASH contrasts as well as (b) the maps of the static magnetic ΔB_0 and (c) the RF field inhomogeneity ΔB_1 are presented. Blue arrows mark the position of the shine bone and yellow arrows the position of the fibula. The signal amplitudes are biased by the transmit and receive field of the RF coil. This is shown by the central contrast deviations and the hyperintense signal values marked by the white arrow. The static magnetic field map shows a smooth distribution of the ΔB_0 values. Fatty tissues appear to be off-resonant by 0.5 ppm compared to the common literature value of 3.4 ppm. The B_1 field map shows a strong inhomogeneity and a region of significantly increased values in the center. Fatty tissue does not hold the desired effect of the preparation pulse on the magnetization and cannot be quantified.

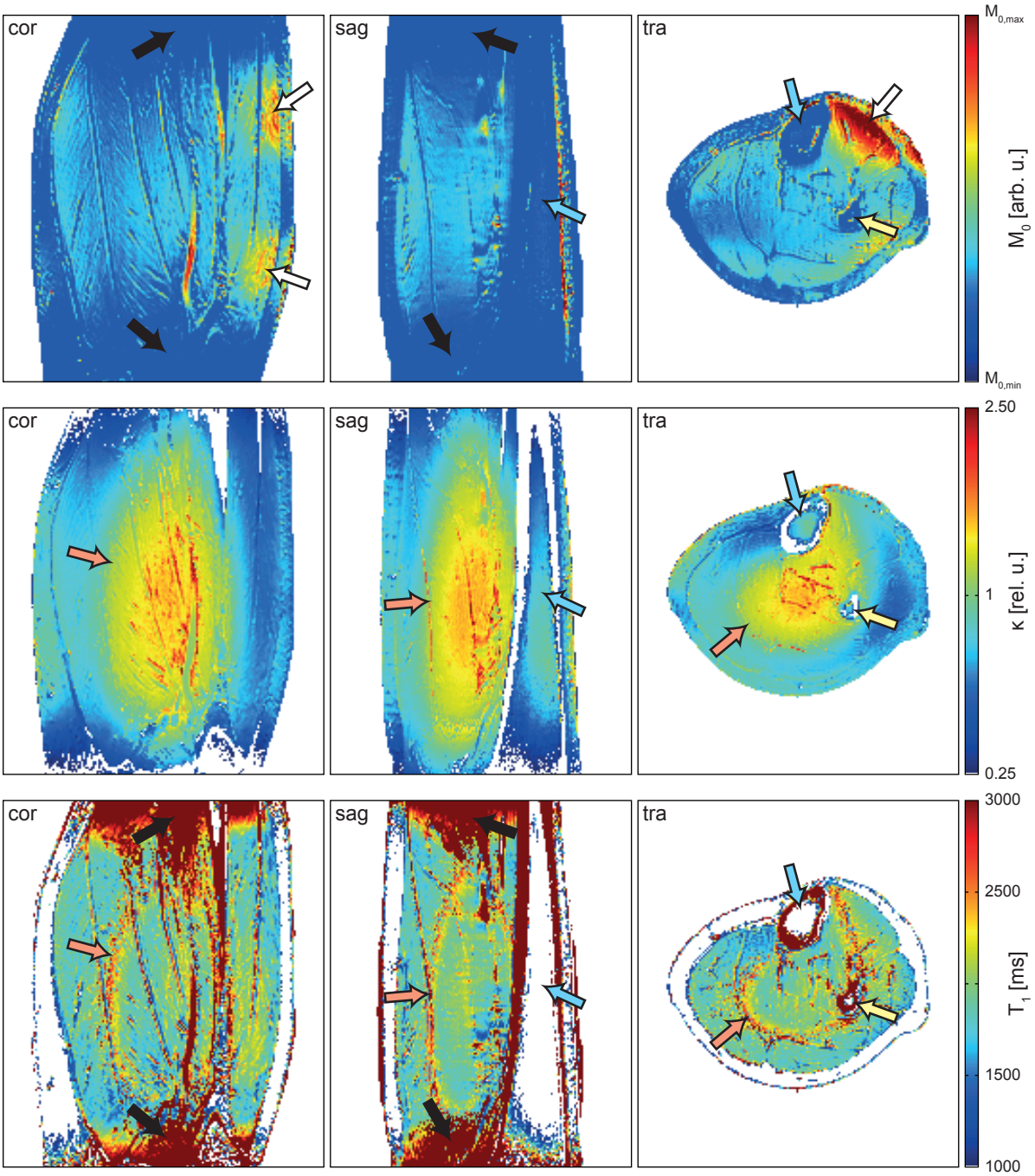

Figure 6.18: T_1 quantification of the calf muscle by the non-adiabatic SIMBA DESPOT1-HIFI method: From left to right, one coronal, sagittal, and transverse view of the magnetization M_0, the tip angle scaling factor κ, and the longitudinal relaxation time T_1 is shown. The FOV is 256×256×176 mm large with a 1 mm isotropic resolution and was acquired in 28:55 min. Blue arrows mark the position of the shine bone and yellow arrows the position of the fibula. White and black arrows point out regions of an increased receive sensitivity of the coil and a reduced transmit field amplitude, respectively. M_0 is impacted by the bias of the receive field. The tip angle map is in a strong agreement with the reference scan. The quantification of the parameters fails for fatty tissues. The organization of muscle strands in the head-feet direction is indicated by a hard change in T_1 values. The red arrows mark an evaluation inaccuracy in a distinct κ value range.

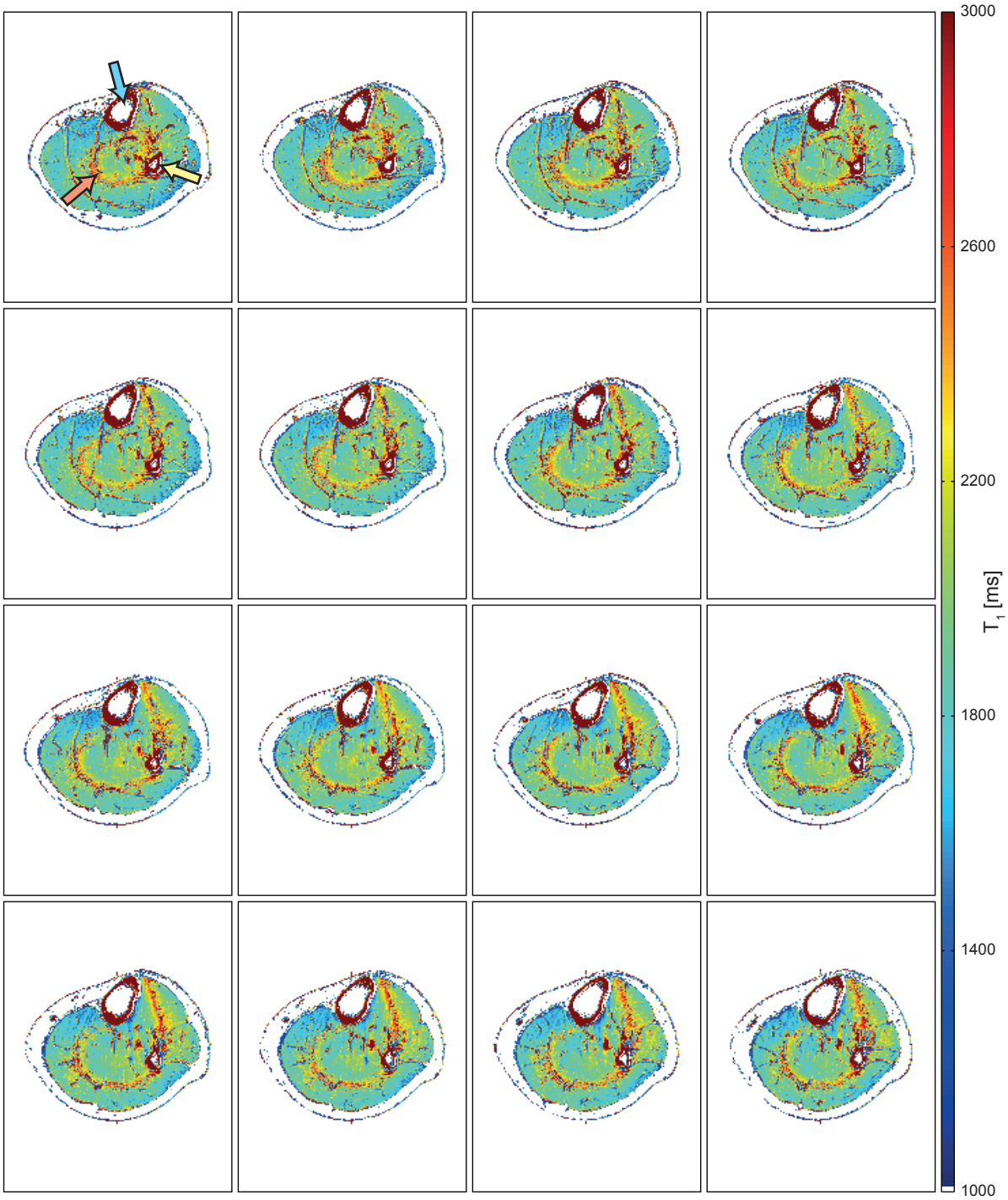

Figure 6.19: T_1 mosaic of the calf muscle by the non-adiabatic SIMBA DESPOT1-HIFI method: 16 out of 256 transverse slices of the T_1 maps. Blue arrows mark the position of the shine bone and yellow arrows the position of the fibula. Overall, the T_1 values are smoothly distributed over the whole calf muscle. A T_1 bias exists only in regions of low RF amplitude. Marked by the red arrows is an artifact that shows up as overestimated T_1 values.

bottom row of figure 6.18. At first, it must be pointed out that the evaluation fails in the region of low SNR (black arrows). Overall, the T_1 value distribution comes out smoothly, but a few details must be addressed. Anatomical structures, such as the organization of individual muscle strand in head-feet direction, can be depicted by a hard change in T_1 values in the coronal and sagittal view. The transverse view also shows a slight bias in the regions of low B_1 amplitude (see figure 6.18). Marked by the red arrows is an artifact that shows up as overestimated T_1 values. Its shape corresponds to a distinct κ value range and thus, follows the RF transmit field distribution. It can be observed in all three orientations. One possible cause of this is discussed in section 7.4.2. Figure 6.19 shows 16 out of 256 transverse slices of the whole imaged volume. The longitudinal relaxation time in the human calf muscle can be quantified to (1876.91±92.23) ms and will be compared to literature values in section 7.4.2.

7 Discussion

The main objective of this thesis was the development of a technique to quantify the longitudinal relaxation times by magnetic resonance imaging (MRI) at ultra high field (UHF). A stronger magnetic field strength improves the signal to noise ratio (SNR) and allows for faster and higher resolved imaging. However, along with the signal increase come the issues of spatial variations of the static magnetic and the radio frequency (RF) field. As the imaging process is prone to the local inhomogeneity of the field distributions, the desired signal evolution of transient states deviates from the values predicted by theory. Furthermore, the readout in fast MRI also impacts the contrast generation and thus, the evaluation. To overcome these limits, the novel quantification technique presented in this thesis has been designed, which simulates and regards these effects for any tissue type in a range of varying local conditions [Breithaupt et al., 2014].

At first, the spatial variations of the magnetic fields have to be determined using sample reference measurements. Once available, a simulation of the magnetization vectors for the tissues of interest with all the respective physical parameters and all the appearing local conditions is to be performed. This is done for all the involved sequences of the experiment and the corresponding parameter protocols. Correction libraries are calculated from these simulations. All the steps mentioned above only need to be carried out once. The correction libraries can be applied as long as neither the local conditions change, e. g. by the utilization of different RF coils or by significantly different loads, nor the tissue of interest does, i. e. the appropriate physical parameters. Next, the measurement is executed with the same sequences and protocols as for the simulation. Finally, the evaluation is performed. The measured data is matched to the respective theory in an iterative manner. On the one hand, the quantified physical parameters rely on the signal values, which themselves are affected by the imaging process. On the other hand, the correction is associated to the physical parameters. This double dependency is resolved when the optimization minimizes the target function. The result is a set of fully corrected quantitative parameter maps.

Three main steps of the described method are discussed within this section to give a more thorough understanding. At first the quantification of the parameter uncertainties of the static magnetic and the RF field is addressed in section 7.1. This is followed by the classification of the simulation framework and its performance in section 7.2. In section 7.3 the simulation-based evaluation strategies are investigated in detail. At last, section 7.4 deals with the comparison of the quantified values of the longitudinal relaxation time for phantom and *in vivo* measurements.

7.1 Parameter Uncertainties

Variations of the static magnetic and the RF field strength impact the effect of an MRI sequence element on the magnetization. This has been covered in the physical background in section 2.2.1 about the RF pulses. The influence of the two is different though and also manifests for conventional and adiabatic pulses in a likewise unique manner. In section 7.1.1, the consequences of the inhomogeneity of the static magnetic field are discussed. The same is done for the inhomogeneity of the RF field in section 7.1.2.

7.1.1 Static Magnetic Field Inhomogeneity

The static magnetic field in high field and UHF magnetic resonance (MR) systems is generated by an electrical current passing through a superconducting wire in a loop. Liquid helium cools the system down to a few kelvins only. By today, the magnetic field strength has been increased to values as high as 7 T and above. More than 40 UHF systems are installed and operated worldwide [Kraff et al., 2015]. The intrinsic homogeneity of such a system is difficult to handle and new magnet designs are still under investigations [Robitaille and Berliner, 2006]. Variations of the field strength are compensated by the shim coils to a certain degree, but a remaining variance for Siemens systems has been specified in the range of a few parts per million [oral communication with manufacturer].

Another influence results from the magnetizability of the sample material and the respective susceptibility. Even for an ideal magnet does the inhomogeneity scale with the change of the susceptibility of adjacent materials and the absolute field strength; see equation 2.69. This spatial fluctuation is on a scale of or even below the pixel dimensions. With higher order shimming, it has been reduced [Gruetter, 1993; Shen et al., 1997] and more advanced approaches are still an ongoing field of research [Wilson et al., 2002]. Shimming is especially important and demanding for small objects [Robitaille and Berliner, 2006].

The results for the quantification of the static magnetic field in the human brain were presented in section 6.1.1 in detail. It can be recalled, that the maps showed a smooth distribution of the local field strength. A drop could be identified into feet direction with increasing distance to the magnetic isocenter of the MR system. This is due to the magnet itself. The field lines diverge at each end of the cylindrical structure. First effects already occur within a few decimeter distance from the center. Another more severe disturbance of the magnetic field exists in the proximity of the nasal cavities. Here, it is caused by the change of the susceptibility of the air and brain tissue and comes out to more than 1.65 ppm. Overall, 90 % of the variations of the static magnetic field range from -0.46 ppm to 0.42 ppm.

Other research sites report the same static magnetic field inhomogeneity. The field strength drop in feet direction is not that apparent as it is in this thesis [Truong et al., 2006]. It might either be due the utilization of another magnet, or a less sensitive quantification technique. The conditions in the proximity of the frontal sinus lead to signal loss and artifacts in gradient-recalled echo (GRE) and spin echo (SE) imaging [Truong et al., 2006].

It is important to know whether or not the effect of the RF pulse on the magnetization and thus, the contrast and signal evolution must be regarded for or not. This effect certainly differs for the zoo of RF pulses and will be discussed for the most simple rectangular pulse at this point. There are two approaches to deal with off-resonance effects.

The first one is the optimization of the frequency response. From the physical background it is known, that the frequency profile can be approximated by the FOURIER transform of the pulse envelope. The FOURIER transform of a rectangle is a cardinal sine (sinc) with a bandwidth scaling inversely with the pulse duration; the shorter the pulse the broader the frequency response is. However, with a shorter pulse comes a higher amplitude of the RF field and thus a higher exposure to specific absorption rate (SAR). For this reason, it is not practical to reduce the duration to arbitrary short values; 1 ms is a good value though, see section 6.1.1. Additionally, it must not be forgotten that the concept of the FOURIER transform is only valid within the small tip angle approximation. Using the pulse for the preparation of the magnetization, e. g. as an inversion by 180 °, does not fulfill those conditions any longer. A replacement of the rectangular shape by a sinc function, and furthermore an optimization of the slice profile by the SHINNAR-LE ROUX (SLR) algorithm [Le Roux, 1986; Shinnar et al., 1989], would feature the same issues. Nevertheless, if the absolute variation of the static magnetic field is small enough, the pulses can be designed with an arbitrary robustness. No additional effort must be made within the quantification.

Another approach is the extension of the simulated parameter space, i. e. the correction library, into the static magnetic field dimension. The simulation tool, presented in the results section 4.1, is capable of calculating the off-resonance effect; more information is given in the respective section and will be discussed later on. There are several drawbacks to this approach, though. On the one side, the computational burden scales linearly with the size of each parameter space dimension. At the moment, the simulation for one typical protocol and 3D imaging takes about 3 h without regarding a variation of the static magnetic field amplitude. With such regard, this time frame will easily be extended to last several days or even weeks. The other drawback is concerning the robustness of the evaluation. With an additional free regression parameter, the optimization can more easily run into a local minimum due to the reduced uniqueness of the target space. The apparent tip angle scaling due to off-resonances or RF field inhomogeneity can be ambiguous.

If an adiabatic pulse is used for the preparation of the magnetization, the situation is less complex. The equation of motion and the composition of the effective magnetic field, see equations 2.38 and 2.39, have been explained in the physical background. For an adiabatic pulse, the z-component of this field is attributed by its off-resonance in time. Depending on the principle of adiabaticity, the pulse is either constantly on- or off-resonant. In case of a variation of the static magnetic field amplitude there is an additional contribution to the effective magnetic field. This will influence the dynamic range of the solid angle within the rotating reference frame. Or to clarify the same in a more illustrative manner, the adiabatic condition is fulfilled with a temporal delay or violated towards the end of the duration. In either case, the inversion will be non-perfect and leads to a disturbed signal. The same two approaches as for the conventional pulses can be applied to overcome these effects.

The frequency response, and besides that also the SAR exposure, can be optimized by the variable-rate selective excitation (VERSE) technique [Conolly et al., 1988]. Within a certain dynamic range, depending on the pulse parameters, off-resonance effects can be completely

disregarded. This is the case as long as the off-resonance from the static magnetic field is small enough compared to the off-resonance of the RF pulse itself [Bernstein et al., 2004], as applies for all applications within this thesis. If this is not sufficient, the simulation of the off-resonance effects can also be performed and regarded for in the evaluation.

In this study, the frequency response of the applied RF pulses has been simulated and measured on a homogeneity phantom. The off-resonance conditions were induced by a change of the transmission frequency. Within the quantified dynamic range of the magnetic field strength, no distinct deviations from the desired RF pulse effects were identified. As a consequence, no further regard has been given to the static magnetic field inhomogeneity within this range.

7.1.2 Radio Frequency Field Inhomogeneity

The band gap of the ZEEMAN levels increases with an increasing magnetic field strength. With the band gap, the transition frequency increases and the wavelength decreases. At a magnetic field strength of 7 T, the LARMOR frequency comes out to approximately 300 MHz and the wavelength takes value in the order of the imaged object [Van de Moortele et al., 2005]. The dielectric properties such as the permeability, permittivity, and conductivity of different tissue types, e. g. muscle, fat, or fluids, must also be considered [Kraff et al., 2015]. Constructive and destructive interferences of multiple reflections of the RF wave cause a spatial variation of the signal evolution. It does not only affect the absolute signal value, but also the contrast of the different tissue types.

The inhomogeneity of the RF field amplitude has been quantified for the human head and presented in section 6.1.2. Two important observations are recalled again at this point. An RF field amplitude drop into the feet direction and to both temporal sides of the brain appears. The first phenomenon can be assigned to the geometry and the limited size of the transmission birdcage of the coil. The second is most likely also correlated to the coil setup. Whether this is due to destructive interference can however not be concluded. The second observation concerns the central brightening effect. In the center of the brain, a strong hyperintense region forms. It is expected that the penetration depth of the RF is decreasing with increasing frequency and thus, the RF amplitude [Bottomley and Andrew, 1978]. In contrary, the measurements show that the superposition of multiple reflections interfere constructively. This central brightening is a known effect and often reported in literature [Truong et al., 2006]. The percentile, in which 90 % of all data points lie, spans a range from 0.18 to 1.35 of the nominal RF field amplitude. A comparison for the absolute statistics cannot be drawn. The transmission profile is specific for each individual coil and depends on the realization of the coil concept.

Again it is important to investigate how the RF pulses perform under such conditions. For conventional pulses this is easy to discuss. On-resonant spins show a direct linear scaling of the tip angle with the RF field amplitude; see equation 2.51. This can be computed by the simulation framework. Adiabatic pulses perform nearly perfect until the RF amplitude drops below a minimum threshold [Bernstein et al., 2004]. In this case, it is very hard to estimate the exact effect of the pulse; minimum changes in the local conditions already have a strong impact. It can be optimized though and made more robust with a number of

different numerical optimizations such as a genetic algorithm (GA) [Goldberg and Holland, 1988; Hurley et al., 2010]. For that reason, the adiabatic pulse is optimized and considered to be independent of the RF field amplitude.

Since the effects of the tip angle scaling cannot be neglected, it makes up one of the dimensions of the parameter space for the simulation. Within the respective dynamic range, the library will hold the adequate corrections.

7.2 Simulations of Spin Interactions

The first implementation to compute the Bloch equation was published in the mid 80's [Summers et al., 1986]. Soon, many of the simulation tools were intended for educational use and are thus limited in the variety of functions [Rundle et al., 1990; Torheim et al., 1994]. With the ongoing research in the field of MR physics, such simulations were used to improve the general understanding of the spin behavior [Shkarin and Spencer, 1996]. Eventually, the investigation of the origin of artifacts was performed by such synthetic experiments [Brenner et al., 1997].

At the time of this thesis, two simulation frameworks, namely SIMRI [Benoit-Cattin et al., 2005] and JEMRIS [Stocker et al., 2010], have been published that were promising to fulfill all the needs of this project. The benefits and drawbacks of both in comparison to the novel simulation design presented in this thesis will be discussed below. At first this is done for the implementation of the mathematical kernel in section 7.2.1. Next, the approach of how the simulation of composite pulses and pulse sequences is realized is discussed in section 7.2.2. Section 7.2.3 closes with a comparison of the computational burden.

7.2.1 Mathematical Kernel

The mathematical kernel is the core of the simulation tools. It processes the manipulation of the magnetization due to the interaction with an effective magnetic field and the relaxation processes. Within this thesis, the mathematical kernel has been implemented in a rotation matrix approach. In general this was also done for SIMRI and JEMRIS, but there are some major differences.

At first, an alternative to the rotation matrices shall be discussed. The problem defined by the equation of motion and the Bloch equation is expressed by an ordinary differential equation (ODE). It can be solved by a large variety of ODE solvers. Modern implementations of such solvers are capable of estimating the error of the non-permuting operations and dynamically set the time step durations of consecutive iterations. This reduces the computational burden when the effective magnetic field needs to be subclassified. To clarify what this means, RF pulses with non-constant amplitude or frequency, composite pulses, and MRI sequences are subclassified. The varying time step duration can also be interpreted as a limitation. For the determination of the exact signal value under the influence of k-space filters, a fixed time grid is mandatory. Simulating the signal evolution of a sequence on a fixed time grid will hold the same computational burden as for the rotation matrix approach. These are the main reason why the rotation matrix approach has been chosen.

The mathematical kernel of this thesis consists of the rotation of the magnetization around the effective magnetic field followed by the relaxation in form of a multiplication with a diagonal matrix and a vector addition; see equation 4.16. The transverse and longitudinal relaxations are independent of each other and thus, two consecutive and non-permuting operations are computed. This minimizes the accumulation of errors in time.

The SIMRI simulation tool, in contrast, encompasses a kernel that performs four consecutive operations: a rotation around the z-axis due to a magnetic gradient field, another rotation around the z-axis due to static magnetic field inhomogeneity, the relaxation, and the rotation induced by the RF around an axis in the transverse plane only [Benoit-Cattin et al., 2005]. Furthermore, in the absence of a magnetic gradient, the rotation of the RF itself consists of three individual rotations: first a rotation around the z-axis by the phase angle of the pulse, next a rotation about x by the tip angle of the pulse, and finally a rewinding around z again by the negative phase angle. In presence of a magnetic gradient it gets even more complicated. An effective tip angle for the magnetization vectors and an additional rotation around the z-axis due to off-resonance are defined. In total, the mathematical kernel of the SIMRI simulation tool performs at least 7 non-permuting rotations. Therefore, the accumulated error of the operation at the same time step duration will be larger for SIMRI than for the approach presented in this thesis. Alternatively, the time step duration could be shortened but that leads to a higher computational burden. Moreover, the inhomogeneity of the RF field is not regarded for so far, but the kernel can be expanded [Benoit-Cattin et al., 2005].

The mathematical kernel of JEMRIS is more advanced. While the relaxation is handled the same way as in this thesis, the rotation of the precession motion is separated into two matrices [Stocker et al., 2010]. The z-component of the effective magnetic field and the phase of the RF pulse are isolated from the RF field and coupled with the relaxation. As a result of the order of these operations, the magnetization first precesses and relaxes and is then turned around an axis of the transverse plane. Whether this holds a larger error than the approach of this thesis is hard to estimate.

The numerical errors caused by the discrete computation of the new approach presented in this thesis have been estimated and analyzed. Within the respective time step durations, the simulation is in a strong agreement with measurements [Breithaupt et al., 2012] and in perfect agreement with available analytical expressions. Thus, the presented implementation is suitable for the simulation of spin interactions.

7.2.2 Composite Pulses and Pulse Sequences

The succession of a number of MRI sequence elements can be achieved by the simulation tool presented in this thesis in two different ways. Either the program is called several times for the different objects, each time passing the new initial state and the equilibrium state, or one externally defined object is used. In the approach presented in this thesis, a virtual analog digital converter (ADC) event is specified and the corresponding complex values of the magnetization at the given time points are stored in a virtual k-space; more information is given in the respective results section 4.1.5.

The SIMRI simulation pursues a very similar approach. It classifies the sequence into different events: free precession, magnetic gradient, 1D data acquisition, and RF pulses

[Benoit-Cattin et al., 2005]. If necessary, they are subclassified into constant parameters for each time step. The signal values are stored within a k-space matrix. However in extension to this, the simulation tool presented in this thesis is not just capable of simulating the signal evolution, but it can also generate a weighting matrix to regard for the k-space filters that evolve during the readout.

JEMRIS offers the most advanced graphical user interface. Any MRI sequence can be assembled by nodes and building blocks [Stocker et al., 2010]. This is an advantage compared to the command line execution of the new simulation framework presented in this thesis in terms of user friendliness. However, it is unknown how exactly the individual building blocks are handled. Most likely, it is done analogous to SIMRI and the tool introduced within this thesis.

At last, three remarks regarding additional features of the new simulation tool must be made. In particular these features are: spatiotemporal object variations, parallel transmission, and spin dephasing within voxels. Spatiotemporal object variations can be interpreted as motion or flow. Also, issues with stability of the magnetic fields can be addressed this way. The concept and the significance of parallel transmission is a topic by itself and will not be explained within this thesis. With the dephasing of the spins inside a voxel, MRI sequence elements such as spoiler gradients or physical phenomena such as diffusion can be simulated. It is not published whether SIMRI is in the power of performing these features [Benoit-Cattin et al., 2005], while the programmers of JEMRIS list these features as future developments to come [Stocker et al., 2010]. However, both, the new approach and JEMRIS, are limited to the solution of the equation of motion and the Bloch equations [Stocker et al., 2010]. Any physics beyond this point can certainly be regarded for, but is a target of future development.

In the context of this thesis, the simulation tool proved to be capable to simulate magnetization prepared GRE sequences. The signal as well as the k-space filters could be determined for arbitrary tissue types. The user interaction was not implemented via a graphical user interface, but as a command line. This way, program calls were more complicated but allowed scripted executions for parameter studies.

7.2.3 High Performance Computing and Complexity Estimation

How the computational burden is handled by the different simulation tools is an essential factor for the usability. Just to give an impression, an RF pulse might be classified into a few thousand steps, the gradients and the data acquisition into a few hundred. Such an acquisition pattern will be called a few hundred times within one MRI sequence. The magnetization space varies in the range of 100^2 entries in 2D and 100^3 in 3D. Overall, this accounts to approximately 10^9 kernel calls. There are different implemented approaches to resolve this issue to a certain degree.

As it has been outlined before, the simulation tool presented in this thesis is implemented in MATLAB. MATLAB executables are less time efficient than C/C++ ones, except for matrix operations. However, due to the large variety of predefined functions, MATLAB code is easier to maintain. To benefit from the advantages of both, MATLAB and C/C++, all time consuming functions have been outsourced into MEX-files. Yet, the most effective

calculation time reduction originates from the simplification of the problem by extracting a unique set of parameters and computing these only; see section 4.1.6 for more information. The parallelization is done on the function calls themselves, not on the magnetization space, and can be distributed to multi CPU computers or high performance computing (HPC) systems.

SIMRI is implemented in the programming language of C with high level function calls and can be parallelized within a PC grid architecture [Benoit-Cattin et al., 2005].

The JEMRIS simulation software is implemented with an object-oriented design in C++ [Stocker et al., 2010] and relies on several libraries. For parallelization, the sample is split into equal portions which are distributed to the working nodes.

From the first implementation to the final code, the efficiency of the program was improved by a factor of 1000 or more, strongly depending on the specific problem. Although the calculation of the k-space filters of 3D parameter spaces can last several hours, no limitations occurred due to an additional need of resources. The impact of the simulation is discussed in the following section.

7.3 Volumetric T_1 Quantification

One of the motivations behind quantitative imaging is the RF field bias-independent contrast. Furthermore, investigations hereby are reproducible and comparable for multi-site and longitudinal studies. The quantification of longitudinal relaxation times plays a special role as an indicator, e. g. for the tumor aggressiveness [Steen et al., 1994]. Many different approaches have been proposed and investigated to determine this tissue specific parameter. Most of these are based on magnetization prepared or tip angle altered spoiled GRE sequences [Christensen et al., 1974]. The most prominent implementations are the Look-Locker approach [Look and Locker, 1970] with an echo planar imaging (EPI) or *fast low angle shot* (FLASH) readout [Gowland and Mansfield, 1993; Deichmann et al., 1999]. At last, the methods based on driven-equilibrium single-pulse observation of T_1 relaxation (DESPOT1) shall also be mentioned here [Deoni et al., 2003; Deoni, 2007].

Although the approach introduced in this thesis is derived from the DESPOT1 with high-speed incorporation of RF field inhomogeneities (DESPOT1-HIFI) method [Deoni, 2007], it features more resemblance with the MP2RAGE technique and magnetic resonance fingerprinting (MRF) [Van de Moortele et al., 2009; Ma et al., 2013]. Before a comparison is drawn to the alternative quantification methods, the novel evaluation strategies are discussed [Breithaupt et al., 2014]. The significance of the simulation of the signal with or without the k-space filters is addressed in section 7.3.1. In the following section 7.3.2, the correction techniques based on the simulation are compared. Finally, similarities and differences with the benefits and drawbacks are pointed out in the context of alternative quantification methods in section 7.3.3.

7.3.1 Predicting the MR Signal

For the novel quantification approach presented in this thesis, the signal is derived from numerical simulations of the respective MRI sequences as presented in section 4.2. The

equation of motion and the BLOCH equation are solved consecutively for each time step, and at predefined ADC events, the complex transverse signal is stored in a virtual k-space. The focus of these simulations lies on the influence of the readout for magnetization prepared states and the impact on the repetition pattern. An analytical solution for the manipulation by a FLASH readout has been introduced in 1992 [Deichmann and Haase, 1992]. In this approach, the signal and steady-state of the preparation can be calculated from the evolution of the longitudinal magnetization. The numerical simulation and the analytical determination are in a perfect agreement, but this is not explicitly presented within this thesis.

However, if the FLASH readout is replaced by a non-spoiled data acquisition technique, then the analytical expression is no longer valid in general. In these cases the signal does not only depend on the longitudinal magnetization disturbed by the excitation RF pulses, but also on the remaining transverse or rewound signal; this is especially the case for fully-balanced steady-state free precession (SSFP) sequences [Oppelt et al., 1986]. Dephasing influences of non-perfect spoiling would also lead to similar deviations from theory [Zur et al., 1991]. Also not accounted for in the analytical expression are relaxation effects during the RF pulses; the hard pulse approximation is used for the mathematical derivation. In a more complex setup for 2D imaging, the need of simulating the slice profiles for different RF pulses will arise [Breithaupt et al., 2012]. If the small tip angle approximation is not fulfilled, the determination of the frequency response by a FOURIER transform is not valid anymore. These profiles must be calculated by a numerical solution of the equation of motion. The simulation tool presented in this thesis is capable to perform all these operations so that these effects can be regarded for.

An additional feature that exceeds the analytically expressed theory is given by the simulation of k-space filters; see section 4.2.5 for more information. The signal information is not just stored in the center of the k-space, but distributed all over it. Especially the filter into the phase encoding (PE) direction and the corresponding point spread function (PSF) causes a signal deviation [Deichmann et al., 2000]. The blurring due to the apparent transverse relaxation with an exponential envelope in readout or frequency encoding (RO) direction and the transient oscillations into the partition direction impact the signal amplitude. As a consequence, the effect on the signal amplitude depends on the size and the shape as well as the physical properties of the structure itself. Nevertheless, the weighting of the low frequency lines of k-space can be investigated on a virtual dataset [Berger et al., 2011]. A FLASH readout drives the magnetization into the respective steady-state. Thus, the actual signal will always be closer to the one of this steady-state than the predicted one. The effect of this k-space filter is depending on the ordering of the PE lines [Lin and Bernstein, 2008]; a centrically ordered acquisition scheme, as used within this thesis, holds the smallest error. This can also only be calculated with a more sophisticated numerical simulation as the one introduced within this thesis.

Within this thesis, the quantification of the longitudinal relaxation time is corrected by the simulated signals, as presented below. It can be stated, that the quality of the determination is improved. How the two different signal types impact the accuracy of the quantification is shown in the next section.

7.3.2 Signal Correction Techniques

Three different approaches on how to use the simulated signal values for the correction of the measurements have been introduced in this thesis: the scaling of the signal, the calculation of a virtual initial magnetization, and the direct matching of the signal. The motivation and the reasonability as well as the performance of each correction must be discussed. A thorough comparison to alternative simulation-based approaches cannot be drawn due to the limited number of publications available for this topic.

The signal scaling can be understood as the correction of each signal sample point to fit the original theory. This is done by extracting the corresponding correction factor from a lookup table for each trial point within the optimization. The novel approach bears the advantage that the resulting signal value distribution directly resembles the given theory; i. e. the inversion recovery experiment is still described by an exponential function. However, experiments on virtual data have shown that the evaluation is unstable for the inclusion of arbitrary sample points (see section 6.2.1). Signal amplitudes close to zero cause singularities in the lookup tables and thus, the interpolated drawings of the optimization process yields numerical errors. Which sample points are affected depends on the respective theory to be corrected for, i. e. in the context of this thesis the inversion recovery (IR) theory and the IR theory with a reduced repetition time of the preparation. Without giving special regard to the imprinted signal values and thus, the limitation in the choice of the respective MRI sequence parameters, this approach will not hold in practice.

As indicated by the name, the calculation of the virtual initial magnetization concerns the state of the spin system prior to the magnetization preparation. If the effect of the k-space filters must be regarded, an analytical expression cannot be given any longer, as discussed above. The absolute value of the virtual magnetization may exceed the one corresponding to the equilibrium state. Although this is not intuitive, it can easily be exemplified for an IR spoiled GRE experiment. When the prepared magnetization is above the level of the FLASH steady-state of the readout, then the k-space filters reduce the actual signal value. As a consequence, the starting point of the relaxation process must also be of reduced amplitude to compensate for this. For a perfect inversion of the equilibrium state, this means that the absolute normalized virtual magnetization must be larger than the equilibrium magnetization itself. In practice, this approach performs more accurately and stable than the scaling of the signal, but is still outperformed by the signal matching.

The direct matching of the signal values to the entries of a lookup table has been introduced in the same time frame as it was done for MRF [Ma et al., 2013]. With respect to all physical parameters of the magnetization, the vector can be scaled by a free parameter corresponding to the apparent proton density (PD). No theoretical description of the signal behavior is needed. The experiment can consist of any set of MRI sequences and any contrast. As long as the evolution of the signal can be simulated, the correction in this manner is valid. Quantification hereby has shown a high stability and accuracy and outperformed the other approaches also in a reduced computational burden (see section 6.2).

In conclusion, the matching of the signal to the simulated signal values with the effect of the k-space filters performs the best. Therefore, all respective experiments presented in this thesis have been evaluated with this strategy.

7.3.3 Alternative T_1 Quantification Methods

As outlined above, two alternative methods for the quantification of the longitudinal relaxation time are set into relation with the works of this thesis. The MP2RAGE sequence acquires two different contrasts following one preparation [Marques et al., 2008]. By combining the two signals, the field bias from the coil sensitivity profiles can be removed to improve the contrast of the weighted images [Van de Moortele et al., 2009]. Furthermore, by calculating the impact of the readout on the evolution of the magnetization the longitudinal relaxation time can be estimated [Marques et al., 2010].

The dependence on the RF field amplitude is not completely resolved in the evaluation process of the MP2RAGE method. As a consequence, the error of the quantification of the longitudinal relaxation time comes out to e. g. 4.9 % for gray matter [Marques et al., 2010]. This is due to the lack of efficiency of the adiabatic preparation pulse at low RF amplitudes. Of course the same accounts for the adiabatic preparation utilized within this thesis. However, due to the intrinsic RF field mapping, the efficiency of the RF pulse can be estimated. Alternatively, the novel approach features a preparation by a conventional rectangular pulse where the efficiency directly scales with the RF field amplitude. This way, the inhomogeneity of the RF field distributions can be completely regarded for. The MP2RAGE additionally suffers from the PSF along the PE direction and the linearly ordered data acquisition [Marques et al., 2010]. As mentioned above, the ordering scheme and the signal offset due to the k-space filters have been addressed by the simulations for the corrections introduced within this thesis. The temporal efficiency of the MP2RAGE method is higher than for the new approach. Within approximately 6:30 min a 1 mm isotropic map of the longitudinal relaxation time of the whole brain can be acquired at a magnetic field strength of 7 T [Marques et al., 2010]. The imaging has been accelerated by parallel imaging and partial fourier techniques. The novel simulation-based approach takes about 25 min for the same resolution and field of view (FOV) without employing any acceleration methods [Breithaupt et al., 2014]. If the same acceleration techniques were included, then the novel approach would perform with the same temporal efficiency.

Another method that is also based on simulations is MRF. In 2013 it was proposed to do a single-shot imaging with a spiral readout of consecutive non-steady state contrasts [Ma et al., 2013]. The tip angle and timing parameters of a fully-balanced SSFP sequence are deliberately changed to evoke a unique evolution of the signal, i. e. a fingerprint. By matching the fingerprint of each volume element to the entries of a library, all respective physical parameters of the magnetization can be quantified.

To differentiate the effects caused by different physical parameters involved in the formation of each contrast, MRF needs up to 1000 images. All images are strongly impacted by artifact from the highly undersampled data acquisition. The artifacts are coherent in space and only noise-like in time, though. It can be stated, that MRF is using a large number of poor SNR images for the quantification in contrast to the approach introduced in this thesis, which uses only a comparably small number of high SNR images. Due to the availability of a greater variation of contrasts in MRF, not only can the longitudinal relaxation time and the RF field amplitude be quantified, but also the transverse relaxation time and the static magnet field inhomogeneity [Ma et al., 2013]. A limitation of the single-shot MRF technique is the achievable spatial resolution. The undersampling of

k-space can only be performed up to a certain degree. It is reported that quantitative maps with a spatial resolution of 2.34×2.34×5.00 mm can be acquired within 12.3 s [Ma et al., 2013]. The efficiency of MRF is a factor of 1.8 times higher than for the DESPOT1 methods [Ma et al., 2013]. A fair comparison at high resolution in the order of or higher than 1 mm has not and cannot be drawn since MRF is a 2D technique. Thus, MRF is more efficient at low resolution than the new approach presented in this thesis, but is mostly likely to lose its efficiency at higher resolutions. The newly presented volumetric quantification technique performs best at a high spatial resolution of large volumes in 3D imaging, as discussed below.

7.4 Simulations and Experiments

To estimate the accuracy and efficiency of a quantification method, it is important to evaluate its performance for actual measurements. In various studies, different strategies are pursued to give insights into the behavior of the respective approaches. This section summarizes those considerations and sets them into relation to the work presented in this thesis. It has already been outlined before, that the complete variety of different quantitative imaging methods is too wide to be fully covered within this thesis. For this reason, only a limited number of alternative approaches will be discussed in the following: three-point DESPOT1 [Li and Deoni, 2006], DESPOT1-HIFI [Deoni, 2007], MP2RAGE [Marques et al., 2010], and MRF [Ma et al., 2013].

The novel simulation-based quantification approach is evaluated using simulation experiments and measurements of the contrast phantom. All respective results are discussed in section 7.4.1. Furthermore, two *in vivo* applications of the simulation-based DESPOT1-HIFI (SIMBA DESPOT1-HIFI) for the quantification of the longitudinal relaxation T_1 time are presented in section 6.2.3 and discussed in section 7.4.2.

7.4.1 Phantom Studies

The accuracy of the quantification process can be specified either as a deviation from or by a correlation coefficient to a nominal value. Within this thesis, both quantities were calculated and listed throughout the results sections 6.2.1 to 6.2.2 to allow for a direct comparison to literature values. The simulation-based IR (SIMBA IR) method quantifies T_1 with an accuracy in terms of a deviation of less than 2 %, while the coefficient of determination to the reference values comes accounts to 0.99 in a range of T_1 values from 1100 ms to 3300 ms. A systematic underestimation of the longitudinal relaxation time is most likely due to blurring affects from the single-shot FLASH readout; this is discussed in the previous section. The accelerated SIMBA DESPOT1-HIFI approach bears a quantification accuracy of approximately 3 % and a corresponding correlation to the reference of 0.98.

The first comparison of the accuracy of the SIMBA DESPOT1-HIFI method is outlined against the original DESPOT1-HIFI method [Deoni, 2007]. It has been reported, that the accuracy of the original method for T_1 is greater than 5 % in the range of 300 ms to 2500 ms [Deoni, 2007]. Furthermore, it depends on the choice of the sequence parameters. From the presented data, it can however not be approximated how the method would perform for longer relaxation times, as encountered at higher static magnetic field strengths.

Moreover, in section 4.2.2 it is pointed out, that the original approach likely suffers from a non-accurate theory. Within this thesis, the mean deviation of the original DESPOT1-HIFI from the reference was found to be more than 10 % (see section 6.2.2).

In the publication presenting the quantification of the longitudinal relaxation time with the MP2RAGE sequence [Van de Moortele et al., 2009], the accuracy has been specified in the same manner. Within a T_1 range of 700 ms to 4200 ms, the accuracy is 2 % [Marques et al., 2010]. Especially for long longitudinal relaxation times this method does hold a higher accuracy than the approach presented in this thesis. However, the evaluation was performed on simulation data only and with an SNR of 10 [Marques et al., 2010]. A direct performance comparison on experimental data has not been given.

The accuracy of MRF has been quantified by the concordance coefficient as a measure of correlation. Although it cannot be set into a direct relation to the coefficient of determination, a rough comparison will be made. The correlation of MRF to the IR SE experiment is 0.988 [Ma et al., 2013]. This is the same reference as used for the work presented in this thesis. A second correlation to the original DESPOT1 method of 0.956 has also been calculated [Ma et al., 2013]. It has been discussed above, that the SIMBA DESPOT1-HIFI approach performs more accurate than the original DESPOT1-HIFI approach and it can be considered, that SIMBA DESPOT1-HIFI performs more accurate than MRF.

The efficiency of different quantitative mapping techniques is more difficult to be compared. It strongly depends on whether it is a 2D or 3D method and on the size of the imaging matrices for a given resolution. In this thesis, a rough comparison is done by calculating the acquisition time for one volume element. The SIMBA DESPOT1-HIFI method acquires 256×256×176 voxels within approximately 25 min resulting in a measurement time of 0.13 ms for one voxel. As a comparison, the three-point DESPOT1 method needs 0.57 ms and the MP2RAGE approach 0.06 ms [Li and Deoni, 2006; Marques et al., 2010]. The standard DESPOT1 is 30 % faster than the three-point approach [Li and Deoni, 2006] and by a factor of 1.87 less efficient than MRF [Ma et al., 2013]. However it must be again pointed out, that it is hard to conclude which method is absolutely the most efficient, because efficiency relies on the size of the FOV and the desired resolution. From this comparison, SIMBA DESPOT1-HIFI has the second highest efficiency among the considered methods, only outnumbered by MP2RAGE. However, if similar acceleration techniques are used for the SIMBA DESPOT1-HIFI method, then the same efficiency is the result, as discussed in section 7.3.3.

7.4.2 3D *in vivo* Studies

As a final investigation of this thesis, two different *in vivo* applications of the novel SIMBA DESPOT1-HIFI approach have been performed (see section 6.2.3). The whole brain as well as the calf muscle of two healthy volunteers were examined. How the novel evaluation strategy performs has been discussed in detail above and will not be repeated in the following. The sole purpose of this section is to compare the quantified values for the longitudinal relaxation times with the current literature.

Whole Brain The brain is one of the preferred parts of the human body to be investigated. With the SIMBA DESPOT1-HIFI approach, the whole brain was covered in a FOV of

Table 7.1: T_1 values of the gray and white matter of the human brain. All reported values are in a good agreement within the respective uncertainty ranges. Differences of the quantified longitudinal relaxation times T_1 must not solely be attributed to the accuracy of the mapping techniques, but are also a characteristic of human individuals.

	T_1 [ms]		
Study	gray matter	white matter	Method
[Li and Deoni, 2006]	2000±100	1500±100	three-point DESPOT1
[Ikonomidou et al., 2006]	2007±45	1357±22	multi-slice IR EPI
[Rooney et al., 2007]	2132±103	1220±36	mod. Look-Locker
[Wright et al., 2008]	1940±150	1130±100	MPRAGE
[Marques et al., 2010]	1920±160	1150±60	MP2RAGE
This study	1917±95	1246±56	SIMBA DESPOT1-HIFI

$256\times256\times176\,\mathrm{mm}^3$ with an isotropic resolution of 1 mm and a measurement time of 28:57 min. Table 7.1 lists a selection of the quantified longitudinal relaxation times T_1 for the gray and white matter by different methods and a static magnetic field strength of 7 T. The results overall show a good agreement. Differences of the T_1 values are not necessarily due to the accuracy of the methods themselves, but can also be attributed to individual characteristics of each investigated subject. The values of the longitudinal relaxation time quantified by the SIMBA DESPOT1-HIFI come out to (1917±95) ms for gray matter and (1246±56) for white matter.

Calf Muscle At the time this thesis was finished, there was only one published report on the longitudinal relaxation time of the human calf muscle. The approach presented in this thesis quantified T_1 to (1877±92) ms for the same parameters as for the head but with a non-adiabatic inversion pulse. A study using the 2D saturation recovery (SR) experiment listed a T_1 of (1864±243) ms [Marschar et al., 2014]. These two values are in a strong agreement. Furthermore, the fat tissue and the bone marrow are reported to have a T_1 value of approximately 500 ms [Ren et al., 2008; Marschar et al., 2014]. Since this value corresponds to the limit of the lookup table of the correction libraries generated in this thesis, it can be regarded as the reason why the evaluation of the fatty tissues failed.

***T_1* Artifact** A new artifact appeared in the non-adiabatic SIMBA DESPOT1-HIFI experiment that had not been identified before. In a certain range of tip angles, the longitudinal relaxation time is overestimated. For the given experiment the relative tip angle scaling ranges from approximately 1.15 to 1.30. However, these are proper conditions for the evaluation to supposably perform accurately; inaccuracies of the quantification have previously only been identified for low RF field amplitudes. One possible explanation for this artifact is proposed in the following.

The relative scaling has a different effect on the absolute values of the large preparation and small readout tip angles. Within the IR experiment, a non-adiabatic inversion holds the same effect on the magnetization for symmetric deviations of the 180 ° tip angle. Those two signals will only scale with the different tip angles of the FLASH readout. However, the two corresponding readout tip angles are of comparable values and will neither cause

a significant signal change, nor influence the state of the magnetization prior to the next preparation. Thus, the signal of the IR experiments primarily depends on the inversion time and T_1. The signal of the FLASH experiments scales only with the readout tip angle and T_1. However, the FLASH steady-state signals are not sufficiently dissimilar under a variation of the tip angle at a magnetic field strength of 7 T.

As a consequence, the optimization problem becomes ill-posed for a non-adiabatic preparation and an ambiguity of T_1 and tip angle values evolves. Under real SNR conditions, the quantified parameters may results from a convergence of the target function into a local minimum. This is only one possible explanation and further investigations of this behavior must be undertaken.

8 Summary and Outlook

Magnetic resonance imaging (MRI) at ultra high field (UHF) features an improved signal to noise ratio (SNR) compared to standard clinical examinations. However, accompanying static magnetic and radio frequency (RF) field inhomogeneities cause signal variations in weighted magnetic resonance (MR) images and lead to false positive and negative contrasts. A correction of the field biases is one approach to overcome these challenges and to allow for quantitative imaging. Additionally, maps presenting the quantified physical parameters of a sample exhibit a strong contrast and are reproducible and comparable in inter-site and longitudinal studies. However, conventional mapping methods require a measurement time frame beyond any clinical reasonability.

In this thesis, a novel quantitative imaging technique, capable of generating volumetric and spatially high-resolved maps of the longitudinal relaxation time T_1 within a clinical time frame, is introduced. This method is based on the prediction of the MR signal disturbances, which are due to the field inhomogeneities and the influences of the MRI sequence readout itself, as well as the correction hereby. The basis of the imaging process is provided by differently contrasted *fast low angle shot* (FLASH) and inversion recovery (IR) experiments.

The required prediction of the MR signals is performed by the simulation of the complete MRI experiments. For this purpose, the mathematics behind the equation of motion and the Bloch equations were implemented into a new framework. To efficiently compute the effect of an arbitrarily natured effective magnetic field on the magnetization, a rotation matrix approach was developed. Any basic condition can be specified by means of the static magnetic and RF field amplitude, the initial and equilibrium magnetization, and the longitudinal, transverse, and apparent transverse relaxation times. Furthermore, the impact of noise contributions and motion can be regarded for in order to approximate the real experimental conditions as close as possible. Supplementary, an interface for the optimization of MRI sequence parameters has also been created to address upcoming approaches such as magnetic resonance fingerprinting (MRF) or parallel transmission (pTx). The developed simulation tool has been validated to generate results that are in perfect agreement with solutions of analytically describable problems and in a strong agreement with actual MR measurements.

The novel quantitative imaging technique has been realized for the gold standard IR as well as the DESPOT1-HIFI methods. In this thesis, the corresponding approaches are referred to as the simulation-based IR (SIMBA IR) and simulation-based DESPOT1-HIFI (SIMBA DESPOT1-HIFI) methods, respectively. Three different approaches to correct the measured MR signals have been pointed out. The first option is to introduce a scaling factor into the respective common evaluation theory to correct the signal of each sampling point independently. Another option is valid for the IR experiment only. It comprises the calculation of the disturbance on the longitudinal magnetization and the determination of the magnetization's virtual initial state to regard it within the regression

expression. A third option is the direct matching of the measured signal value to the predicted value. The individual advantages and disadvantages of each of these approaches have been analyzed. The scaling of the signal is very intuitive but relies on correction tables that may feature singularities and thus cause numerical instabilities within the evaluation. With the calculation of the virtual initial magnetization these issues are resolved on the one hand, but on the other hand the strategy is only valid for IR signals. By matching the signal directly to the predicted value, the evaluation is very flexible and not limited to the availability of an analytical signal equation. The nature of the predicted signal can either be the deflection of the longitudinal magnetization or the additional consideration of a weighting matrix in k-space. For the second case, a concept similar to the one of excitation k-space has been introduced and implemented into the new simulation framework. All correction strategies have been investigated in simulation, phantom, and *in vivo* studies.

Simulation studies allowed gaining a deeper understanding of the performance of the correction strategies. The direct matching based on the k-space weighted signal was identified to be the most accurate and robust approach. One major result of the SIMBA IR phantom studies was the proof of concept of the novel quantification technique for an imperfectly relaxed longitudinal magnetization. Furthermore, it has been shown that the measurement time can be reduced by more than 50 % with an accompanying improvement of the accuracy in terms of a mean deviation of (-0.42±1.23) %. A replacement of the adiabatic by a non-adiabatic IR preparation yields a respective accuracy of (-1.13±4.27) %. This implies that the method is more unstable than with an adiabatic preparation. However, the specific absorption rate (SAR) exposure is reduced by approximately 70 % and applications near organs of risk or with coils featuring a strongly inhomogeneous RF field distribution become feasible. Moreover, phantom studies with the SIMBA DESPOT1-HIFI method on two optimized contrasts of the FLASH and IR experiment revealed a T_1 mean deviation of (1.99±1.58) %.

Eventually, two initial *in vivo* examinations of the human head and calf have been performed with a field of view (FOV) of 256×256×176 mm^3 and an isotropic resolution of 1 mm within less than 30 min each. Both, the adiabatically and non-adiabatically prepared quantification methods, performed very robust under the given field inhomogeneities even for low RF amplitudes. The corresponding T_1 maps showed a clear tissue contrast and differentiation. The longitudinal relaxation time of gray and white matter of a human brain accounted for (1917±95) ms and (1246±56) ms, respectively. The quantification of the human calf muscle revealed a T_1 value of (1877±92) ms. Both results are in a good agreement with literature values.

One option for a future advancement is the involvement of additional magnetic resonance imaging (MRI) sequences within the presented quantitative imaging technique. The presented quantitative imaging process is not limited to the FLASH and IR experiments only. In fact, with the application of the signal matching correction, there is no need for the signal to be analytically describable. This would allow for the extension to a greater number of physical parameters, such as the transverse or apparent transverse relaxation times as well as the diffusion coefficient, to be quantified and a more accurate evaluation.

Another topic for a future improvement of the technique is the complete deconvolution of all k-space filters. If the spatial distribution of the magnetization with the corresponding physical parameter would be known, then the blurring due to the readout could be determined. Within an iterative approach, corrected images could be repeatedly calculated and analyzed. The resulting quantified parameters would be more accurate especially for small and sharply defined structures.

Overall, the novel simulation-based quantitative imaging techniques are promising to be applicable in clinical trials and routine. By the time this thesis was finished, first possibilities for cooperations with the medical department were discussed and outlined. For this reason, the evaluation method has been implemented into the diagnostics framework MITK operated by the physicians.

List of Abbreviations

ADC analog digital converter

ASL arterial spin labeling

CAD computer-aided design

CPMG Carr-Purcell-Meiboom-Gill

CSF cerebrospinal fluid

CT computed tomography

DESPOT1 driven-equilibrium single-pulse observation of T_1 relaxation

DESPOT1-HIFI DESPOT1 with high-speed incorporation of RF field inhomogeneities

DIPP DKFZ Image Processing Platform

EPI echo planar imaging

FLASH *fast low angle shot*

fMRI functional magnetic resonance imaging

FMT fluorescence mediated tomography

FOV field of view

FWHM full width at half maximum

GA genetic algorithm

GRE gradient-recalled echo

HPC high performance computing

HS hyperbolic secant

IDEA Integrated Development Environment for Applications

ICE Image Calculation Environment

IR inversion recovery

ITK Insight Segmentation and Registration Toolkit

MITK Medical Imaging Interaction Toolkit

MP magnetization preparation

MPRAGE magnetization prepared rapid gradient echo

MR magnetic resonance

MRI magnetic resonance imaging

MRF magnetic resonance fingerprinting

NMR nuclear magnetic resonance

MT magnetization transfer

OCT optimal control theory

ODE ordinary differential equation

PART partition encoding

PD proton density

PE phase encoding

PMMA poly(methyl methacrylate)

PNS peripheral nerve stimulation

POET Protocol Off-line Editing Tool

PSF point spread function

pTx parallel transmission

RF radio frequency

RO readout or frequency encoding

ROI region of interest

SAR specific absorption rate

SDE Sequence Development Environment

SE spin echo

SENSE sensitivity encoding

SIMBA DESPOT1-HIFI simulation-based DESPOT1-HIFI

SIMBA IR simulation-based IR

sinc cardinal sine

SLR Shinnar-Le Roux

SNR signal to noise ratio

SR saturation recovery

SS slice-selection

SSFP steady-state free precession

SSI steady-state incoherent

TOF time of flight

TTL transistor-transistor logic

UHF ultra high field

GRAPPA generalized autocalibrating partial parallel acquisition

SPECT single-photon emission tomography

PET positron emission tomography

US ultrasound

trFOCI time resampled frequency offset corrected inversion

VERSE variable-rate selective excitation

VTK Visualization Toolkit

XML Extensible Markup Language

List of Figures

List of Tables

Appendix: Simulation Framework

The implemented framework can be classified into three sections: the initialization (init), the preparation (prep), and the execution (run) as shown in figure 8.1(a). To execute the code, the initialization function must be called while passing the following parameters (all important variables are specifically named and highlighted). The `SIM` object holds general information about where to find the initial data as well as how to handle and store the results. Both objects `PHANTOM` and `FLOW` define the physical parameters of the magnetization space and how it changes throughout time. The gradient fields are defined by the parameters of the position space in the `FOV` variable and geometric parameters about the slice-selective manipulation in the `SLICE` variable. Finally, the radio frequency (RF) pulse, the potential modulation and noise are characterized by the objects `PULSE`, `PULSE MOD`, and `PULSE NOISE`, respectively.

The initialization section of the code encompasses functions that set up the obligatory conditions; see figure 8.1(b). At first, the project folder structure is prepared and cleared if necessary. All parameters of the function call are saved into a log file.

Next, the phantom data, including all physical parameters, is loaded from the hard drive. If specified, a set of matrices to regard the flow motion is loaded as well. Furthermore, the initial state of the magnetization is determined and set to equilibrium or likewise loaded. This is followed by the scaling of the magnetization space and, if specified, the inner-voxel supersampling.

A set of variables describing the equilibrium magnetization $\mathtt{M}_0$ and the initial magnetization $\mathtt{M}_{\mathtt{init}}$ is the result. The longitudinal, transverse, and apparent transverse relaxation times are stored in $\mathtt{T}_1$, $\mathtt{T}_2$, $\mathtt{app.T}_2$, respectively. Fields map variables are $\mathtt{B}_0$ for the static magnetic field and $\mathtt{B}_1$ for the RF field. The last variable concerns the displacement vector $\Delta\mathtt{r}$ of motion. At the end, the next block of the preparation section is called.

Within the preparation section, the effective magnetic field and the scalar gradient fields are declared, see figure 8.2. It begins with the definition of the primary RF pulse, followed by the potential modulation and noise contributions. An RF pulse can either be picked from a predefined library or loaded from the hard drive as an external pulse.

Next, the first simplification of the computational burden is performed. Despite the amplitude of the gradient fields, they only differ in their orientation. For this reason, a unique set of orientations and a lookup table `LUT` for all time steps is determined and computed. A gradient field is calculated for each orientation; this matrix is similar to a distance map. The same accounts for the definition of the supersampling gradient.

The RF pulse is stored within the variables `RF` for all pulse forms, `GRAD` for the gradient amplitude, `ADC` for the k-space indices, and $\Delta\mathtt{t}$ for the time step durations. The two gradient fields are represented by the `GRADIENT` and the `DEPHASE` objects. At the end, all necessary information for the run section is gathered and passed to the final code block.

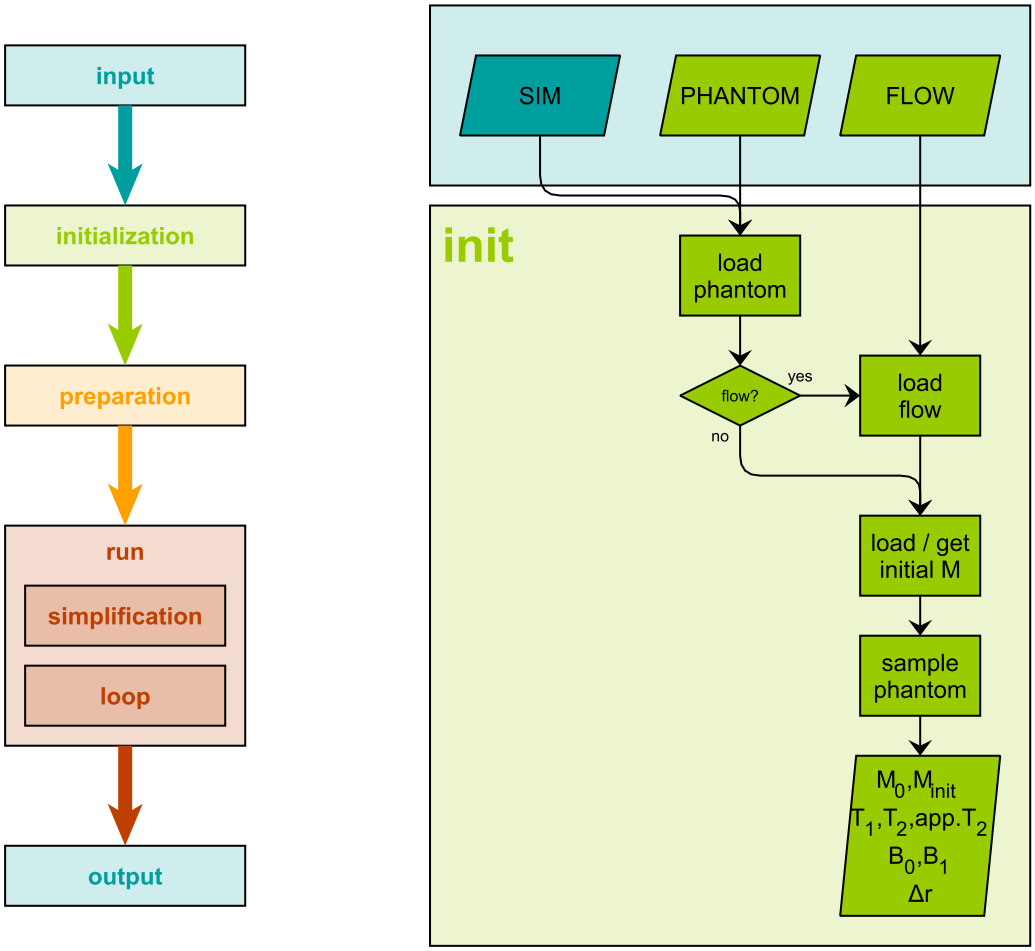

(a) (b)

Figure 8.1: Illustration of the simulation tool: overview and initialization. (a) This overview shows how the tool can be split into three parts, the initialization, preparation, and run section. The run section itself can be divided into a simplification and a loop part. (b) Within the initialization, the phantom data of the magnetization and the physical parameters are loaded at first. Motion effects are prepared next, then the initial magnetization state is determined, and potential scaling and supersampling is performed. At the end, all variables are passed to the preparation section. For a more detailed description including the definition of variables is given in the text.

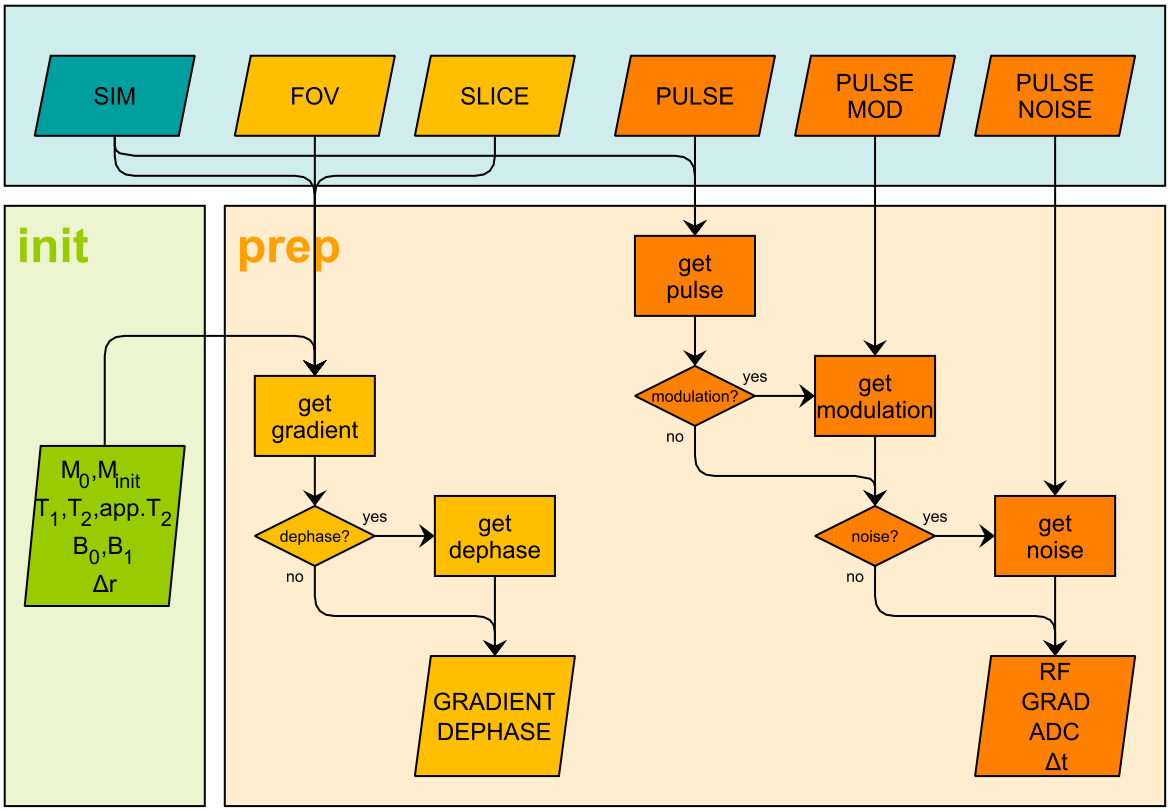

Figure 8.2: Illustration of the simulation tool: preparation. Marked by the orange boxes is the computation of the RF pulse object: initialized at first, potentially modulated, and altered by noise contributions. The yellow boxes mark the evolution of the gradient fields. A simplification of the computational burden is not illustrated within this figure but explained in the text. The main gradient field is defined at first. If specified, a supersampling field is calculated afterward. All variables are passed to the run section. For a more detailed description including the definition of variables is given in the text.

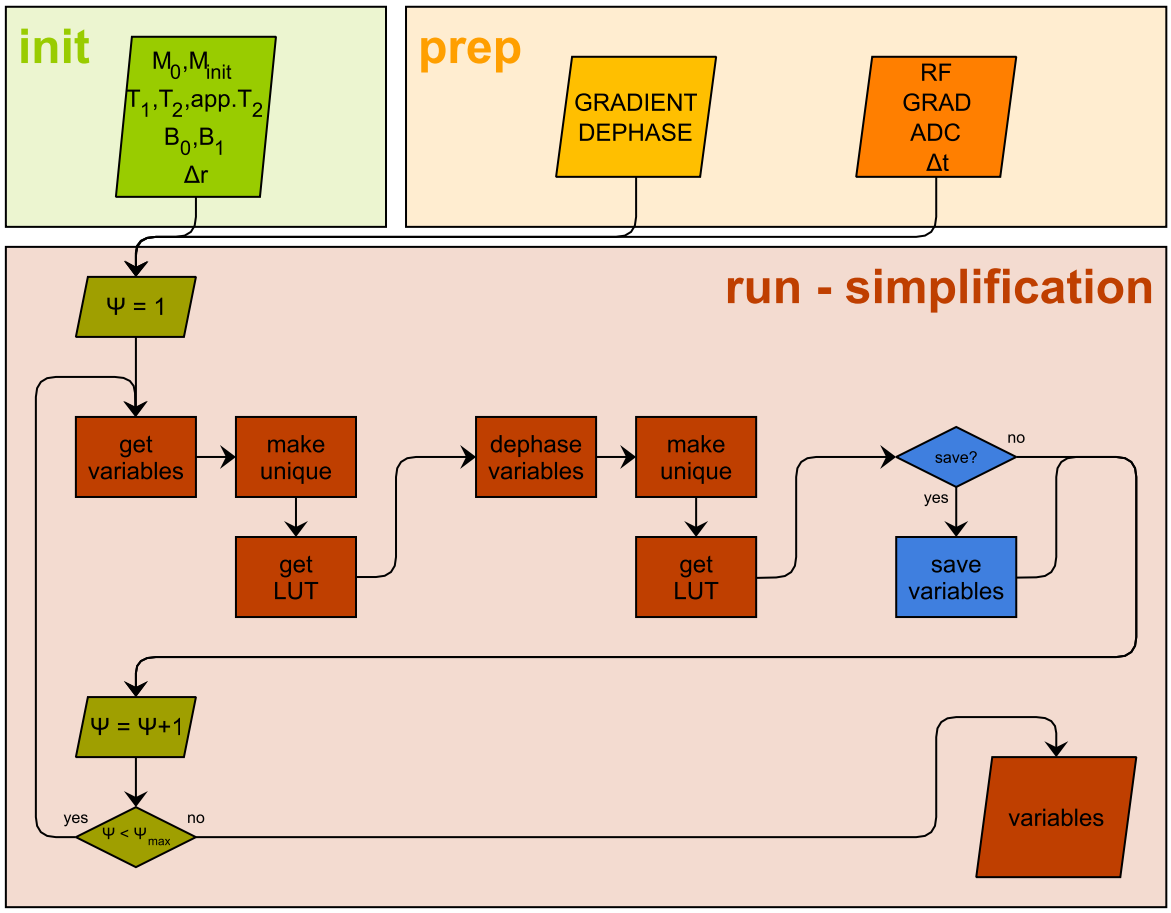

Figure 8.3: Illustration of the simulation tool: run simplification. All variables from the initialization and preparation section are stored in a single matrix as a unique set; this is done to minimize the computational burden of the simulation. A loop iterates over all gradient orientations Ψ. In a two-step process, the set of magnetization and physical parameters is made unique at first. This is followed by regarding the supersampling, expanding the matrix and then making it unique again. Each set can be stored to the hard drive if desired. For a more detailed description including the definition of variables is given in the text.

The run section is the central part of the code. At first, it takes the information about the magnetization space from the initialization section and the information about the pulse object from the preparation section and stores it in a single matrix as a unique set as illustrated in figure 8.3. The magnetization vectors are normalized first. This is possible because the magnitude of the vector only acts as a scaling parameter. Next, a loop over all orientations Ψ of the gradient from the preparation section is executed. Within this loop, the three entries of the normalized magnetization are concatenated with the longitudinal and transverse relaxation time, with the static magnetic and all RF field maps (in case of multi-channel transmission), and with the gradient distance map. A unique set of entries with the corresponding lookup table is determined on a pixel by pixel basis. This unique set is then again concatenated with the supersampling gradient field. By doing this in consecutive steps, the computational burden is reduced. At the end of a loop iteration, the resulting matrix can either be stored on the hard drive or kept within the main memory.

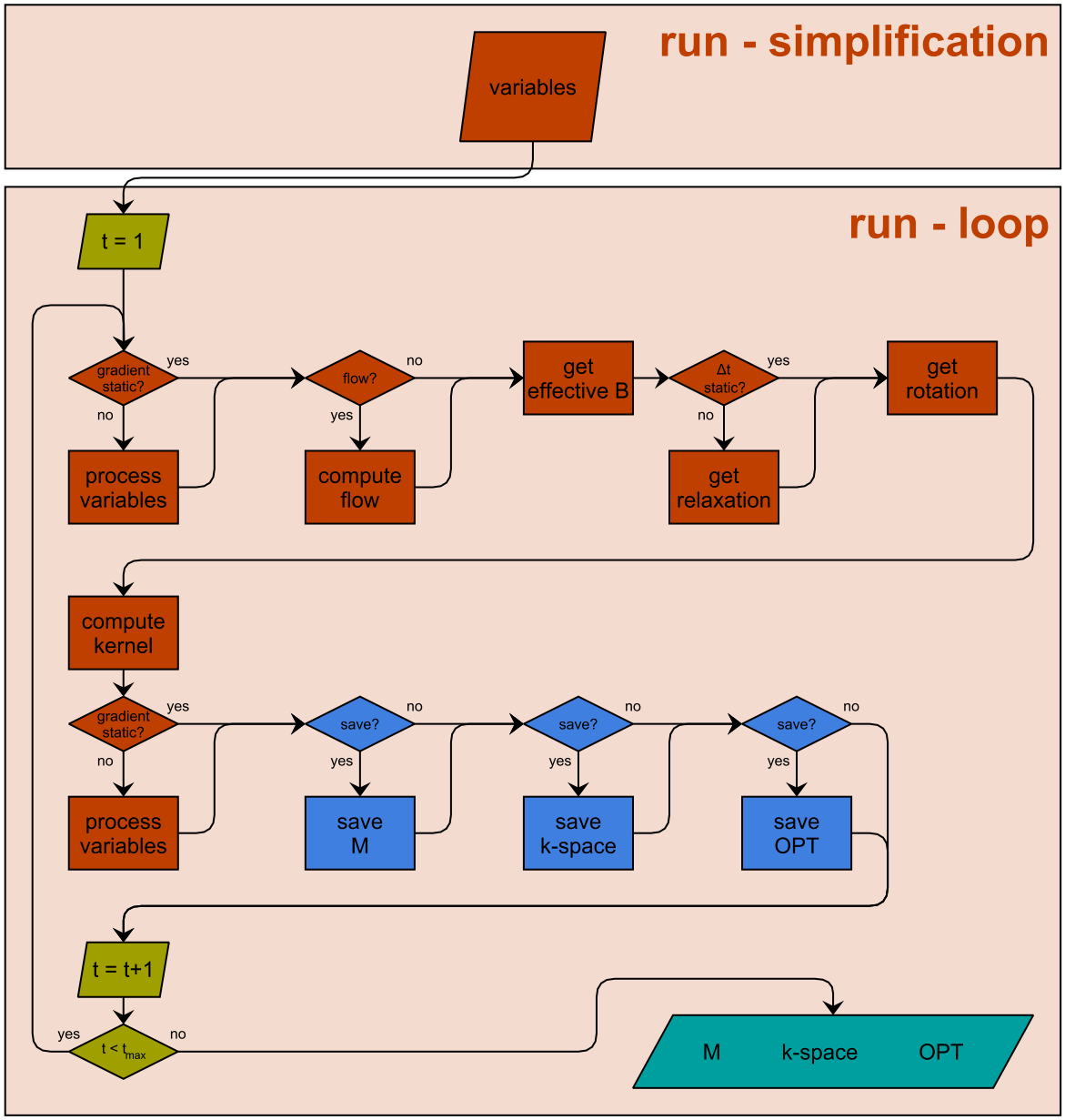

Figure 8.4: Illustration of the simulation tool: run loop. The run loop executes the mathematical kernel for all time steps. At first the variables from the run simplification section need to be preprocessed (loaded from hard drive if specified). Next, the flow transition is performed. The effective magnetic field, the relaxation matrices, and the rotation matrix are defined sequentially. Finally, the mathematical kernel is called. Before the loop iteration ends, different variables can be saved to the hard drive. Once the loop is finished, the resulting variables are passed back. For a more detailed description including the definition of variables is given in the text.

Once all orientations are computed, a second matrix is created holding the information about the pulse amplitude, frequency, and phase as well as the gradient amplitude.

Once all variables have been initialized in the run section, the actual time loop, outlined in figure 8.4, is computed. At first, the unique set of variables is loaded either from hard drive or extracted from the main memory. Before the rotation matrices and their basic contributions are calculated, motion must be regarded. For this reason, the parameter space is shifted by the transition vector of the flow. New linearly interpolated $\mathtt{B_0}$ and $\mathtt{B_1}$ field grids are the result.

Next, the effective magnetic field is determined as described in section 4.1.1. It consists of three dimensions (logical notation: read, phase, and slice), despite the fact of multi-channel transmission. In the latter case, the vector sum of all channel contributions is taken. With this basic information, the 3×3 rotation matrix can be calculated. The relaxation processes are regarded as outlined in chapter 4.1.2. Finally, the mathematical kernel can be called for one time step.

The unique matrix is decomposed into its original state revealing the scaled magnetization space. The result of a time step can be evaluated and saved depending on the simulation mode. On one hand, the complete magnetization with the scaling but without the dephasing can be written to the hard drive as an indexed file. This can have a huge data load as a result. As an alternative, a k-space from virtual ADCs can be produced and saved. It can be in the case of spatially resolved simulations, where the complex sum of all magnetization vectors is stored in a matrix position corresponding to the ADC entries. Alternatively, it could be in the case of time resolved imaging, e. g. magnetic resonance fingerprinting, with a spatial and temporal assignment. The last possible option is the evaluation regarding efficiency and/or safety issues of each time step of a pulse object.

After all information has been stored, the unique set of variables is conditioned to fit as a basis of the following loop iteration. Once the loop iteration index meets the abortion criterion, once the final time step is processed, the magnetization space and the k-space and the pulse evaluation are passed back to the preparation and to the initialization section and the program quits.

The result is given by three variables: `M` for the magnetization, `k-space` for the k-space, and `OPT` for the evaluation of the pulse object.

Bibliography

Abragam, A. (1983). *Principles of Nuclear Magnetism*. Oxford University Press. ISBN: 9780198520146. 5

Benoit-Cattin, H., Collewet, G., Belaroussi, B., Saint-Jalmes, H., & Odet, C. (2005). The simri project: a versatile and interactive mri simulator. *Journal of Magnetic Resonance*, 173(1):97–115. 117, 118, 119, 120

Berger, M., Semmler, W., & Bock, M. (2011). Simulation of the filtering effect of the flash readout on saturation recovery t1 evaluation. In: *Proceedings of the International Society for Magnetic Resonance in Medicine (19)*. 121

Beringer, J. e. a. (2012). Review of particle physics. *Physical Review D*, 86(1):1–1526. 7

Bernstein, M., King, K., & Zhou, X. (2004). *Handbook of MRI Pulse Sequences*. Elsevier Academic Press. ISBN: 9780120928613. 5, 116

Bloch, F. (1946). Nuclear induction. *Physical Review*, 70(7-8):460–474. 11

Boada, F., Gillen, J., Shen, G., Chang, S., & Thulborn, K. (1997). Fast three dimensional sodium imaging. *Magnetic Resonance in Medicine*, 37(5):706–715. 22

Bottomley, P. & Andrew, E. (1978). Rf magnetic field penetration, phase shift and power dissipation in biological tissue: Implications for nmr imaging. *Physics in Medicine and Biology*, 23(4):630–643. 26, 27, 116

Breithaupt, M., Berger, M., Homagk, A.-K., Semmler, W., & Bock, M. (2012). Let's do the time warp again - slice profile evolution of adiabatic pulses at 7 tesla. In: *Proceedings of the International Society for Magnetic Resonance in Medicine (20)*. 118, 121

Breithaupt, M., Flassbeck, S., Berger, M., & Nagel, A. (2014). High resolution t1 mapping of the full brain with a modified despot1-hifi approach at 7 t. In: *Proceedings of the International Society for Magnetic Resonance in Medicine (22)*. 113, 120, 123

Brenner, A., Kursch, J., & Noll, T. (1997). Distributed large-scale simulation of magnetic resonance imaging. *Magnetic Resonance Materials in Physics, Biology and Medicine*, 5(2):129–138. 117

Christensen, K., Grant, D., Schulman, E., & Walling, C. (1974). Optimal determination of relaxation times of fourier transform nuclear magnetic resonance. determination of spin-lattice relaxation times in chemically polarized species. *Journal of Physical Chemistry*, 78(19):1971–1977. 45, 120

Conolly, S., Nishimura, D., Macovski, A., & Glover, G. (1988). Variable-rate selective excitation. *Journal of Magnetic Resonance (1969)*, 78(3):440–458. 19, 54, 115

Deichmann, R., Good, C., Josephs, O., Ashburner, J., & Turner, R. (2000). Optimization of 3-d mp-rage sequences for structural brain imaging. *NeuroImage*, 12(1):112–127. 121

Deichmann, R. & Haase, A. (1992). Quantification of t1 values by snapshot-flash nmr imaging. *Journal of Magnetic Resonance (1969)*, 96(3):608–612. 121

Deichmann, R., Hahn, D., & Haase, A. (1999). Fast t1 mapping on a whole-body scanner. *Magnetic Resonance in Medicine*, 42(1):206–209. 120

Deoni, S. (2007). High-resolution t1 mapping of the brain at 3t with driven equilibrium single pulse observation of t1 with high-speed incorporation of rf field inhomogeneities (despot1-hifi). *Journal of Magnetic Resonance Imaging*, 26(4):1106–1111. 47, 59, 120, 124

Deoni, S., Peters, T., & Rutt, B. (2005). High-resolution t1 and t2 mapping of the brain in a clinically acceptable time with despot1 and despot2. *Magnetic Resonance in Medicine*, 53(1):237–241. 45

Deoni, S., Rutt, B., & Peters, T. (2003). Rapid combined t1 and t2 mapping using gradient recalled acquisition in the steady state. *Magnetic Resonance in Medicine*, 49(3):515–526. 45, 120

Detre, J., Leigh, J., Williams, D., & Koretsky, A. (1992). Perfusion imaging. *Magnetic Resonance in Medicine*, 23(1):37–45. 25, 44

Gabriel, C., Gabriel, S., & Corthout, E. (1996a). The dielectric properties of biological tissues: I. literature survey. *Physics in Medicine and Biology*, 41(11):2231–2249. 26

Gabriel, S., Lau, R., & Gabriel, C. (1996b). The dielectric properties of biological tissues: Ii. measurements in the frequency range 10 hz to 20 ghz. *Physics in Medicine and Biology*, 41(11):2251–2269. 26

Gabriel, S., Lau, R., & Gabriel, C. (1996c). The dielectric properties of biological tissues: Iii. parametric models for the dielectric spectrum of tissues. *Physics in Medicine and Biology*, 41(11):2271–2293. 26

Gatehouse, P., Firmin, D., Collins, S., & Longmore, D. (1994). Real time blood flow imaging by spiral scan phase velocity mapping. *Magnetic Resonance in Medicine*, 31(5):504–512. 22

Glover, G. & Lee, A. (1995). Motion artifacts in fmri: Comparison of 2dft with pr and spiral scan methods. *Magnetic Resonance in Medicine*, 33(5):624–635. 22

Goldberg, D. & Holland, J. (1988). Genetic algorithms and machine learning. *Machine Learning*, 3(2-3):95–99. 19, 117

Gowland, P. & Mansfield, P. (1993). Accurate measurement of t1 in vivo in less than 3 seconds using echo-planar imaging. *Magnetic Resonance in Medicine*, 30(3):351–354. 120

Gowland, P., Mansfield, P., Bullock, P., Stehling, M., Worthington, B., & Firth, J. (1992). Dynamic studies of gadolinium uptake in brain tumors using inversion-recovery echo-planar imaging. *Magnetic Resonance in Medicine*, 26(2):241–258. 44

Griswold, M., Jakob, P., Heidemann, R., Nittka, M., Jellus, V., Wang, J., Kiefer, B., & Haase, A. (2002). Generalized autocalibrating partially parallel acquisitions (grappa). *Magnetic Resonance in Medicine*, 47(6):1202–1210. 22

Gruetter, R. (1993). Automatic, localized in vivo adjustment of all first- and second-order shim coils. *Magnetic Resonance in Medicine*, 29(6):804–811. 114

Haacke, E., Brown, R., Thompson, M., & Venkatesan, R. (1999). *Magnetic Resonance Imaging: Physical Principles and Sequence Design*. Wiley-Liss. ISBN: 9780471351283. 5, 7

Haacke, E. & Lenz, G. (1987). Improving mr image quality in the presence of motion by using rephasing gradients. *American Journal of Roentgenology*, 148(6):1251–1258. 39

Haase, A., Frahm, J., Matthaei, D., Hanicke, W., & Merboldt, K.-D. (1986). Flash imaging. rapid nmr imaging using low flip-angle pulses. *Journal of Magnetic Resonance (1969)*, 67(2):258–266. 23, 36

Homer, J. & Beevers, M. (1985). Driven-equilibrium single-pulse observation of t1 relaxation. a reevaluation of a rapid "new" method for determining nmr spin-lattice relaxation times. *Journal of Magnetic Resonance (1969)*, 63(2):287–297. 45

Homer, J. & Roberts, J. (1987). Conditions for the driven equilibrium single pulse observation of spin-lattice relaxation times. *Journal of Magnetic Resonance (1969)*, 74(3):424–432. 45

Homer, J. & Roberts, J. (1990). Routine evaluation of m0 ratios and t1 values from driven-equilibrium nmr spectra. *Journal of Magnetic Resonance (1969)*, 89(2):265–272. 45

Hoult, D. & Lauterbur, P. (1979). The sensitivity of the zeugmatographic experiment involving human samples. *Journal of Magnetic Resonance (1969)*, 34(2):425–433. 25

Hurley, A., Al-Radaideh, A., Bai, L., Aickelin, U., Coxon, R., Glover, P., & Gowland, P. (2010). Tailored rf pulse for magnetization inversion at ultrahigh field. *Magnetic Resonance in Medicine*, 63(1):51–58. 117

IEC (2010). 60601, 2 33: Medical electrical equipment, part 2 33: Particular requirements for the basic safety and essential performance of magnetic resonance equipment for medical diagnosis. Technical report, International Electrotechnical Commission. 27

Ikonomidou, V., van Gelderen, P., de Zwart, J., & Duyn, J. (2006). T1 measurements at 7 t with application to tissue specific imaging. In: *Proceedings of the International Society for Magnetic Resonance in Medicine (14)*. 126

Keller, P., Drayer, B., Fram, E., Williams, K., Dumoulin, C., & Souza, S. (1989). Mr angiography with two-dimensional acquisition and three-dimensional display. *Radiology*, 173(2):527–532. 25

King, K., Foo, T., & Crawford, C. (1995). Optimized gradient waveforms for spiral scanning. *Magnetic Resonance in Medicine*, 34(2):156–160. 22

Konstandin, S. & Nagel, A. (2014). Measurement techniques for magnetic resonance imaging of fast relaxing nuclei. *Magnetic Resonance Materials in Physics, Biology and Medicine*, 27(1):5–19. 26

Konstandin, S., Nagel, A., Heiler, P., & Schad, L. (2011). Two-dimensional radial acquisition technique with density adaption in sodium mri. *Magnetic Resonance in Medicine*, 65(4):1090–1096. 22

Kraff, O., Fischer, A., Nagel, A., Monninghoff, C., & Ladd, M. (2015). Mri at 7 tesla and above: Demonstrated and potential capabilities. *Journal of Magnetic Resonance Imaging*, 41(1):13–33. 25, 26, 114, 116

Lauterbur, P. (1973). Image formation by induced local interactions: Examples employing nuclear magnetic resonance. *Nature*, 242(3):190–191. 22

Le Roux, P. (1986). 8610179. Technical report, French Patent. 19, 54, 115

Levitt, M. (2008). *Spin Dynamics: Basics of Nuclear Magnetic Resonance*. Wiley-Liss. ISBN: 9780470511176. 6

Li, T.-Q. & Deoni, S. (2006). Fast t1 mapping of the brain at 7 t with rf calibration using three point despot1 method. In: *Proceedings of the International Society for Magnetic Resonance in Medicine (14)*. 46, 56, 57, 124, 125, 126

Lin, C. & Bernstein, M. (2008). 3d magnetization prepared elliptical centric fast gradient echo imaging. *Magnetic Resonance in Medicine*, 59(2):434–439. 121

Look, D. & Locker, D. (1970). Time saving in measurement of nmr and epr relaxation times. *Review of Scientific Instruments*, 41(2):250–251. 120

Ma, D., Gulani, V., Seiberlich, N., Liu, K., Sunshine, J., Duerk, J., & Griswold, M. (2013). Magnetic resonance fingerprinting. *Nature*, 495(7440):187–192. 120, 122, 123, 124, 125

MacFall, J., Charles, H., & Prost, R. (1990). Truncated since slice excitation for 31p spectroscopic imaging. *Magnetic Resonance Imaging*, 8(5):619–624. 22

Madelin, G. & Regatte, R. (2013). Biomedical applications of sodium mri in vivo. *Journal of Magnetic Resonance Imaging*, 38(3):511–529. 26

Mansfield, P. (1977). Multi-planar image formation using nmr spin echoes. *Journal of Physics C - Solid State Physics*, 10(3):L55–L58. 22

Mansfield, P., Harvey, P., & Stehling, M. (1994). Echo-volumar imaging. *Magnetic Resonance Materials in Physics, Biology and Medicine*, 2(3):291–294. 22

Marques, J., Kober, T., Krueger, G., van der Zwaag, W., Van de Moortele, P.-F., & Gruetter, R. (2010). Mp2rage, a self bias-field corrected sequence for improved segmentation and t1-mapping at high field. *NeuroImage*, 49(2):1271–1281. 123, 124, 125, 126

Marques, J., Kober, T., van der Zwaag, W., Kruegger, G., & Gruetter, R. (2008). Mp2rage, a self-bias field corrected sequence for improved segmentation at high field. In: *Proceedings of the International Society for Magnetic Resonance in Medicine (16)*. 123

Marschar, A., Breithaupt, M., Berger, M., & Nagel, A. (2014). T1 and t2 relaxation times of the human calf at 7 tesla. In: *Proceedings of the International Society for Magnetic Resonance in Medicine (22)*. 126

The MathWorks MATLAB Products and Services. MathWorks.com. The MathWorks Inc. Accessed: 2015.2.2. URL `http://www.mathworks.com/products/`. 35

Medical Imaging Interaction Toolkit. MITK.org. German Cancer Research Center, Division of Medical and Biological Informatics. Accessed: 2015.2.2. URL `http://www.mitk.org`. 35

Mugler, J. & Brookeman, J. (1990). Three-dimensional magnetization-prepared rapid gradient-echo imaging (3d mp rage). *Magnetic Resonance in Medicine*, 15(1):152–157. 39

Nagel, A., Laun, F., Weber, M.-A., Matthies, C., Semmler, W., & Schad, L. (2009). Sodium mri using a density-adapted 3d radial acquisition technique. *Magnetic Resonance in Medicine*, 62(6):1565–1573. 22

The Nobel Prize in Physics 1902. Nobelprize.org. Nobel Media AB (2013). Accessed: 2014.1.13. URL `http://www.nobelprize.org/nobel_prizes/physics/laureates/1902`. 6

The Nobel Prize in Physics 1943. Nobelprize.org. Nobel Media AB (2013). Accessed: 2014.1.13. URL `http://www.nobelprize.org/nobel_prizes/physics/laureates/1943`. 6

The Nobel Prize in Physics 1944. Nobelprize.org. Nobel Media AB (2013). Accessed: 2014.1.13. URL `http://www.nobelprize.org/nobel_prizes/physics/laureates/1944`. 6

The Nobel Prize in Physics 1952. Nobelprize.org. Nobel Media AB (2013). Accessed: 2014.1.13. URL `http://www.nobelprize.org/nobel_prizes/physics/laureates/1952`. 6

The Nobel Prize in Chemistry 1991. Nobelprize.org. Nobel Media AB (2013). Accessed: 2014.1.13. URL `http://www.nobelprize.org/nobel_prizes/chemistry/laureates/1991`. 6

The Nobel Prize in Chemistry 2002. Nobelprize.org. Nobel Media AB (2013). Accessed: 2014.1.13. URL `http://www.nobelprize.org/nobel_prizes/chemistry/laureates/2002`. 6

The Nobel Prize in Physiology or Medicine 2003. Nobelprize.org. Nobel Media AB (2013). Accessed: 2014.1.13. URL `http://www.nobelprize.org/nobel_prizes/medicine/laureates/2003`. 14

Noebauer-Huhmann, I., Szomolanyi, P., Juras, V., Kraff, O., Ladd, M., & Trattnig, S. (2010). Gadolinium-based magnetic resonance contrast agents at 7 tesla: In vitro t1 relaxivities in human blood plasma. *Investigative Radiology*, 45(9):554–558. 33

Ogawa, S., Tank, D., Menon, R., Ellermann, J., Kim, S.-G., Merkle, H., & Ugurbil, K. (1992). Intrinsic signal changes accompanying sensory stimulation: Functional brain mapping with magnetic resonance imaging. *Proceedings of the National Academy of Sciences of the United States of America*, 89(13):5951–5955. 25

Oppelt, A., Graumann, R., Barfuss, H., Fischer, H., Hartl, W., & Shajor, W. (1986). Fisp - a new fast mri sequence. *Electromedica*, 54(1):15–18. 121

Pattany, P., Phillips, J., Chiu, L., Lipcamon, J., Duerk, J., McNally, J., & Mohapatra, S. (1987). Motion artifact suppression technique (mast) for mr imaging. *Journal of Computer Assisted Tomography*, 11(3):369–377. 39

Pauly, J., Le Roux, P., Nishimura, D., & Macovski, A. (1991). Parameter relations for the shinnar-le roux selective excitation pulse design algorithm. *IEEE Transactions on Medical Imaging*, 10(1):53–65. 19

Pauly, J., Nishimura, D., & Macovski, A. (1989). A k-space analysis of small-tip-angle excitation. *Journal of Magnetic Resonance (1969)*, 81(1):43–56. 18

Pitkanen, A., Laakso, M., Kalviainen, R., Partanen, K., Vainio, P., Lehtovirta, M., Riekkinen, P., & Soininen, H. (1996). Severity of hippocampal atrophy correlates with the prolongation of mri t2 relaxation time in temporal lobe epilepsy but not in alzheimer's disease. *Neurology*, 46(6):1724–1730. 44

Pohmann, R., Speck, O., & Scheffler, K. (2015). Signal-to-noise ratio and mr tissue parameters in human brain imaging at 3, 7, and 9.4 tesla using current receive coil arrays. *Magnetic Resonance in Medicine*, Early View(Early View):1–9. 26

Pruessmann, K., Weiger, M., Scheidegger, M., & Boesiger, P. (1999). Sense: Sensitivity encoding for fast mri. *Magnetic Resonance in Medicine*, 42(5):952–962. 22

P. Reimer, P. Parizel, & F.-A. Stichnoth, ed. (2010). *Clinical MR Imaging: A Practical Approach*. Springer-Verlag. ISBN: 9783540745013. 5

M. Reiser, W. Semmler, & H. Hricak, ed. (2007). *Magnetic Resonance Tomography*. Springer-Verlag. ISBN: 9783540293545. 5

Ren, J., Dimitrov, I., Sherry, A., & Malloy, C. (2008). Composition of adipose tissue and marrow fat in humans by 1h nmr at 7 tesla. *Journal of Lipid Research*, 49(9):2055–2062. 126

Robitaille, P.-M. & Berliner, L. (2006). *Ultra High Field Magnetic Resonance Imaging*. Springer-Verlag. ISBN: 9780387342313. 5, 25, 114

Rooney, W., Johnson, G., Li, X., Cohen, E., Kim, S.-G., Ugurbil, K., & Springer, C. (2007). Magnetic field and tissue dependencies of human brain longitudinal 1h2o relaxation in vivo. *Magnetic Resonance in Medicine*, 57(2):308–318. 126

Ruggieri, P., Laub, G., Masaryk, T., & Modic, M. (1989). Intracranial circulation: Pulse-sequence considerations in three-dimensional (volume) mr angiography. *Radiology*, 171(3):793–799. 25

Rundle, D., Kishore, S., Seshadri, S., & Wehrli, F. (1990). Magnetic resonance imaging simulator: A teaching tool for radiology. *Journal of Digital Imaging*, 3(4):226–229. 117

Shen, J., Rycyna, R., & Rothman, D. (1997). Improvements on an in vivo automatic shimming method (fastermap). *Magnetic Resonance in Medicine*, 38(5):834–839. 114

Shinnar, M., Eleff, S., Subramanian, H., & Leigh, J. (1989). The synthesis of pulse sequences yielding arbitrary magnetization vectors. *Magnetic Resonance in Medicine*, 12(1):74–80. 19, 54, 115

Shinnar, M. & Leigh, J. (1989). The application of spinors to pulse synthesis and analysis. *Magnetic Resonance in Medicine*, 12(1):93–98. 19

Shkarin, P. & Spencer, R. (1996). Direct simulation of spin echoes by summation of isochromats. *Concepts in Magnetic Resonance*, 8(4):253–268. 117

Silver, M., Joseph, R., & Hoult, D. (1984). Highly selective $\pi/2$ and π pulse generation. *Journal of Magnetic Resonance (1969)*, 59(2):347–351. 17

Slichter, C. (1978). *Principles of Magnetic Resonance*. Springer-Verlag. ISBN: 9780387084763. 5

Steen, R., Gronemeyer, S., Kingsley, P., Reddick, W., Langston, J., & Taylor, J. (1994). Precise and accurate measurement of proton t1 in human brain in vivo: Validation and preliminary clinical application. *Journal of Magnetic Resonance Imaging*, 4(5):681–691. 120

Stocker, T., Vahedipour, K., Pflugfelder, D., & Shah, N. (2010). High-performance computing mri simulations. *Magnetic Resonance in Medicine*, 64(1):186–193. 117, 118, 119, 120

Summers, R., Axel, L., & Israel, S. (1986). A computer simulation of nuclear magnetic resonance imaging. *Magnetic Resonance in Medicine*, 3(3):363–376. 117

Torheim, G., Rinck, P., Jones, R., & Kvaerness, J. (1994). A simulator for teaching mr image contrast behavior. *Magnetic Resonance Materials in Physics, Biology and Medicine*, 2(4):515–522. 117

Truong, T.-K., Chakeres, D., Beversdorf, D., Scharre, D., & Schmalbrock, P. (2006). Effects of static and radiofrequency magnetic field inhomogeneity in ultra-high field magnetic resonance imaging. *Magnetic Resonance Imaging*, 24(2):103–112. 26, 114, 116

Ugurbil, K., Garwood, M., & Bendall, M. (1987). Amplitude- and frequency-modulated pulses to achieve 90° plane rotations with inhomogeneous b1 fields. *Journal of Magnetic Resonance (1969)*, 72(1):177–185. 19

Ugurbil, K., Garwood, M., & Rath, A. (1988). Optimization of modulation functions to improve insensitivity of adiabatic pulses to variations in b1 magnitude. *Journal of Magnetic Resonance (1969)*, 80(3):448–469. 19

Van de Moortele, P.-F., Akgun, C., Adriany, G., Moeller, S., Ritter, J., Collins, C., Smith, M., Vaughan, J., & Ugurbil, K. (2005). B1 destructive interferences and spatial phase patterns at 7 t with a head transceiver array coil. *Magnetic Resonance in Medicine*, 54(6):1503–1518. 116

Van de Moortele, P.-F., Auerbach, E., Olman, C., Yacoub, E., Ugurbil, K., & Moeller, S. (2009). T1 weighted brain images at 7 tesla unbiased for proton density, t2* contrast and rf coil receive b1 sensitivity with simultaneous vessel visualization. *NeuroImage*, 46(2):432–446. 120, 123, 125

Vymazal, J., Righini, A., Brooks, R., Canesi, M., Mariani, C., Leonardi, M., & Pezzoli, G. (1999). T1 and t2 in the brain of healthy subjects, patients with parkinson disease, and patients with multiple system atrophy: Relation to iron content. *Radiology*, 211(2):489–495. 44

Wang, H., Riederer, S., & Lee, J. (1987). Optimizing the precision in t1 relaxation estimation using limited flip angles. *Magnetic Resonance in Medicine*, 5(5):399–416. 45

Wendt, R. (1991). Interactive design of motion-compensated gradient waveforms with a personal computer spreadsheet program. *Journal of Magnetic Resonance Imaging*, 1(1):87–92. 39

Wilson, J., Jenkinson, M., de Araujo, I., Kringelbach, M., Rolls, E., & Jezzard, P. (2002). Fast, fully automated global and local magnetic field optimization for fmri of the human brain. *NeuroImage*, 17(2):967–976. 114

Wright, P., Mougin, O., Totman, J., Peters, A., Brookes, M., Coxon, R., Morris, P., Clemence, M., Francis, S., Bowtell, R., & Gowland, P. (2008). Water proton t1 measurements in brain tissue at 7, 3, and 1.5 t using ir-epi, ir-tse, and mprage: results and optimization. *Magnetic Resonance Materials in Physics, Biology and Medicine*, 21(1-2):121–130. 126

Zur, Y., Wood, M., & Neuringer, L. (1991). Spoiling of transverse magnetization in steady-state sequences. *Magnetic Resonance in Medicine*, 21(2):251–263. 38, 121